National Library
of Canada

Acquisitions and
Bibliographic Services Branch

395 Wellington Street
Ottawa, Ontario
K1A 0N4

Bibliothèque nationale
du Canada

Direction des acquisitions et
des services bibliographiques

395, rue Wellington
Ottawa (Ontario)
K1A 0N4

Your file Votre référence

Our file Notre référence

NOTICE

The quality of this microform is heavily dependent upon the quality of the original thesis submitted for microfilming. Every effort has been made to ensure the highest quality of reproduction possible.

If pages are missing, contact the university which granted the degree.

Some pages may have indistinct print especially if the original pages were typed with a poor typewriter ribbon or if the university sent us an inferior photocopy.

Reproduction in full or in part of this microform is governed by the Canadian Copyright Act, R.S.C. 1970, c. C-30, and subsequent amendments.

AVIS

La qualité de cette microforme dépend grandement de la qualité de la thèse soumise au microfilmage. Nous avons tout fait pour assurer une qualité supérieure de reproduction.

S'il manque des pages, veuillez communiquer avec l'université qui a conféré le grade.

La qualité d'impression de certaines pages peut laisser à désirer, surtout si les pages originales ont été dactylographiées à l'aide d'un ruban usé ou si l'université nous a fait parvenir une photocopie de qualité inférieure.

La reproduction, même partielle, de cette microforme est soumise à la Loi canadienne sur le droit d'auteur, SRC 1970, c. C-30, et ses amendements subséquents.

Canada

University of Alberta

Enhancements to Millimetre- and Submillimetre-Wave Integrated Circuit Receivers

by

Bruce George Veidt ©

A thesis submitted to the Faculty of Graduate Studies and Research in partial fulfillment of the requirements for the degree of Doctor of Philosophy.

Department of Electrical Engineering

Edmonton, Alberta

Fall, 1995

National Library of Canada
Acquisitions and Bibliographic Services Branch
395 Wellington Street
Ottawa, Ontario
K1A 0N4

Bibliothèque nationale du Canada
Direction des acquisitions et des services bibliographiques
395, rue Wellington
Ottawa (Ontario)
K1A 0N4

Your file Votre référence

Our file Notre référence

THE AUTHOR HAS GRANTED AN IRREVOCABLE NON-EXCLUSIVE LICENCE ALLOWING THE NATIONAL LIBRARY OF CANADA TO REPRODUCE, LOAN, DISTRIBUTE OR SELL COPIES OF HIS/HER THESIS BY ANY MEANS AND IN ANY FORM OR FORMAT, MAKING THIS THESIS AVAILABLE TO INTERESTED PERSONS.

L'AUTEUR A ACCORDE UNE LICENCE IRREVOCABLE ET NON EXCLUSIVE PERMETTANT A LA BIBLIOTHEQUE NATIONALE DU CANADA DE REPRODUIRE, PRETER, DISTRIBUER OU VENDRE DES COPIES DE SA THESE DE QUELQUE MANIERE ET SOUS QUELQUE FORME QUE CE SOIT POUR METTRE DES EXEMPLAIRES DE CETTE THESE A LA DISPOSITION DES PERSONNE INTERESSEES.

THE AUTHOR RETAINS OWNERSHIP OF THE COPYRIGHT IN HIS/HER THESIS. NEITHER THE THESIS NOR SUBSTANTIAL EXTRACTS FROM IT MAY BE PRINTED OR OTHERWISE REPRODUCED WITHOUT HIS/HER PERMISSION.

L'AUTEUR CONSERVE LA PROPRIETE DU DROIT D'AUTEUR QUI PROTEGE SA THESE. NI LA THESE NI DES EXTRAITS SUBSTANTIELS DE CELLE-CI NE DOIVENT ETRE IMPRIMES OU AUTREMENT REPRODUITS SANS SON AUTORISATION.

ISBN 0-612-06304-6

Canada

University of Alberta

Library Release Form

Name of Author: Bruce George Veidt

Title of Thesis: Enhancements to Millimetre- and Submillimetre-Wave Integrated Circuit Receivers

Degree: Doctor of Philosophy

Year this Degree Granted: 1995

Permission is hereby granted to the University of Alberta Library to reproduce single copies of this thesis and to lend copies for private, scholarly, or scientific research purposes only.

The author reserves all other publication and other rights in association with the copyright in the thesis, except as hereinbefore provided, neither the thesis nor any substantial portion thereof may be printed or otherwise reproduced in any material form whatever without the author's prior written permission.

10993-74 Avenue
Edmonton, AB
T6G 0E5

Dated: October 6, 1995

“Everyone should take two trips into the wilderness each year, each of six months duration.”

Ernest Thompson Seton

University of Alberta

Faculty of Graduate Studies and Research

The undersigned certify that they have read, and recommend to the Faculty of Graduate Studies and Research for acceptance, a thesis entitled *Enhancements to Millimetre- and Submillimetre-Wave Integrated Circuit Receivers* submitted by *Bruce George Veidt* in partial fulfillment of the requirements for the degree of *Doctor of Philosophy.*

D. Routledge

D. Routledge, Supervisor

J F Vaneldik

J. F. Vaneldik, Supervisor

M Brett

M. J. Brett

J McMullin

J. McMullin

D. P. Hube

C.T. Cunningham

C. T. Cunningham

Herzberg Institute of Astrophysics

Dated: Oct. 5, 1995

Abstract

An important area of radio astronomy instrumentation is the development of sensitive receivers at millimetre- and submillimetre-wavelengths. Over the last decade, there has been steady progress in advancing the technology from using receivers based on mechanically machined waveguides and horn antennas to transmission lines and antennas fabricated using integrated circuit techniques. The motivation has been to simplify the fabrication of the receivers through the use of photolithography and etching. It is hoped that this will eventually lead to the development of focal plane arrays, which have many elements placed side-by-side forming a radio camera.

The first part of this thesis addresses one of the problems with the integrated circuit technology, namely the fixed nature of the circuits, by examining one type of electrically-adjustable tuning. In those experiments, the bias voltage was modulated across the active device so as to change its tuning. Unfortunately the tuning effect was severely limited by the electrical nonlinearity of the device. Another part of this thesis builds upon the integrated nature of modern receivers by adding what, up until now, has been an external component: the Josephson effect suppression electromagnet. This technique will allow the receiving elements to be much simpler and smaller than would otherwise be the case. Finally, the last part of this thesis examines another method of constructing antennas and transmission lines using integrated circuit techniques. This work shows the feasibility of integrating a waveguide fabricated with integrated circuit technology with a diagonal horn antenna. This technique will provide another option for receiver designers.

Acknowledgments

First, I must thank my wife Nancy for her constant support and for enduring the long winters on the steppe.

This thesis would not have been possible without SIS junctions made by Kevin Kornelsen. I thank him for his tireless effort. Roy Schmaus also played an important part by building and maintaining the vacuum, cryogenic, and electronic systems used in the receiver laboratory.

Equipment crucial for this work was obtained from several sources. Graham McKinnon made available the device fabrication facilities at the Alberta Microelectronic Centre, John MacLeod of the JCMT Group of the National Research Council provided a receiver cryostat and a mixer block, and Dave Clegg at TRLabs provided access to an HP-8510 network analyzer. The generosity of these people and their organizations is acknowledged.

My supervisors, Dave Routledge and Fred Vaneldik, are thanked for their encouragement, financial support, and for giving me the freedom to pursue any topic that interested me. They also provided critical and helpful reviews of my writing. Mike Brett also provided moral support and important technical advice. Tom Landecker's advise was important to both help me decide to do further graduate work and to continue when the problems seemed insurmountable.

A number of people at other institutes helped me understand SIS devices and receivers. They include Brian Ellison, Mike Wengler, Thomas Büttgenbach, and Jacob Kooi. Their expert advice is gratefully acknowledged.

A number of financial sources must be acknowledged. The National Sciences and Engineering Research Council (NSERC), and the Alberta Microelectronic Centre provided major scholarships. Additional funds were received from the Eva Segall Scholarship, the R. M. Hardy Graduate Scholarship, and the Walter H. Johns Graduate Fellowship. Funding to our research group was provided by NSERC, the JCMT Group of the National Research Council, and the Central Research Fund of the University.

Charles Cunningham must be thanked for traveling a long distance to be the external examiner at the final oral examination.

And finally, I thank all the AMC people for creating a cheerful and stimulating environment in which to work.

Table of Contents

Chapter 1: Introduction

1.0 Introduction 1

1.1 Applications 1

1.2 Receiver technology 1

  1.2.1 Waveguide-based mixers 3

  1.2.2 Integrated mixer designs 4

1.3 The work in this thesis 7

1.4 References 8

Chapter 2: Experiments in Bias-Tuning of SIS Mixers

2.0 Introduction 10

2.1 Quantum admittance of SIS junction at millimetre wavelengths 10

  2.1.1 Computer procedure for analyzing SIS I-V curves 11

  2.1.2 Plots of SIS I-V curve and quantum admittance 12

  2.1.3 Physical meaning of quantum susceptance 15

  2.1.4 A mixer with an electrically adjustable tuner 15

  2.1.5 Bias-tuned mixer 16

2.2 Waveguide probe with constant conductance tuning 18

  2.2.1 Model measurements 20

  2.2.2 Electromagnetic simulations 21

  2.2.3 Low-pass filter design 24

2.3 RF circuit design 25

2.4 Precision mixer block design 27

2.4.1 Split waveguide with alignment keys 27
2.4.2 Diagonal horn antenna 30
2.4.3 Non-contacting backshort 30
2.5 SIS fabrication 31
2.5.1 Summary of fabrication process....................31
2.5.2 Anodization spectroscopy of trilayers....................33
2.5.3 Remaining problems with SIS devices 36
2.6 Measurements 37
2.6.1 Test setup 37
2.6.2 Noise temperatures....................38
2.6.3 Pumped I-V curves....................39
2.7 Analysis....................41
2.7.1 Measurement errors....................41
2.7.2 Voltage match method 42
2.7.3 Results....................44
2.7.4 Comparison with "ideal" SIS junction....................49
2.8 Conclusions....................53
2.9 References....................54

Chapter 3: An Integrated Josephson Current Suppression Electromagnet for SIS Receivers

3.0 Introduction....................58
3.1 Theory of Josephson current suppression 58
3.2 The technique....................60
3.3 Verification 64

- 3.3.1 Verification with a receiver 64
- 3.3.2 Verification with a DC SQUID 66

3.4 Practical concerns 68

3.5 Conclusions 69

3.6 References 69

Chapter 4: Evaluation of a Diagonal Horn Fed with Micromachined Waveguide

4.0 Introduction 71

4.1 Silicon micromachined waveguide 71

- 4.1.1 Etching of silicon 73
- 4.1.2 Problems with micromachined waveguide 75

4.2 Diagonal horn antenna 75

4.3 Experiments 78

- 4.3.1 Standard horn 80
- 4.3.2 Four-wafer waveguide experiments 82
- 4.3.3 Modified waveguide structure 83
- 4.3.4 Flat-sided inserts 84
- 4.3.5 Inserts with curved walls 87
- 4.3.6 Proper modeling of undercut 89

4.4 Discussion 91

- 4.4.1 Conclusions 91
- 4.4.2 Recommendations for future work 92

4.5 References 92

Chapter 5: Conclusions

5.0 Conclusions 94

Appendix: An Outline of Superconducting Electronics

A.0 Introduction 95
A.1 Microscopic superconductivity 95
  A.1.1 Conduction in normal metals 96
  A.1.2 BCS superconductivity 98
A.2 Quasiparticle tunnel junctions 102
  A.2.1 Tunneling theory 102
  A.2.2 RF properties of a superconducting tunnel junction 105
A.3 Electromagnetic properties of superconductors 111
  A.3.1 London equations 111
  A.3.2 Magnetic penetration depth 113
  A.3.3 Superconducting transmission lines 113
  A.3.4 Two-fluid model 117
A.4 Superconducting quantum interference devices (SQUIDs) 118
  A.4.1 The Josephson junction as an RF signal source 118
  A.4.2 Inductance measurement using SQUIDs 119
A.5 Conclusions 121
A.6 References 121

List of Tables

2.1 July 21, 1994 noise measurements at 110 GHz 39

2.2 July 28, 1994 noise measurements at 110 GHz 39

2.3 Total power detection peak and amplitude vs. backshort tuning 45

List of Figures

1.1 A block diagram of a radio astronomy receiver 2

1.2 A cross-section through a waveguide mixer block 3

1.3 Cross-section of a lens-substrate antenna 5

1.4 Exciting antenna geometries used in lens-substrate antennas 6

1.5 A cross-section through a silicon micromachined horn antenna 7

2.1 Unpumped I-V curve of a single 1×1 μm^2 SIS junction. 13

2.2 Quantum conductance of the SIS junction in Figure 2.1 at 110 GHz. 14

2.3 Quantum susceptance of the SIS junction in Figure 2.1 at 110 GHz. 15

2.4 Quantum susceptance of an SIS junction at various frequencies 17

2.5 Predicted tuning bandwidth as a function of centre frequency 18

2.6 A reduced equivalent circuit representation of the bias-tuned mixer 19

2.7 A perspective view of the waveguide probe suspended across waveguide 19

2.8 Measured probe admittances from the scale model 20

2.9 Diagram of waveguide probe model used in the electromagnetic simulator. 22

2.10 Plot of simulated feed point admittances for the waveguide probe. 23

2.11 Examples of transmission line structures used in the receiver design 26

2.12 Photograph of an SIS mixer device similar to the one used 27

2.13 Diagram showing how the waveguide slot and the alignment slots were cut into the mixer block 28

2.14 Diagram of mixer block showing the transverse mounting channel 29

2.15 Photograph of the assembled mixer block 29

2.16 Cross-section through the backshort, waveguide, and wafer 31

2.17 Cross-section through a niobium SIS device 32

2.18 Schematic of test apparatus for anodization spectroscopy of trilayers 34

2.19 Anodization spectroscopy curve for a trilayer with a thin base layer 35

2.20 Anodization spectroscopy curve for a trilayer with a thick base layer 35

2.21 Pumped I-V curves for various backshort positions 40

2.22 Pumped I-V curves for various backshort positions 41

2.23 Mixer model for the voltage match method. 43

2.24 Smith chart showing the embedding admittance points 46

2.25 Smith chart showing the embedding admittance points 47

2.26 Contour plot of the voltage match error function 48

2.27 Plot of the unpumped I-V curve, photon steps, and fitted points 49

2.28 Simulated detected power curves using the experimental I-V curve 50

2.29 Simulated detected power curves using the experimental I-V curve 51

2.30 Simulated detected power curves using the ideal I-V curve 52

3.1 The suppression of the Josephson current by a magnetic field 60

3.2 Schematic of SIS mixer before modifications 61

3.3 Schematic of SIS mixer modified with an integrated Josephson effect suppression electromagnet 62

3.4 A perspective view of a cut through a microstrip line carrying current 63

3.5 Design of RF mixer circuit with an integrated Josephson suppression electromagnet 66

3.6 Schematic representation of the DC SQUID circuit used to demonstrate Josephson current suppression 67

3.7 Plot of Josephson current as a function of control current 68

4.1 Silicon micromachined waveguide. 72

4.2 Comparison of modes in waveguide and stripline against substrate thickness 73

4.3 An illustration of anisotropic and isotropic etching. 74

4.4 The family of <111> planes looking down into a <110> Si wafer 75

4.5 Vector plots of the electric fields in the diagonal horn 76

4.6 Vector field plot of the resultant of the addition of the TE_{10} and TE_{01} modes 77

4.7 Plot of the amplitude of the diagonal horn electric fields aligned in the co-polarized direction 78

4.8 Plot of the amplitude of the cross-polarized electric fields in the diagonal horn 78

4.9 Perspective view of diagonal horn 79

4.10 Co-polarization radiation patterns for standard diagonal horn 81

4.11 E plane cross-polarization radiation pattern (dashed line) plotted with co-polarized pattern 81

4.12 Diagonal horn using micromachined waveguide based on a four wafer stack 82

4.13 E plane, H plane, and D plane radiation patterns for diagonal horn shown in Figure 4.12 83

4.14 Diagonal horns with the modified silicon micromachined waveguide 84

4.15 Horn with inserts that have flat flare sides representing minimal isotropic undercut 85

4.16 Co-polarized radiation pattern of diagonal horn with modified micromachined waveguide 86

4.17 Co- and cross-polarized radiation patterns in the D plane of diagonal horn with modified micromachined waveguide 86

4.18 Diagonal horn with inserts simulating a constant radius undercut 87

4.19 Co-polarized radiation patterns for horn with inserts simulating a constant radius undercut along the horn flare 88

4.20 D plane radiation patterns of horn with inserts simulating constant radius undercut 88

4.21 Geometry of the intersection of the isotropic and anisotropic etches in the transition from waveguide to horn 89

4.22 Co-polarized radiation patterns of the diagonal horn with the undercut properly modeled....90

4.23 Co- and cross-polarized radiation patterns for the horn with undercut properly modeled....90

4.24 A section through the diagonal horn showing the profiles of the standard horn, flat sided flare, and undercut flare 91

A.1 Probability of occupancy versus electron energy. 96

A.2 Hole and electron excitations in a normal metal. 97

A.3 Two representations of electron and hole excitations in a normal conductor 98

A.4 Excitations from the superconducting ground state. 100

A.5 Energies of quasiparticle excitations 101

A.6 Density of quasiparticle states. 102

A.7 Density of states representation of normal - superconductor tunneling. 103

A.8 Density of states representation of SIS quasiparticle tunneling. 104

A.9 IV characteristic of a SIS junction. 105

A.10 Junction IV curve and its Kramers-Kronig transform. 108

A.11 Junction IV curve with and without local oscillator. 109

A.12 Quantum conductance of SIS junction. 110

A.13 Quantum susceptance of SIS junction. 110

A.14 Geometry of microstrip transmission line showing the volume of integration. 114

A.15 Schematic representation of two fluid model of current through a superconductor. 117

A.16 Schematic of SQUID 120

Chapter 1:

Introduction

1.0 Introduction

The last frontiers for radio engineering are the millimetre- and submillimetre-wave bands, located between microwaves and infrared waves in the electromagnetic spectrum. It is an interesting regime, since it is where classical physics and quantum physics meet and it is where there is the choice between wire-like transmission lines and optical guiding structures. However, this region of the spectrum is not without its difficulties. Except for Schottky diodes, semiconductor devices do not work well at such high frequencies, making it difficult to generate signals of significant strength in the submillimetre-band. The most sensitive detectors, which this thesis is partly about, require cooling to liquid helium temperatures. Yet another difficulty is the fact that the dimensions and tolerances needed to build systems are often between what can easily be done with metal machining and what can be made with integrated circuit fabrication techniques. This thesis describes several attempts to overcome difficulties in building systems at these wavelengths.

1.1 Applications

One of the main forces driving the development of millimetre and submillimetre instrumentation is radio astronomy. Astronomers observe the sky at as many wavelengths as possible because different phenomena are visible at different wavelengths. The range from 100 to 1000 GHz is important because it is where star formation is best studied. What astronomers observe is the emission lines of the infalling gas as the gravitational potential energy is dissipated [1]. This study cannot be done at shorter wavelengths because the gas is opaque. At longer wavelengths the radiation does not contain the spectral lines from which information about the gas temperature, velocity, and pressure can be obtained. These observations look at not only our own galaxy but others as well.

A major problem encountered by astronomers at these wavelengths is attenuation due to oxygen and water vapour in the atmosphere. This has forced astronomers to site their instruments in dry deserts or at high elevations, such as the summit of Mauna Kea on the island of Hawaii. However, even at these elevations, the atmosphere is still significantly absorbing and the amount of absorption is dependent on the weather and hence quite variable. For this reason there is a strong need to maximize the efficiency of the telescope when the weather is good. One way to do this for spatial mapping observations is to make an array of side-by-side receiver elements. This would form a radio camera and reduce the time required for a single mapping observation.

1.2 Receiver technology

A brief overview of millimetre-wave receiver technology will be given here. The emphasis will be on heterodyne detectors (i.e., frequency conversion by mixing) rather than direct detectors, such as by bolometers. Receivers based on superconducting tunnel diodes (superconductor-insulator-superconductor or SIS junctions) will be stressed over those using Schottky barrier diodes because of the greater sensitivity and the lower local oscillator (LO) power requirements of the superconducting technology. The coverage here will be cursory, with just enough information to allow the reader to follow the rest of the thesis. Several references provide a more complete survey of the field [2, 3, 4]

Heterodyne receivers at millimetre- and submillimetre-wavelengths are constructed in a similar manner to the block diagram in Figure 1.1. For systems using superconducting devices the mixer is cooled to 4K with liquid helium. In systems like this, the entire chain from antenna to intermediate frequency (IF) amplifier is cooled while the bias supply and LO are at room temperature. This system works by optically combining the signal with the LO. The diagram suggests a partially transmitting/partially reflecting beam splitter, and this is indeed what is used in many systems. The signal and LO are coupled into the same antenna which is connected to the mixer. The difference signal is passed through the isolator and the bias tee to the IF amplifier. An isolator is often needed to prevent oscillations in the IF amplifier when the mixer has a negative output impedance. The bias tee is required since the bias and the output of the mixer share the same line. A low-noise, high gain IF amplifier is essential because the mixer usually has a conversion loss of between 0 and 8 dB, the effect of which is to increase the noise contribution of the IF amplifier to the overall noise. The signal is then analyzed with a spectrometer that integrates the signal and displays the received power as a function of frequency.

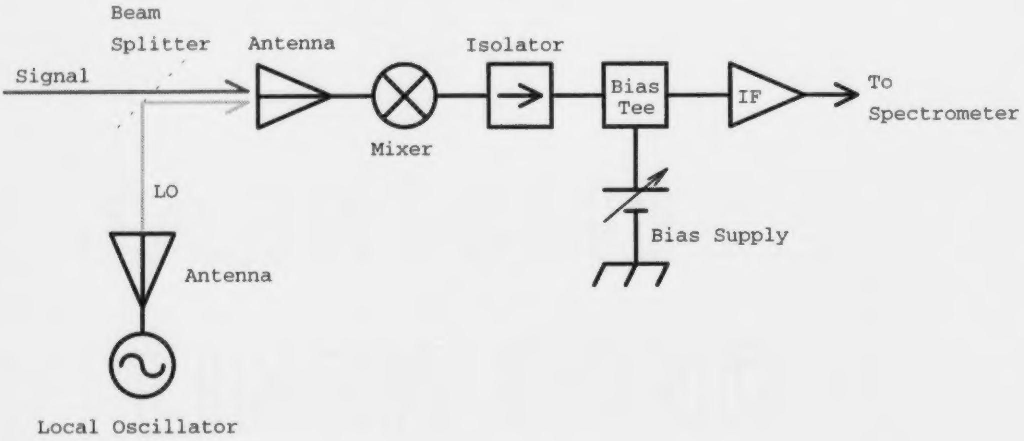

Figure 1.1: A block diagram of a radio astronomy receiver for millimetre and submillimetre wavelengths.

1.2.1 Waveguide-based mixers

The first millimeter-band mixers were constructed using waveguide circuits [5, 6]. One reason for this was that it was a natural progression from the waveguide circuits used at centimetre-wavelengths. So when SIS tunnel junctions were first used as mixers, they were used in modified Schottky mixer blocks [7]. After the first laboratory results of heterodyne mixing, the SIS devices were soon put into use on radio telescopes [8].

It is now useful to look at a waveguide mixer design in more detail to appreciate the level of complexity. Figure 1.2 shows a successful mixer design. Although this particular mixer was built to operate near 230 GHz, the design has since been scaled to other frequencies including 345, 490, and 690 GHz with good results.

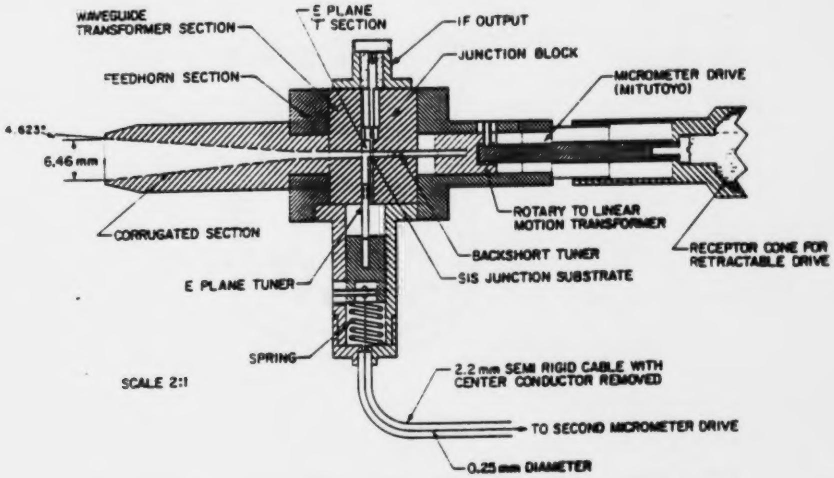
WAVEGUIDE TRANSFORMER SECTION
E PLANE 'T' SECTION
IF OUTPUT
JUNCTION BLOCK
FEEDHORN SECTION
MICROMETER DRIVE (MITUTOYO)
4.623°
6.46 mm
ROTARY TO LINEAR MOTION TRANSFORMER
CORRUGATED SECTION
BACKSHORT TUNER
RECEPTOR CONE FOR RETRACTABLE DRIVE
E PLANE TUNER
SIS JUNCTION SUBSTRATE
SPRING
SCALE 2:1
2.2 mm SEMI RIGID CABLE WITH CENTER CONDUCTOR REMOVED
TO SECOND MICROMETER DRIVE
0.25 mm DIAMETER

Figure 1.2: A cross-section through a waveguide mixer block showing the complex construction. (From Figure 4 in [9].)

The input to the mixer block is the feed horn. Corrugated horns [10] are often used because they have a symmetric Gaussian-shaped far-field radiation pattern with low sidelobes. The Gaussian response is desirable because it is well matched to the quasi-optical beams found in telescopes. The main disadvantage with this design is that it is very difficult to build, particularly at millimetre- and submillimetre-wavelengths. This is because the inner surface of the horn is covered with circumferential grooves $\lambda/4$ deep with a width of less than $\lambda/4$. Although at centimetre-wavelengths it is possible to fabricate the horn in pieces or to fit machine tools inside it, those techniques will not work for shorter wavelengths. Instead, a sacrificial mandrel is machined on a lathe to the complement of the inner shape of the horn. The mandrel is then electrochemically plated ("electroformed") with copper. Once the required wall thickness is achieved, the aluminum mandrel is etched away, leaving a corrugated feed horn. Clearly these horns are very expensive, not only because of the intricate machining, but also because the tooling is destroyed each time one is made.

The remainder of the mixer block is much simpler. It consists of a waveguide (which may be reduced height) with a channel for mounting the small wafer carrying the SIS device, and an orthogonal section of waveguide $\lambda/2$ in front of the SIS wafer. This second section of waveguide is used to form an E plane tuner. A backshort tuner occupies the waveguide following the SIS wafer. The two tuners allow a wide range of SIS device impedances to be matched to the waveguide impedance. At 345 GHz and higher frequencies, an additional complexity of the mixer is the addition of magnetic flux concentrators so that a superconducting electromagnet can be used to suppress the DC Josephson effect.

Mixers of this type are very expensive, costing about $25,000 each. Clearly this technology is very unattractive for array receivers since a modest array of 4×4 elements would cost $400,000 for the mixer blocks alone, excluding the cryogenics, the LO, the IF, and the spectrometers. The waveguide design is also unattractive because tuners, electromagnets, and RF connectors occupy space on the sides of the mixer, making close-packing difficult. For these reasons, much effort has been spent to find alternative structures that take advantage of transmission lines and antennas formed using variations of integrated circuit techniques.

1.2.2 Integrated mixer designs

One solution to the problems with waveguide circuits is to adapt microwave printed circuit elements to higher frequencies by using the technology of integrated circuit (IC) fabrication. The advantages of IC technology, including batch processing, high reproducibility, and small size, are then transferred to millimetre- and submillimetre-wave technology. Some microwave components, such as microstrip transmission lines and co-planar waveguide, are easily adapted. Others, such as antennas, do not transfer as well. For example, microstrip patch antennas are not well suited for millimetre-wavelengths because they have a narrow frequency bandwidth and have a wide radiation pattern. Therefore, an area of much interest has been the development of lithographically-formed antennas for shorter wavelengths. The fundamental problem with integrated circuit antennas is the excitation of surface modes into the supporting dielectric [11]. Two solutions exist for this problem: make the dielectric substrate appear infinitely thick or make it appear infinitely thin. Families of antennas have been invented for each solution and will be outlined below.

When an antenna is placed onto an air-dielectric interface, the coupling is strongest into the dielectric [12]. If the dielectric is a slab, then a parallel plate waveguide is set up for waves with an angle of incidence such that total internal reflection is supported. Such trapped modes, or surface waves, reduce the efficiency of the antenna, and also introduce resonances into the frequency response. A solution to this problem is to make the dielectric appear to extend to infinity so that none of the energy radiated into the substrate is trapped. A simple way to do this is to use a hemisphere of dielectric as the substrate. Then, with an antireflection coating on the curved surface, the substrate appears to extend forever. A further refinement is the addition of a dielectric extension off the back of the hemisphere to form a hyperhemisphere. By varying the extension, the radiation pattern can be adjusted [13]. An example of this is shown in Figure 1.3.

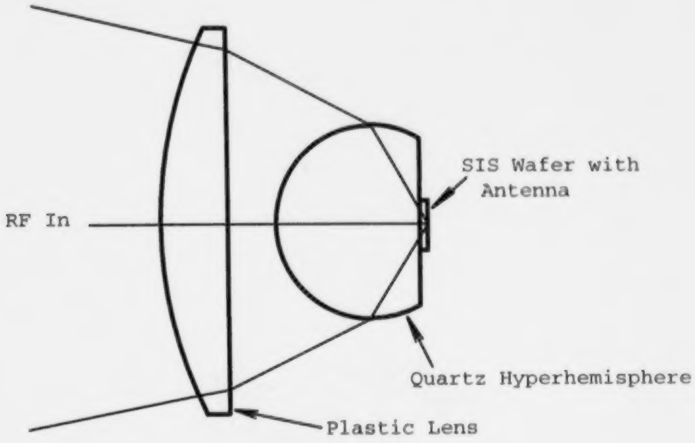

Figure 1.3: Cross-section of a lens-substrate antenna showing incident rays focused onto a planar antenna. The additional plastic lens is used to match the beam of the telescope to the beam of the lens-substrate antenna. (From Figure 1 of [18].)

Early work with this idea used a bow-tie shaped exciting antenna and was done by Rutledge and Muha [14]. Wengler *et al.* [15] then built an SIS receiver based on that work. Not only was this mixer easier to construct than a waveguide mixer, it had a greater operating bandwidth. However, it soon became apparent that the bow-tie was not a good radiating element since most of the power was radiated away from the perpendicular axis [16]. Other antenna designs have since been used, including log periodics, spirals [17], and slots [18], and have provided results similar to those that waveguide-based systems achieve. These different types are shown in Figure 1.4.

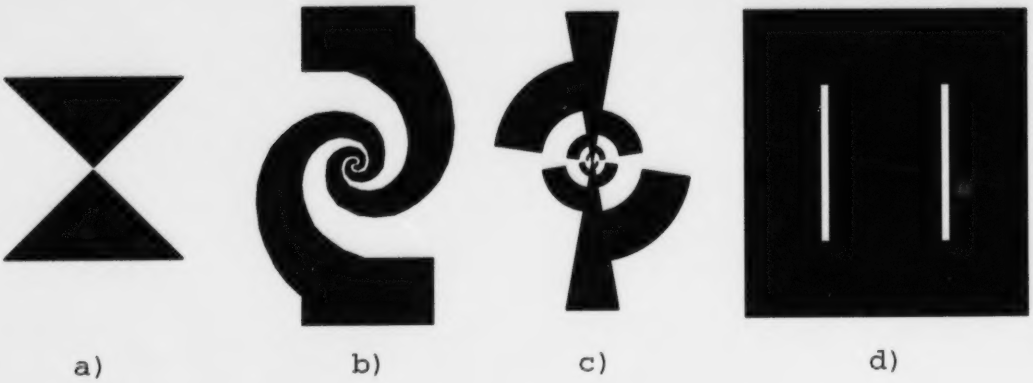

Figure 1.4: Exciting antenna geometries used in lens-substrate antennas. A bow-tie antenna is shown in a), a spiral antenna in b), a log-periodic antenna in c), and an array of parallel slots in d). Dark print represents metallization. The feed points of the first three antennas are at the centre; the slot antennas are fed by a microstrip circuit not shown here.

The other approach to the surface wave problem is to make the substrate thickness much less than a wavelength so that the substrate becomes invisible. This technique is ideally suited for silicon-based designs since thin nitride films are easily grown on silicon, and then the underlying silicon can be etched away leaving a film about 1 µm thick. Another advantage of silicon is that it can be selectively etched along certain crystal planes. For example, a wafer oriented so that the surface is the <100> crystal plane can be etched so that pyramidal holes are formed bounded by the <111> planes. Rebeiz *et al.* [19] have used these techniques to make a pyramidal horn. An important disadvantage of this antenna is the fact that the flare of the horn opening is restricted to 70.6° by the crystal planes. This limits the size and gain of the antenna since large apertures will have a significant phase error across the aperture. One solution that has worked well is to attach a metal machined extension to the horn [20]. The gradual taper of the extension results in a better phase distribution across the aperture and hence a good quality radiation pattern. A cross-section through this horn is shown in Figure 1.5.

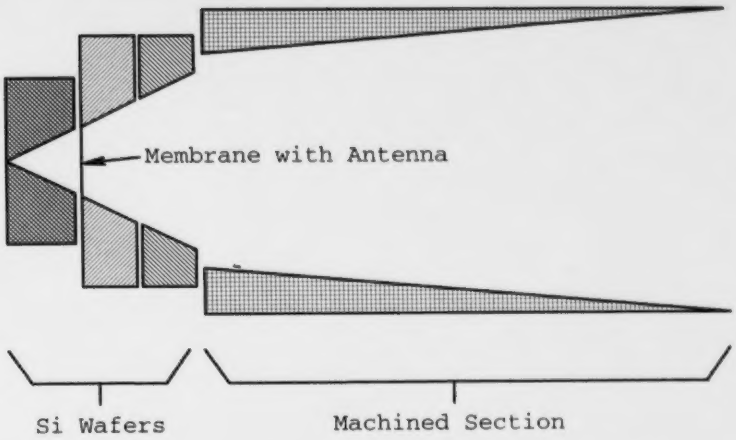

Figure 1.5: A cross-section through a silicon micromachined horn antenna. The opening angle of the horn integrated in silicon is 70.6°. The flare angle of the metal machined section to the right is set to 9° to reduce phase errors across the aperture on the right-hand side. (From Figure 1 of [20].)

The antennas described above are examples of several successful designs and many more exist. A more complete review of integrated circuit antennas can be found in [21].

This introduction has shown how integrated circuit fabrication techniques have been used to ease the difficulty of fabricating millimetre and submillimetre systems. However, there are still problems to be solved. The definition of electromagnetic structures with photolithographic etching has made those structures fixed. Thus there is no longer a convenient tuning mechanism. Also, there may be other parts of the receiving system that can be integrated along with the antenna, active device, and transmission lines. Finally, there may be other antenna structures that could be useful.

1.3 The work in this thesis

The purpose of the work reported in this thesis was to develop techniques that would ease some of the problems encountered by developers of millimetre and submillimetre instrumentation. In particular, it was hoped that these techniques would aid in the development of focal plane arrays.

The first set of experiments describe the efforts to demonstrate a bias-tuning technique for SIS receivers. This was intended to alleviate some of the problems in working with fixed-tuned circuits. Although this method was not successful, a number of techniques which were developed may be of use in future designs. These include a method for precise construction of a waveguide mixer using conventional machining tools and computer-aided design of waveguide probes.

The next body of work involved the integration of Josephson effect suppression magnets onto the same chip as the SIS device. By doing so, the overall size and mass of a mixer can be reduced by eliminating electromagnets external to the mixer. This will simplify the construction of a focal plane array receiver.

The final set of experiments studied the possibility of integrating a silicon micromachined waveguide with a horn antenna. This work shows that a waveguide, probe, and active device could be fabricated using IC processing technology and then clamped between two metal blocks with tapered V-grooves to complete the horn aperture. Like many other IC antennas, this one requires ancillary structures made by other techniques to complete the radiating aperture.

Following the conclusion is an appendix with an outline of superconductivity. This was included because the subject is not a usual part of electrical engineering curricula. By placing this outline at the end of the thesis, the flow is made smoother for readers who do have a background in superconductivity.

1.4 References

[1] T. G. Phillips, J. B. Keene, "Submillimeter Astronomy," *Proc. IEEE*, vol. 80, pp. 1662-1678, 1992

[2] T. G. Phillips, D. P. Woody, "Millimeter- and submillimetre-wave receivers," *Ann. Rev. Astron. Astrophys.*, vol. 20, pp. 285-321, 1982

[3] J. W. Archer, "Low-noise heterodyne receivers for near-millimeter-wave radio astronomy," *Proc. IEEE*, vol. 73, pp. 109-130, 1985

[4] R. Blundell, C.-Y. E. Tong, "Submillimetre receivers for radio astronomy," *Proc. IEEE*, vol. 80, pp. 1702-1720, 1992

[5] W. M. Sharpless, "Wafer-type millimeter wave rectifiers," *Bell Syst. Tech. J.*, vol. 35, pp. 1385-1402, 1956

[6] A. R. Kerr, "Low-noise room-temperature and cryogenic mixers for 80-120 GHz," *IEEE Trans. MTT*, vol. 23, pp. 781-787, 1975

[7] T. G. Phillips, D. P. Woody, G. J. Dolan, R. E. Miller, and R. A. Link, "Dayem-Martin (SIS tunnel junction) mixers for low noise heterodyne receivers," *IEEE Trans. MAG*, vol. 17, pp. 684-689, 1981

[8] D. P. Woody, R. E. Miller, and M. J. Wengler, "85 to 115 GHz receivers for radio astronomy," *IEEE Trans. MTT*, vol. 33, pp. 90-95, 1985

[9] B. N. Ellison, R. E. Miller, "A low-noise 230 GHz SIS receiver," *Int. J. Infrared Millimeter Waves*, vol. 8, pp. 609-626, 1987

[10] B. MacA. Thomas, "Design of corrugated conical horns," *IEEE Trans Antennas Propagat.*, vol. 26, pp. 367-372, 1978

[11] D. B. Rutledge, D. P. Neikirk, D. P. Kasilingam, "Integrated-circuit antennas," *Infrared and Millimeter Waves*, vol. 10, K. J. Button, ed., New York: Academic Press, pp. 1-90, 1983

[12] C. R. Brewitt-Taylor, D. J. Gunton, H. D. Rees, "Planar antennas on a dielectric surface," *Electronics Lett.*, vol. 17, pp. 729-731, 1981

[13] D. F. Filipovic, G. M. Rebeiz, "Double-slot antennas on extended hemispherical and elliptical quartz dielectric lenses," *Int. J. Infrared Millimeter Waves*, vol. 14, pp. 1905-1924, 1993

[14] D. B. Rutledge, M. S. Muha, "Imaging antenna arrays," *IEEE Trans. Antennas Propagat.*, vol. 30, pp. 535-540, 1982

[15] M. J. Wengler, D. P. Woody, R. E. Miller, and T. G. Phillips, "A low noise receiver for millimeter and submillimeter wavelengths," *Int. J. Infrared Millimeter Waves*, vol. 6, pp. 697-706, 1985

[16] R. C. Compton, R. C. MacPhedran, Z. Popovic, G. M. Rebeiz, P. P. Tong, and D. B. Rutledge, "Bow-tie antennas on a dielectric half-space: theory and experiment," *IEEE Trans Antennas Propagat.*, vol. 35, pp. 622-631, 1987

[17] T. H. Büttgenbach, "An improved solution for integrated array optics in quasi-optical mm and submm receivers: the hybrid antenna," *IEEE Trans. MTT*, vol. 41, pp. 1750-1761, 1993

[18] J. Zmuidzinas, H. G. Leduc, "Quasi-optical slot antenna SIS mixers," *IEEE Trans. MTT*, vol. 40, pp. 1797-1804, 1992

[19] G. M. Rebeiz, D. P. Kasilingam, Y. Guo, P. A. Stimson, D. B. Rutledge, "Monolithic millimeter-wave two-dimensional horn imaging arrays," *IEEE Trans. Antennas Propagat.*, vol. 38, pp. 1473-1482, 1990

[20] G. V. Eleftheriades, W. Y. Ali-Ahmad, G. M. Rebeiz, "A 20-dB quasi-integrated horn antenna," *IEEE Microwave Guided Wave Lett.*, vol. 2, pp. 73-75, 1992

[21] G. M. Rebeiz, "Millimeter-wave and terahertz integrated circuit antennas," *Proc. IEEE*, vol. 80, pp. 1748-1770, 1992

Chapter 2:

Experiments in Bias-Tuning of SIS Mixers

2.0 Introduction

Over the last decade the design of superconductor-insulator-superconductor (SIS) mixers has changed dramatically. In the past receivers were built with waveguide horns and delicate lead alloy SIS junctions, and were tuned with sliding shorts in waveguide. Now receivers use planar antennas defined by photolithography, robust niobium SIS junctions, and fixed microstrip networks to match the antenna impedance to the SIS device impedance. Although this new technology has produced very sensitive receivers at higher frequencies, problems remain. The microstrip matching networks have been made broadband by compromising the impedance match across the frequency band of interest. So although receivers are more sensitive than ever, the receiver noise is still about five times greater than predicted by theory. Another problem is the accuracy to which the junction areas, junction barrier thickness, and transmission line widths can be made. Variations in these parameters will detune the mixer. Thus there is a need for an adjustable component in SIS mixers. Although mechanical tuners for planar transmission lines have been proposed [1], these are likely to be difficult to fabricate and to use. Clearly an electrically adjustable tuning device that is compatible with SIS fabrication technology would be desirable.

This chapter discusses the possibility of using the SIS junction itself as a tuning device. It begins with a description of the radio frequency (RF) properties of SIS junctions and how these might be used as a tuning mechanism, then moves onto the design of a special waveguide probe and a precision waveguide mixer block. A brief discussion of SIS device fabrication follows. After that, a description of the test receiver, the measurements, and analysis are presented. Finally, the conclusions for this work are presented.

2.1 Quantum admittance of SIS junctions at millimetre wavelengths

Unlike classical resistive mixers, quantum mixers such as SIS junctions display a reactive component in addition to the usual resistive component at the signal and local oscillator frequencies. This section will show how these quantities can be calculated and how the reactive component might be used to electrically tune an SIS mixer. An overview of tunneling theory can be found in section A.2.1 of the Appendix, and the RF properties of SIS junctions are outlined in section A.2.2.

Although the theoretical basis of the quantum susceptance has been known for some time [2, 3], only recently has this phenomenon been measured. Hu *et al.* [4] used a Fourier transform spectrometer to measure the frequency response of an SIS junction coupled to an open-circuited stub and a broadband antenna. As the bias voltage of the junction was changed, they observed a change in the resonant frequency. This was due to the quantum susceptance and its dependence upon the bias. This was verified by simulating the circuit with and without the quantum susceptance: without it, the frequency response was flat.

The quantum susceptance was then measured *directly* by Worsham *et al.* [5]. They used a slotted waveguide probe to measure the standing wave pattern of an SIS device driven by an 87 GHz oscillator. The receiver used a broadband waveguide-to-microstrip transition [6]. From the standing wave pattern the junction admittance was determined as a function of SIS bias voltage. Their measured curves agreed well with curves derived from the DC I-V curve using Tucker's theory [7].

Examining the results of Worsham *et al.* it can be seen that the junction susceptance due to the geometric capacitance, about +100 mS, could easily be tuned out by the quantum susceptance of the SIS junction, which varied between -200 and +100 mS. Thus it should be possible to use an SIS device as an electrically-adjustable tuning element.

2.1.1 Computer procedure for analyzing SIS I-V curves

In the investigations reported in this thesis, measured SIS I-V curves were analyzed with a set of functions based on Tucker's theory [7]. These routines were used to determine the RF parameters of a particular device, predict the I-V curve when used in a receiver, and to determine the embedding admittance.

The I-V curve was digitized in voltage steps of 0.05 mV. Since SIS I-V curves are odd functions (i.e. $I[-V] = -I[V]$), only the positive part of the curve was digitized. Data between zero and ~1.7 mV was not used because the Josephson effect obscured the quasiparticle tunneling curve. Instead points were generated by linear interpolation between $I(0) = 0$ and the first reliable quasiparticle tunneling point. This linear curve is what would be seen if the Josephson effect was completely suppressed with a magnetic field.

Taking the Kramers-Kronig transform (see A.2.2) of the data had several difficulties. The first was how to deal with the discrete nature of the input data. Simply doing a linear interpolation between points is not sufficient since the higher-order derivatives of the I-V curve must exist so that a correct Kramers-Kronig transform is obtained [8]. Thus a third-order polynomial was used to interpolate between the points in the numerical integration. Another problem was that the transform was computationally inefficient because the input is defined as double sided, half of which for SIS I-V curves is redundant. The solution was to write the transform in a single-sided form so the integration started at zero and ran to infinity [9]:

$$I_{KK}(V) = \frac{1}{\pi} P \int_{-\infty}^{\infty} \frac{I_{DC}(V')}{V' - V} dV' = \frac{2}{\pi} P \int_{0}^{\infty} \frac{I_{DC}(V')V'}{V'^2 - V^2} dV'. \qquad (2.1)$$

The problem was then made bound by subtracting a linear slope from the I-V curve data so that beyond the data set, the input data were zero. The effect of this modification on the transformed data was a vertical shift, which was unimportant since subsequent functions worked with *differences* of the transformed data. The P in the equation refers to the Cauchy Principal Value, a procedure necessary because of the pole in the denominator of the integral. In the computer code this was realized by integrating to within 0.001 mV of V, skipping 0.001 mV past V, then restarting the integration. This transform function was used to generate a set of points on the same voltage interval as the input data for use by later procedures.

A number of useful functions were then written that would determine the device RF parameters from the DC I-V curve. The quantum admittance of an SIS junction was calculated with

$$
\begin{aligned}
G_Q &= \frac{1}{\alpha V_{PS}} \sum_{n=-\infty}^{\infty} J_n(\alpha)\left(J_{n-1}(\alpha) + J_{n+1}(\alpha)\right) I_{DC}\left(V + n V_{PS}\right) \\
B_Q &= \frac{-1}{\alpha V_{PS}} \sum_{n=-\infty}^{\infty} J_n(\alpha)\left(J_{n+1}(\alpha) - J_{n-1}(\alpha)\right) I_{KK}\left(V + n V_{PS}\right)
\end{aligned}
\tag{2.2}
$$

where the photon step size is $V_{PS} = \omega\hbar/e$ and the normalized LO voltage amplitude is $\alpha = V_{LO}/V_{PS}$. In practice the summation series had to be truncated. Errors were found to be very small with summation limits of -10 and +10 if $\alpha < 5$.

The pumped I-V curve was calculated with

$$
I_{pump} = \sum_{n=-\infty}^{\infty} J_n^{\,2}(\alpha) I_{DC}\left(V + n V_{PS}\right). \tag{2.3}
$$

The LO voltage α depends upon the voltage division of the generator voltage V_{gen} between the source impedance Z_S and the junction. Since the junction admittance is also a function of α, α was found by numerically evaluating the roots of

$$
\alpha = \frac{2\,V_{gen}}{\left| Z_S\left(G_Q(\alpha) + jB_Q(\alpha) + j\omega C_{geo}\right) + 1 \right|}. \tag{2.4}
$$

This equation also includes the effect of the geometric capacitance of the junction, C_{geo}.

2.1.2 Plots of SIS I-V curve and quantum admittance

It was instructive to use these functions to plot the quantum conductance and quantum susceptance for a typical SIS junction fabricated at the Alberta Microelectronic Centre (AMC). The measured I-V curve for a 1×1 μm² junction is shown in Figure 2.1. This was used as input data to generate the two subsequent plots.

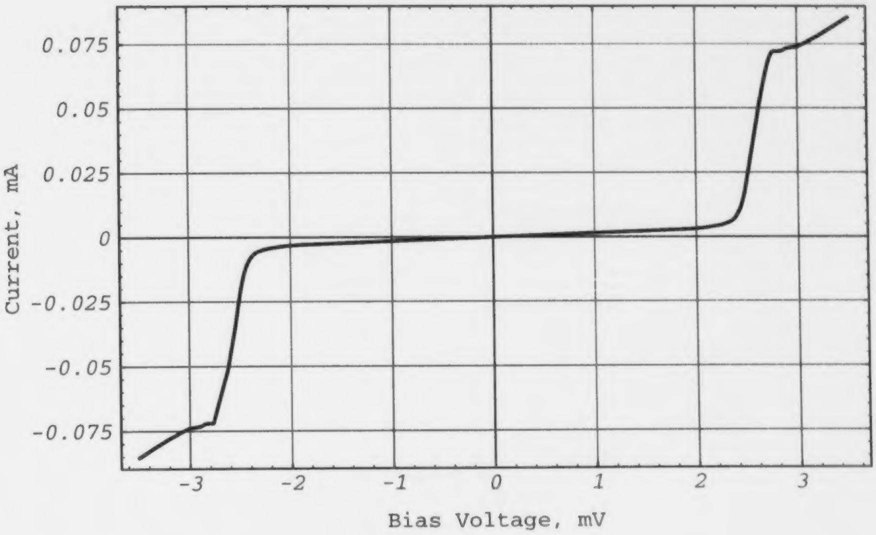

Figure 2.1: Unpumped I-V curve of a single 1×1 μm^2 SIS junction.

Figure 2.2 shows the quantum conductance of the SIS device. What is notable about this curve is that the conductance is almost constant over most of one photon step on either side of the gap voltage. A value for α of 1 was used to generate this figure and Figure 2.3.

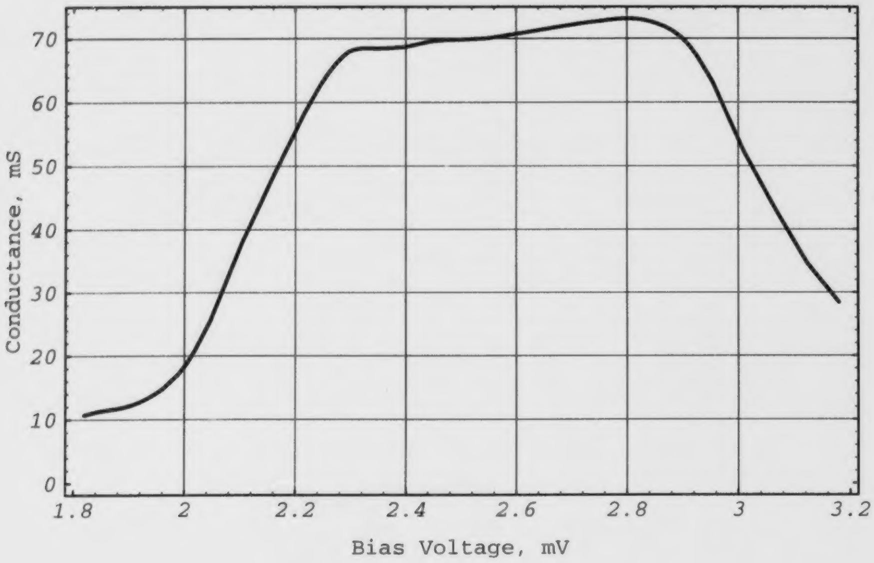

Figure 2.2: Quantum conductance of the SIS junction in Figure 2.1 at 110 GHz.

Figure 2.3 shows the reactive part of the quantum admittance. This plot shows a smooth variation in susceptance across the photon step. For comparison, the susceptance of the junction geometric capacitance is estimated to be ~+30 mS.

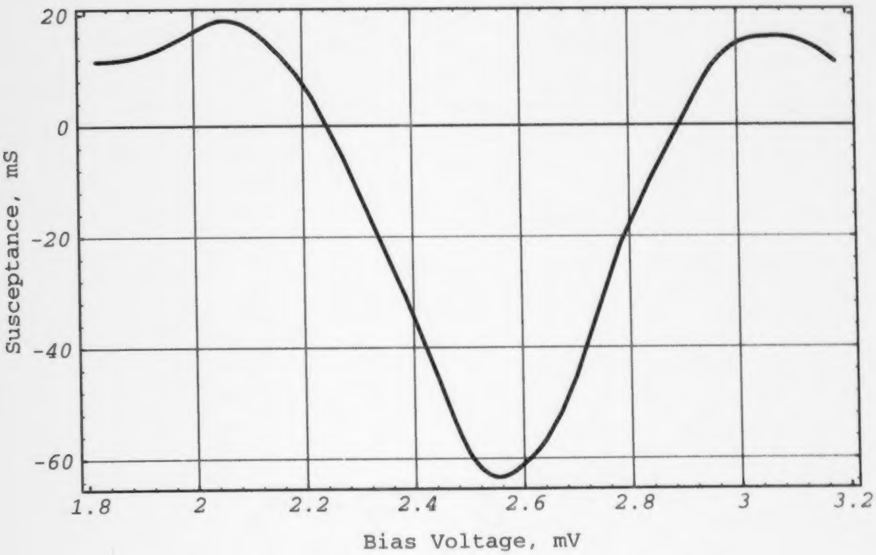

Figure 2.3: Quantum susceptance of the SIS junction in Figure 2.1 at 110 GHz.

2.1.3 Physical meaning of quantum susceptance

The origin of quantum susceptance is often obscured in the mathematics. The key to the origin of this phenomenon is that the relationship between the current flowing through a junction and the voltage across it is not instantaneous. Rather, it is the history of the voltage signal up to the measurement time that determines the current [2].

A more intuitive way to understand this is to realize that all susceptances involve some sort of energy storage. In the tunneling process of SIS junctions, an electron which has tunneled is at an elevated energy level due to the bias voltage and the absorption of a photon. For niobium, the lifetime of that electron is on the order of a nanosecond [10]. If, for example, the incident wave is at a frequency of 100 GHz, it will oscillate about 100 cycles in the electron's lifetime. Thus the electron has many RF cycles to tunnel back to the other electrode and to emit a photon. In this way energy can be stored in, and released from, an SIS junction. Some have referred to this movement to and from the intermittent storage state as "quantum mechanical sloshing" [4].

2.1.4 A mixer with an electrically adjustable tuner

A mixer has been designed by Ugras *et al.* [11] that exploits the change in junction susceptance as a function of bias voltage. It has two sets of junctions: one that performs the mixing, and another that varies the tuning. The two sets of junctions are placed in parallel at RF but have separate DC bias voltages. Measurements were done at 90 GHz in a waveguide mixer block that had fixed mechanical tuning. Photon steps in the I-V curve were observed to change as the bias on the tuning array was changed. The noise temperature of the receiver also changed with tuner bias.

A drawback to this design was an increase in receiver noise temperature due to losses in the tuner junctions. These losses occur because SIS junctions are low-Q devices with the magnitude of the quantum conductance comparable to the quantum susceptance. In this design, the total conductance of the mixing junctions was 61 mS and that of the tuning junctions was 35 mS. Thus about 1/3 of the power was absorbed by the tuner.

2.1.5 Bias-tuned mixer

The susceptance versus bias curve suggests an alternative design that circumvents the problem with the separate tuning junction design. This new design was based on the realization that for all the signal power to be absorbed by the mixing junction, the tuning junction must be part of the mixing junction. This means that the two functions cannot have a separate bias voltage. Thus the tuning was to be accomplished by a variation in the bias voltage of the SIS junction.

Usually SIS mixers are biased in the centre of the first photon step below the gap voltage. One reason for this is that it improves the dynamic range of the receiver. Saturation effects originate from the change in mixer gain as the instantaneous bias point is moved by the intermediate frequency (IF) signal back and forth across the mixer gain curve. Although there is great variation in the shape of these curves, typically they have a parabolic appearance with the maximum at the centre of the photon step. Thus for large amplitude IF signals, the peaks of the waveform are attenuated with respect to the parts near zero, which reduces the overall gain. A hazard of the bias-tuning idea is that the mixer would be more prone to saturation, but this could be minimized by staying away from the edges of the photon step. A good compromise could be to adjust the bias over the middle half of the photon step. In this way a reasonable variation in the susceptance could still be achieved. .

Another problem with this method is that the tuning range is greatest at lower frequencies, rather than at high frequencies. This can be seen in Figure 2.4, which has quantum susceptance plots at 110, 230, 345, 490, and 660 GHz superimposed. Since the photon step size is proportional to frequency, the bias voltage scale has been normalized by photon step size for comparison. The most negative going curve is for 110 GHz, with the others ascending with frequency. It is clear that the variation in susceptance is greatest, and also most linear, for the low frequencies. Since the susceptance variations to be tuned out often *increase* with frequency, this results in a reduction of tuning bandwidth with frequency. This will also be a problem with the tuning method in [11]. However, it should be realized that the percentage bandwidth of the atmospheric windows is largest at the lower frequencies, so the need for tuning is greatest there.

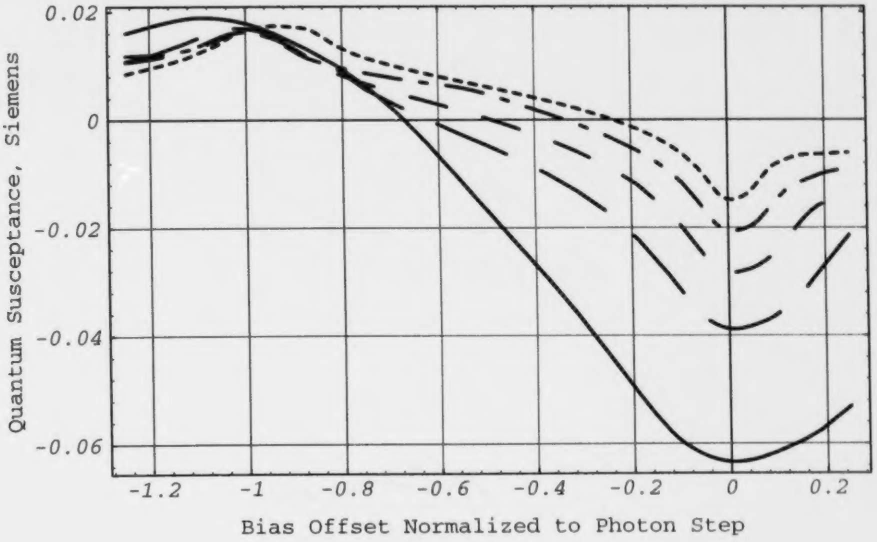

Figure 2.4: Quantum susceptance of an SIS junction at various frequencies, with the voltage bias normalized to the photon step size at the frequency. The solid line is 110 GHz, the line with long dashes is 230 GHz, the line with short dashes is 345 GHz, the line with alternating dots and dashes is 490 GHz, and the dotted line is 660 GHz. Zero bias offset represents the centre of the photon step.

Figure 2.5 shows predicted tuning bandwidth as a function of signal frequency. The model used to generate this plot was a mixer fed from a real and constant antenna impedance and with the geometric capacitance resonated with a fixed inductance at the design centre frequency and with the bias voltage at the centre of the photon step. This is a realistic model for certain planar antennas which have a constant real terminal impedance. The plot was made by varying the bias by ±¼ photon step and finding the two frequencies where the quantum susceptance, the geometric capacitance, and the parallel inductance canceled. The bandwidth was simply the difference between the two frequencies. The plot confirms that this new tuning method will be of most interest for lower frequency designs.

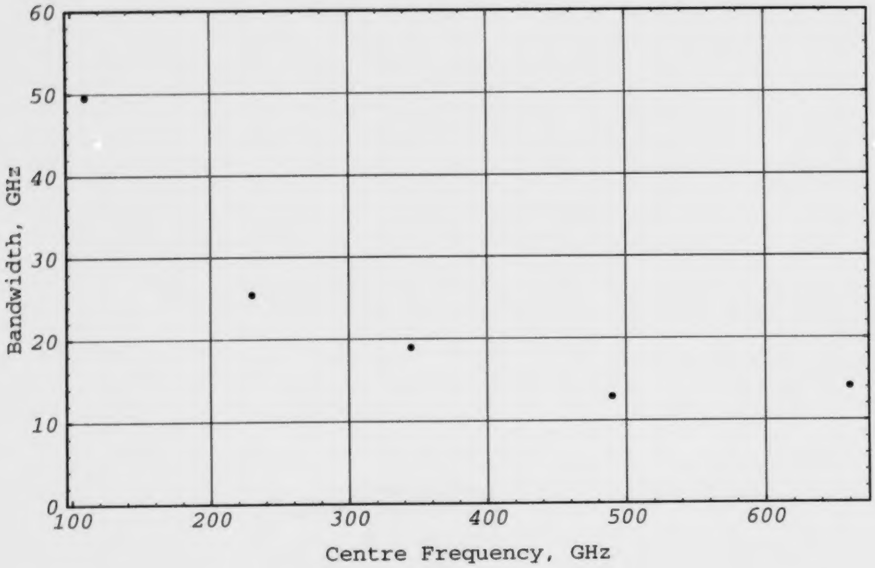

Figure 2.5: Predicted tuning bandwidth as a function of centre frequency for bias tuned mixer.

2.2 Waveguide probe with constant conductance tuning

The fundamental problem addressed in this chapter was to demonstrate the bias-tuning effect. To do this, a special waveguide mixer was built that has a backshort which moves the source admittance on a constant conductance circle on the Smith chart. Thus to demonstrate the bias tuning, the electrically variable component was expected to cancel a change in the mechanically variable component at a fixed frequency. Figure 2.6 shows a simplified equivalent circuit for the mixer.

This design was based on an earlier mixer that was a Schottky diode mixer modified to accept an SIS device. That mixer established some of the design parameters used here, such as the reduced height WR-10 waveguide dimensions of 2.525 mm × .225 mm. Figure 2.7 shows the internal layout of the mixer. The probe was integrated onto a quartz wafer 0.5 mm wide × 6.0 mm long × 0.07 mm thick. On either side of the bow-tie shaped probe are low-pass filters that reflect 110 GHz signals but allow DC and the 1.5 GHz IF to pass. The filters consist of alternating sections of low and high impedance microstrip line $\lambda_{110}/4$ long. The feed point of the probe is at the points of the two triangles. Not shown is the continuation of the waveguide above the wafer to the horn antenna.

The key point in this design is a probe and a low-pass filter that placed the locus of terminal admittance points onto a constant conductance circle on the Smith chart. That design was determined in two ways, by a physical scale model and by a computer simulation model.

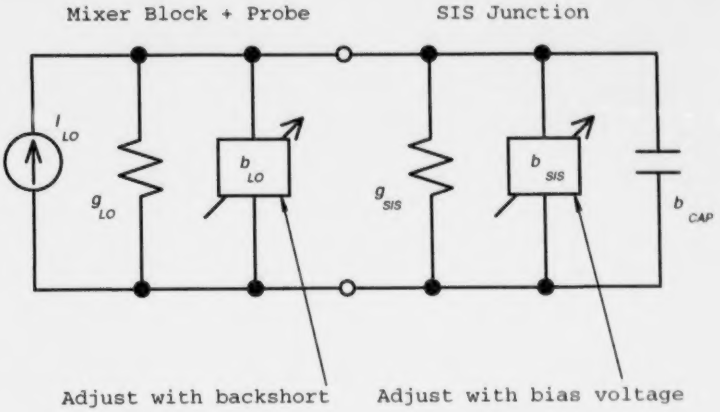

Figure 2.6: A reduced equivalent circuit representation of the bias-tuned mixer.

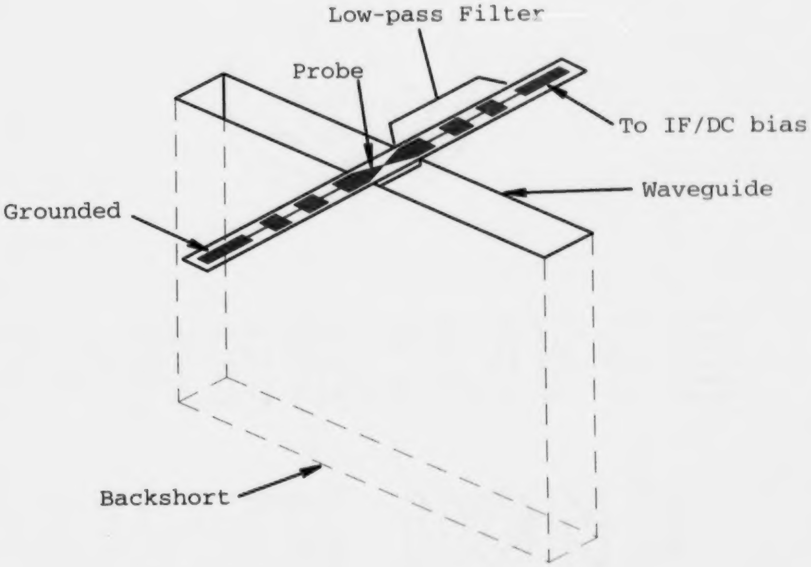

Figure 2.7: A perspective view of the waveguide probe suspended across the reduced-height waveguide. The lower section of waveguide, shown with dashed lines, is terminated with a backshort. The upper section of waveguide that leads to the horn antenna is not shown.

2.2.1 Model measurements

Since direct measurements of structures above ~40 GHz are difficult due to the lack of instrumentation and the small size of the structures, a scale model of the probe and backshort was constructed. The components were scaled by a factor of 20 resulting in a centre frequency of 5.5 GHz. To access the centre of the probe, an electric wall was placed along the guide through the centre of the probe, reducing the waveguide height by two. A small RF connector penetrated this wall and was joined to the tip of the probe. Impedances measured in this way were reduced by a factor of two from the value for the complete probe. The probe was fabricated by depositing and patterning aluminum on a slab of fused quartz. The waveguide was terminated with a sliding load: moving the load traced out a circle on the Smith chart, the centre of which would be the impedance for a non-reflecting load. The probe impedances were measured with an HP-8510 vector network analyzer.

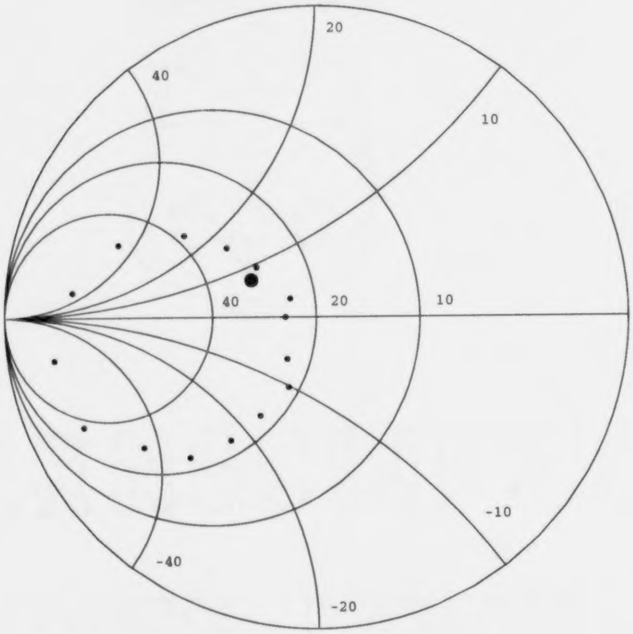

Figure 2.8: Measured probe admittances from the scale model. The Smith chart is normalized to 20 mS and the admittances are for the full-width probe. The large dot represents the minimum backshort distance, and the other dots, going in a clockwise direction, represent other backshort distances. The incremental changes in the backshort setting are constant.

The measured impedances are shown in Figure 2.8. Note how they approximately trace out a constant conductance circle on the Smith chart. The behavior of the 5.5 GHz scale model thus gave confidence that the 110 GHz backshort would provide shunt admittances lying along a similar constant-conductance circle.

2.2.2 Electromagnetic simulations

To understand the probe impedance better, a computer model was used. This allowed a variety of parameters to be changed without having to modify and remeasure the scale model. This model was based on a commercial electromagnetic simulator called *em* [12].

The simulator uses a numerical technique called the Method of Moments [13]. In this technique, a continuous integral formulation of the coupling between different parts of the structure is discretized, and surface currents are found that satisfy the boundary conditions, namely that the tangential electric fields on conductors equal zero. A major advantage of this technique is that only the conducting surfaces need to be gridded. Other numerical methods such as Finite Differences, Finite Elements, or Transmission Line Methods grid the entire volume under study, resulting in very large sparse matrices. The Method of Moments uses smaller matrices that are usually completely filled.

In this implementation, the structure is placed within a conducting box, and the coupling between conducting regions is determined through waveguide modes. Although the sidewalls have zero surface impedance, the top and bottom walls can have a finite resistance. Structures are built with slabs of dielectric that are parallel to the top and bottom, and run continuously from one wall to the other. Metallization is placed onto these slabs and connected with measurement ports on the sidewalls. The program then calculates the scattering parameters for these ports, much like a network analyzer.

Although this simulator is sold as a tool for analyzing microstrip circuits found in microwave devices such as monolithic microwave integrated circuits (MMIC's), the software was originally written to solve waveguide problems, and thus was appropriate for this application. The easiest way to construct a waveguide circuit was to use the sidewalls of the box as the sidewalls, top walls, and bottom walls of a waveguide. The bottom end of the box was used as the backshort, and the top was used as the load. By setting the resistance per square of the top end to the wave impedance of the guide, the load was made non-reflecting for single mode operation. A number of computational experiments were done to verify this model. The velocity of propagation in the waveguide was calculated and was found to agree with theory. Next, the low frequency cutoff of the waveguide was calculated and found to be the same as predicted by theory. Another test was to simulate a published waveguide probe design [14]. Again, the simulator produced very similar results. A final check was to look at the phase of the reflection coefficient of an E plane septum across a waveguide. The results of simulations were within 2.5° of the phases calculated in [15]. This series of experiments helped develop confidence in the program and uncover several subtle problems with it.

Figure 2.9 shows the configuration of the computer model. For clarity, this drawing is not to scale. Like the scale model, only one side of the probe was simulated. This was done to minimize computation time. The distance from the bottom of the box to the quartz layer was varied from run to run to simulate adjustment of the backshort. The dielectric constant of the slab was set to that of quartz ($\varepsilon_r = 3.8$). Two ports were connected to the metallization, one at the feed point (port 1), the other on the edge that connects to the low-pass filter (port 2). Two-port s-parameters were obtained so that the effect of the low-pass filter reflection phase could be studied later using cascade relationships for s-parameters.

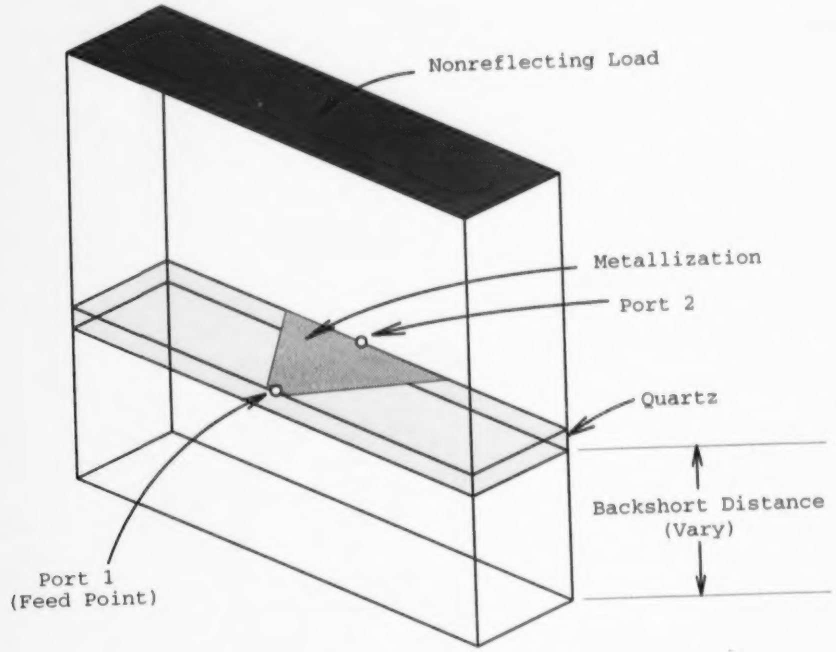

Figure 2.9: Diagram of waveguide probe model used in the electromagnetic simulator.

Unfortunately there were several approximations in this model. One was due to a limitation of this program that requires dielectrics to extend across the entire width and length of the conducting box. The seriousness of this restriction is not great, however, because measurements with the scale model showed the effect of dielectric far from the metallization to be small. A second approximation was that while the real waveguide walls had holes for the quartz wafer to pass through, the computer model must have solid walls. A third approximation was the assumption that the backshort was lossless. Although the surface resistance of the bottom of the simulation box could have been made non-zero to account for losses, that was not done because the losses were unknown and difficult to measure. Later, during the receiver experiments, the local oscillator was nearly nulled out at certain backshort settings, confirming that losses were low.

The results obtained for the probe simulations, shown in Figure 2.10, were qualitatively similar to those of Räisänen *et al.* [16]. As the backshort was moved through $\lambda/2$, the feed point admittance moved about a circle on the Smith chart. As the phase of the low-pass filter admittance was varied, that locus of points moved around the outer edge of the Smith chart. This movement was such that a point on the locus was always on the edge of the Smith chart with the radius of the locus variable. Thus, by selecting the proper low-pass filter phase, the locus was positioned so that it followed a constant conductance circle. This was the result needed for the experimental mixer.

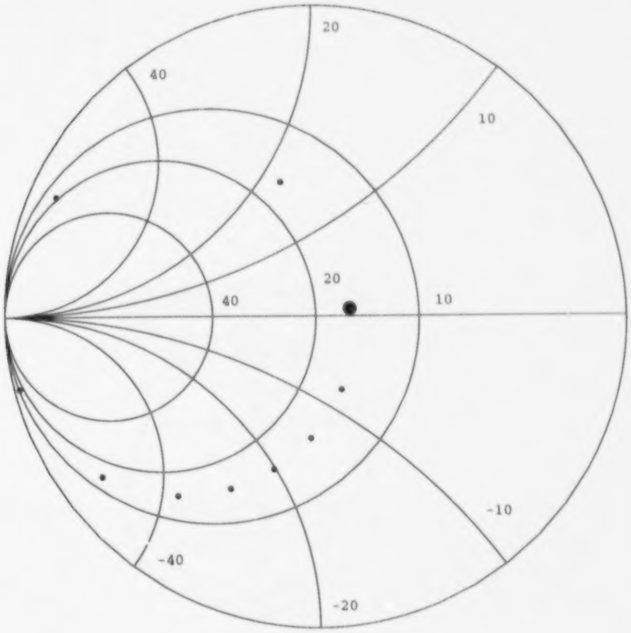

Figure 2.10: Plot of simulated feed point admittances for the waveguide probe. The Smith chart is normalized to 20 mS and the admittances are for the full-width probe. The large dot represents the minimum backshort distance and the dots moving away in a clockwise direction indicate larger backshort distances. The backshort variation was in constant steps.

There are some discrepancies between the simulated and measured admittances. First, the simulated impedance circle touches the outer edge of the Smith chart while the scale model circle does not. This could be due to resistance in the scale model, such as in the silver paint connection which was used between the probe and the connector. These results could be explained by a resistance of 2 Ω, a value which is not unreasonable. The second discrepancy was with the maximum real impedance measured: the simulated result was greater than the measured value. This could be explained by a loss in the backshort which would reduce the radius of the measured impedance circle. This explanation is weak since a spiral is not present in the data. The final discrepancy was the spacing of points on the Smith chart. In both cases the backshort was adjusted by constant steps, but the spacing of the impedance points around the circle was nearly constant for the measured data and variable for the simulated data. At present there is no explanation for this discrepancy.

Since it was more physical, the scale model results were trusted more than the simulation, and those results were used for the design. Thus for subsequent steps in the design, a simple model (for the full probe) of a 25 mS conductance in parallel with a variable susceptance was used. However, computer simulations were sometimes used because they were at least qualitatively correct, they were much easier to work with than a scale model, and access to the network analyzer became very limited. The electromagnetic simulator was the primary design tool for planar transmission lines because it could take into account the surface impedance of superconducting metallization whereas that would be difficult with a scale model. The simulator was trusted for microstrip circuits because fewer approximations were required than with the waveguide probe simulations to convert the physical structure to a computer model.

2.2.3 Low-pass filter design

The final step in the probe design was the specification of the low-pass filter. This filter performed two functions. First, it prevented RF energy from leaking down the lines along which the IF signal and the DC bias current flow. The second function was to terminate the outer edges of the probe so that the terminal admittance of the probe was moved to a desired value. This design assumed a quartz wafer thickness of 70 μm.

The first requirement was achieved by an alternating series of low and high impedance transmission lines, each a quarter wavelength long. This can be seen in Figure 2.7. There were three complications in this design. First, the microstrip lines forming the filter were inside a conducting tube of rectangular cross-section rather than over a flat ground plane. So although published design equations were used for a starting point of the design, the electromagnetic simulator was used to optimize the design. The second problem was the length extension of the wide low impedance line by fringing fields. Again, the electromagnetic simulator was used to reduce the line lengths until the proper phase shift was obtained. The final problem was the possibility of airgaps between the bottom of the substrate and the bottom of the mounting channel. Again this was a problem easily understood using the simulator program. This effect was found to be significant because a 10 μm airgap changed the filter phase by 16°. Therefore, when the wafer was mounted, liquid acrylic was wicked between the wafer and the mixer block bringing the pieces into very close contact.

The second purpose of the low-pass filter was to provide a reflection coefficient of $1\,\underline{/-109^\circ}$ so that a constant-conductance variation on the Smith chart would be obtained as the backshort was adjusted (see section 2.2.2). This was obtained by adjusting the length of the first low impedance section adjacent to the probe.

The widths of the two types of lines were chosen so that they could each be easily fabricated. The width of the narrow, high impedance section was 10 μm because that was a narrow width that could be patterned by a variety of techniques with good reproducibility. The low impedance line was 400 μm wide. This width was chosen because it was the largest width that could be placed on a 500 μm wide quartz wafer without being damaged by the dicing saw used to cut the wafers.

2.3 RF circuit design

With the probe design complete, the matching between the probe and the SIS device was specified. Although an array of two 1×1 μm^2 junctions and resonating circuits could match directly to the waveguide probe, it was uncertain whether or not junctions that small could be made. Thus a variety of contingency designs were devised with more complicated circuits that could match to larger area SIS junctions. Fortunately the small SIS junctions worked and the simpler design was used. That design had fewer uncertainties associated with it and hence became the primary design. Since the other contingency designs were not tested they will not be discussed here.

Two simple device models were used for the designs. The probe was modeled as a 25 mS purely conductive generator (i.e. the variable shunt susceptance was set to zero). The junction was modeled as a 50 mS resistor (the quantum conductance) shunted by a 50 fF capacitor (the geometric capacitance) and a $-j$ 14 mS inductor (the quantum susceptance). Simplified further, the model was a 50 mS resistor in parallel with a $+j$ 20 mS capacitor. This model was for a 1 μm^2 junction with a current density of 4000 Amps/cm^2 at 110 GHz. These parameters were obtained using an I-V curve from an SIS device fabricated about a year before the devices used in the experiment were made. Therefore the design parameters differ from those obtained from Figures 2.2 and 2.3 since those plots were generated using an I-V curve from these experiments.

From these models a simple design was apparent: a series array of two junctions with susceptances canceled would be matched to the antenna. The design was reduced to finding a shunt network to cancel the junction susceptances since no further impedance transformations were needed. The shunt susceptance was synthesized with a length of transmission line with an RF short circuit at the far end. This circuit used the probe and the first section of the low-pass filter as a ground plane.

Two possibilities were considered for the transmission line. One was to use a microstrip line. Microstrip with a 6 μm wide niobium line over 300 nm of SiO insulator and a niobium ground plane has a characteristic impedance of 9.3 Ω. However, to synthesize the required impedance of $+j$ 50 Ω with this line requires a phase length of 80°. The problem with this realization was that it would be extremely sensitive to errors and variations of the dielectric thickness or permittivity. The situation would be made worse because the microstrip parameters are also sensitive to the superconducting properties of the niobium film. This can be understood from Equation A.35 in the appendix: when the dielectric thickness is made similar to or smaller than the magnetic penetration depth, the inductance is modified by the superconductivity of the conductors. Thus it was clear that there would be significant uncertainties with this design.

An alternative to microstrip was co-planar waveguide (CPW). As shown in Figure 2.11 a), CPW consists of a narrow signal conductor on a dielectric with ground planes on either side. One advantage of CPW for this application was its high characteristic impedance of 102 Ω. Thus a phase length of only 26° was required. Another advantage of the CPW was that due to the geometry, the line properties were largely insensitive to parameters such as the SiO thickness and dielectric constant, and the surface impedance of the niobium. These advantages made the CPW design the primary one.

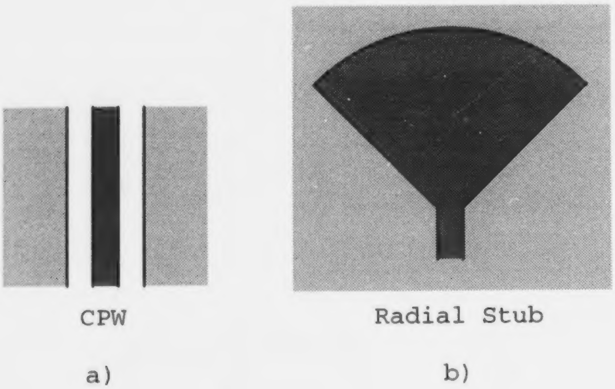

Figure 2.11: Examples of transmission line structures used in the receiver design. The light shading represents the ground, and the dark shading represents the signal line. In a), the ground plane is removed around the signal line which is directly on the substrate. In b), the ground plane is continuous and is separated from the signal line with a thin dielectric layer.

The RF short was realized with a radial stub [17]. This stub provided a broadband short near 110 GHz and an open circuit for the IF and DC bias circuits. It is depicted in Figure 2.11 b). Although it is a microstrip structure, its wide-band frequency response makes it less sensitive to errors and variations in material parameters. An optimum stub radius of 135 μm was found through iteration using the electromagnetic simulator. Those calculations assumed a magnetic penetration depth (λ) of 85 nm [18], a normal state conductivity of $10^6/(\Omega{\cdot}\mathrm{m})$, and a relative dielectric constant of 5.5 [19].

Figure 2.12 shows a photomicrograph of a mixer circuit similar to the one used. The centre conductor of the CPW line runs from the SIS junction, over a hole in the probe metal to form the CPW line, to the radial stub. The radial stub was split into two parts so that it would fit into the available space. The mixer chip that was tested had a series array of two junctions. It differed from this photograph by having a junction, CPW line, and radial stub on each probe which were joined with a very short section of the centre conductor. The operation of this tuner was verified using the electromagnetic simulator.

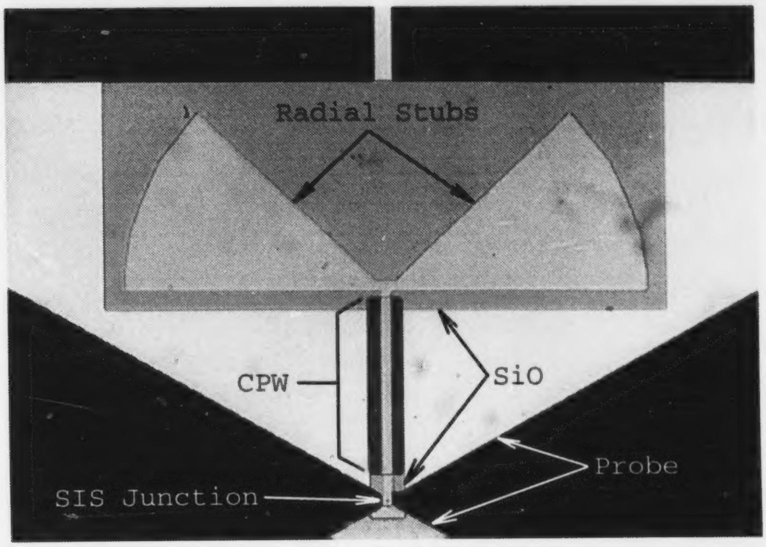

Figure 2.12: Photograph of an SIS mixer device similar to the one used. The actual device had two SIS junctions in series, thus it had two CPW tuners. Note that some of the differences in gray are due to SiO thickness.

2.4 Precision mixer block design

For these experiments a mixer block was needed that was simple to build, had good antenna properties, had an adjustable backshort, and had a minimum of waveguide discontinuities. The last requirement was particularly important for this experiment since reflections from, or leakage through, discontinuities would change the waveguide probe admittance. That requirement made the modified Schottky mixer block that had been used for preliminary work unsuitable because it had three transverse cuts through the waveguide. Therefore a new mixer block was designed that had the waveguide split longitudinally. This configuration also made it convenient to machine a diagonal horn in the block.

2.4.1 Split waveguide with alignment keys

A common construction technique for waveguides at millimetre and shorter wavelengths has the waveguide split longitudinally, through the top and bottom walls [20]. Not only is this structure easy to fabricate with a slitting saw on a milling machine, it is also low-loss. This can be understood by considering the fundamental mode in the waveguide: the E field lines are normal to the top and bottom walls which are equipotential surfaces and thus the cut will not impede the flow of surface currents.

A major objective here was to minimize misalignment between pieces. Typically alignment is done with circular pins in holes. Unfortunately, since a good machinist can locate holes to within 0.001 of an inch (0.025 mm), two pieces can only be aligned to within

.002 of an inch (0.05 mm). This is a significant error compared with the waveguide height of .225 mm. However, by forming the waveguide as a slot, additional slots can be cut in both halves of the block for alignment with metal keys. This technique eliminates the alignment error completely.

Figure 2.13 shows the machining technique. The two halves of the mixer block were originally joined together, back to back. In the figure the dashed lines represent the location of the diagonal horn. The waveguide slot was cut at the same time as the two alignment slots. Note that although these slots did not need to be located precisely, they had to be parallel to the waveguide slot so that any offset error was the same for both halves. Once these grooves were cut, the block was cut into two halves. The next step was to cut transverse slots for mounting the SIS wafer, shown in Figure 2.14. For this step the two pieces were placed side-by-side, and as before, an alignment groove was cut along with the mounting groove for precise alignment. A hole was bored part way to the centre of the block to provide access for the IF/bias connector. The final step was the milling of the V grooves for the horn. The two finished halves were assembled, as shown in Figure 2.15, with tight fitting metal blocks in the alignment grooves.

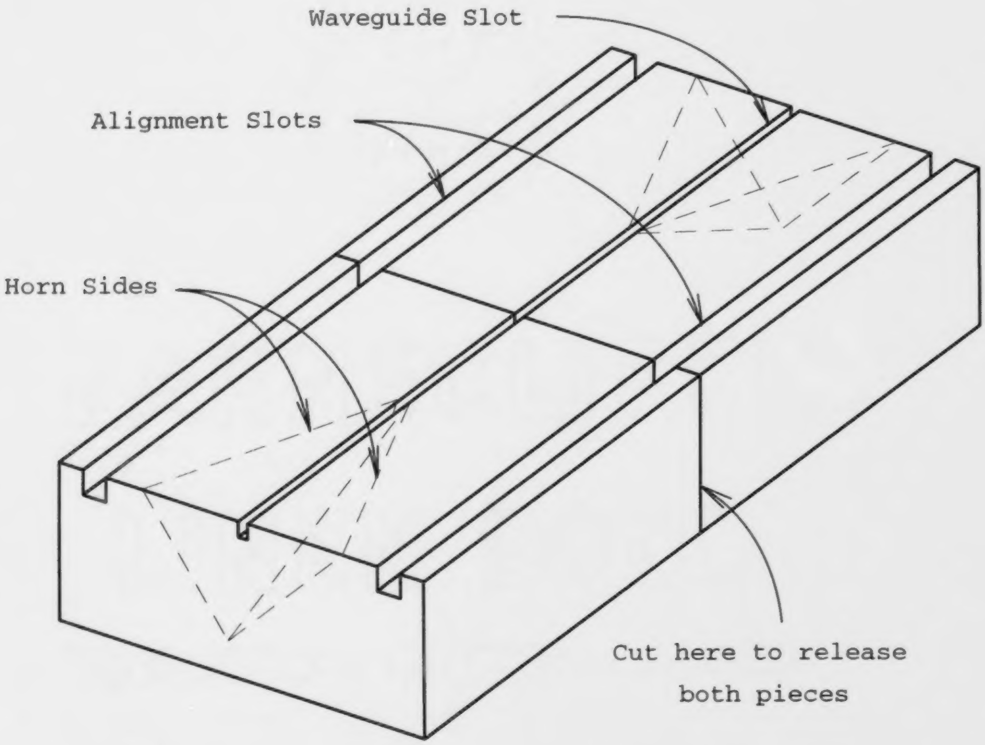

Figure 2.13: Diagram showing how the waveguide slot and the alignment slots were cut into the mixer block. At this point, the two halves of the mixer were in one piece. The dashed lines show where the horn will be milled out.

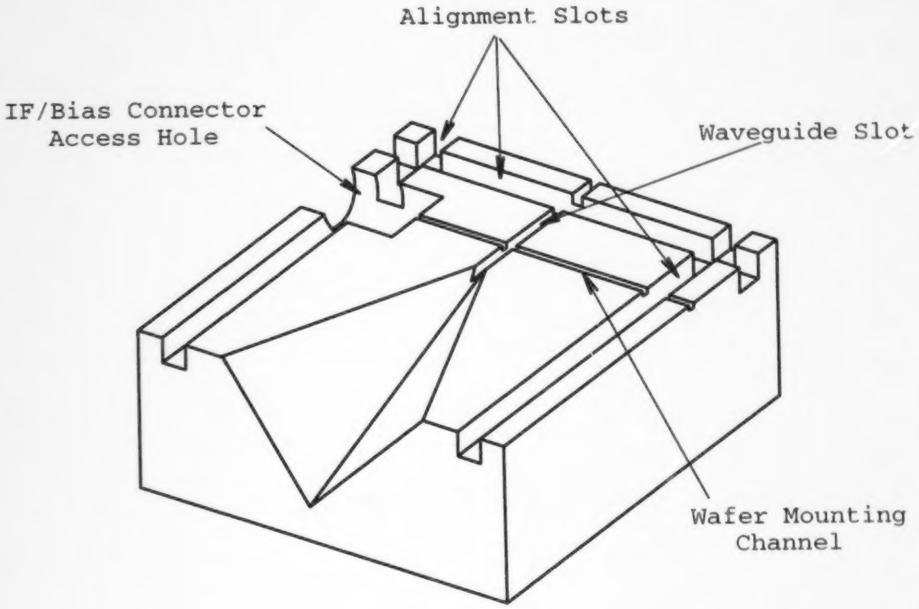

Figure 2.14: Drawing of mixer block showing the transverse wafer mounting channel and an additional alignment slot. For clarity, this figure is not to scale and has been simplified.

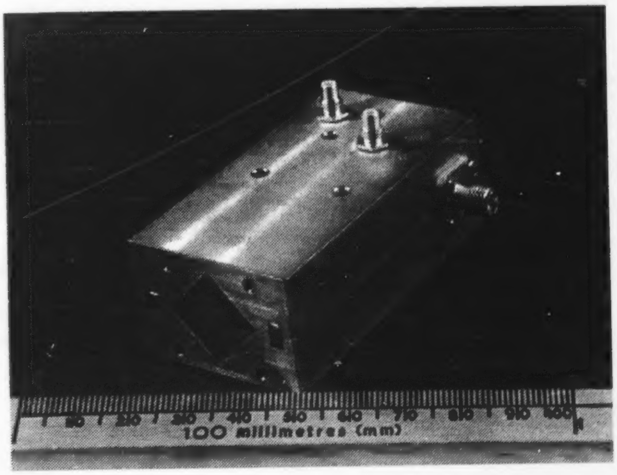

Figure 2.15: Photograph of the assembled mixer block. Metal keys placed in the alignment grooves prevent the horizontal motion of one piece with respect to the other. The connector on the side is for the IF/DC bias and the connectors on the top are to be used for biasing the integrated Josephson effect suppression electromagnet.

2.4.2 Diagonal horn antenna

A diagonal horn was chosen for this mixer for a variety of reasons. One alternative was the corrugated horn which has a nearly ideal radiation pattern, but is very difficult to make. Another alternative was the pyramidal horn which is simple to make, but has an inferior radiation pattern. Thus the diagonal horn antenna (see Chapter 4) was a good compromise between complexity and performance. As shown by Figure 4.10, the responses in the E, H, and D planes are very similar down to the -10 dB level, and the E and H planes remain similar down to the -20 dB level. These radiation patterns are nearly Gaussian making them well matched to the field distributions found in millimetre-wave receiver systems. This type of horn was also easy to make: the metal block (shown in Figures 2.13 and 2.15) was tilted to produce the taper, and the milling head with end mill was tilted at 45° to produce the V groove. This construction technique was also compatible with the split block design for the waveguide. This antenna is discussed in more depth in section 4.2 of chapter 4.

There are several disadvantages to this antenna design. One is the presence of sidelobes in the diagonal or D plane response, shown in Figure 4.10. With the optical arrangement in the cryostat used, the edge of the window was at the -17 dB level so this was not a concern. Another potential problem was the high on-axis cross-polarization response. Figure 4.11 shows an example of this where the cross-polarized response is only 13 dB below the co-polarized response. For some applications, such as polarimetry, this would be a concern, but for this work the cross-polarization was adequate.

2.4.3 Non-contacting backshort

The other critical component making up the mixer block is the adjustable backshort. A noncontacting design was used to avoid wear caused by contacting designs which can lead to intermittent behavior. A rectangular backshort was used instead of a circular backshort [21] because of the large width-to-height ratio of the waveguide (nearly 10:1). This design is shown in Figure 2.16. The signal is prevented from propagating down the sides of the backshort by the alternating low-impedance (narrow gap) and high-impedance (wide gap) sections, each one quarter-wavelength long. The lengths of the sections were adjusted to account for fringing fields using equations in [22]. The backshort was coated with a layer of thermally evaporated SiO on each side to provide a thin insulating layer [23]. The backshort was inserted into the waveguide behind the SIS wafer and its position was controlled with a 40 turns per inch screw connected to a turns counting dial. The operation of the backshort was verified with the backshort in the 5.5 GHz scale model.

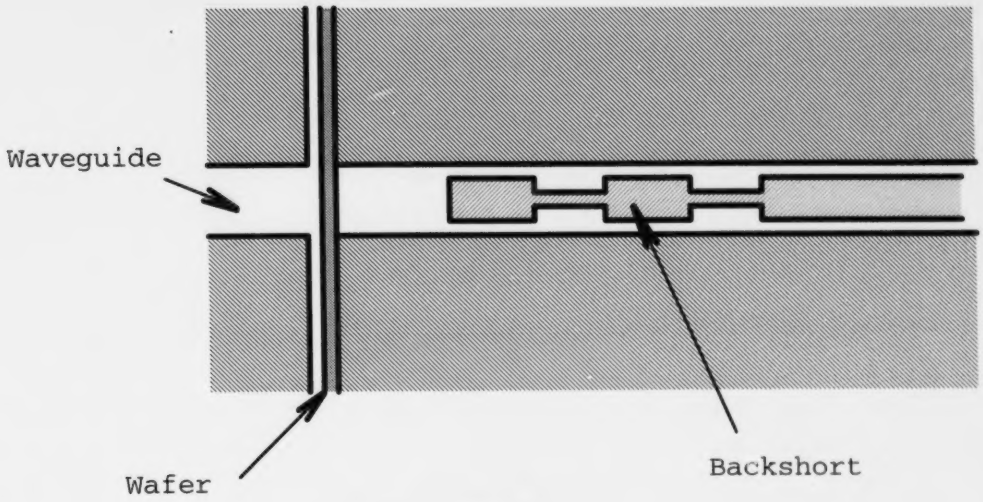

Figure 2.16: Cross-section through the backshort, waveguide, and wafer supporting the SIS device.

2.5 SIS fabrication

Although the focus of this work was in the application of superconducting devices, for completeness the fabrication process will be outlined. The process was based on the original niobium process developed by Gurvitch *et al.* [24] and was very similar to the Jet Propulsion Laboratory process [25]. The devices were fabricated by Dr. Kevin Kornelsen at the Alberta Microelectronic Centre (AMC), with substrates prepared by Barry Arnold in the Electrical Engineering Department of the University of Alberta.

2.5.1 Summary of fabrication process

Fused quartz was used as the substrate material. Quartz was chosen over silicon because its lower dielectric constant (3.8 vs. 11.7 [26]) was better suited for applications where the antenna structure must couple to free-space or a vacuum-filled waveguide. A wafer thickness of 70 μm was used because it was much less than a wavelength, but still not too fragile to handle. To minimize breakage during processing, the wafer was bonded to another quartz wafer that was 1 mm thick. An acetone soluble adhesive (Crystalbond 509 adhesive [27]) was used so that the mixer devices could be easily removed for use.

The clean substrates were then covered with the superconductor-insulator-superconductor trilayer. Although this multilayer is universally called a "trilayer," it is really a stack of five materials: niobium, aluminum, aluminum oxide, niobium, and gold (going from substrate up). Figure 2.17 shows this structure.

The depositions took place in a Perkin-Elmer 4400 Delta sputter system. This was a load-locked system with a base pressure of ~10^{-7} torr. The main chamber contained both a niobium and an aluminum source. A small gold sputter source was mounted on the load lock door. Since the system did not contain an *in situ* film thickness measurement device, the thickness was determined by counting the revolutions of the wafer under the sputter source at a known deposition rate.

The bottom layer of niobium was deposited to a thickness of 120 nm. This thickness was chosen since it was thicker than the magnetic penetration depth for niobium, and because it was thin enough that the accumulated film roughness did not seriously degrade the junctions. A 13 nm thick aluminum layer was then deposited. Aluminum was used because it wets the surface of the niobium, permitting thin layers to be formed that are also continuous [24]. To form the insulating layer, the wafers were transferred into the load lock and exposed to pure oxygen at a pressure of 60 mtorr for 3 minutes. The depth of the aluminum oxide layer was controlled by the oxygen pressure and the length of exposure time [28]. The wafers were then transferred back into the main chamber for the final layer of niobium which was 90 nm thick. The top layer of niobium was protected from oxidation with a layer of gold 20 to 30 nm thick. This step was critical for obtaining low resistance contacts to the SIS junction.

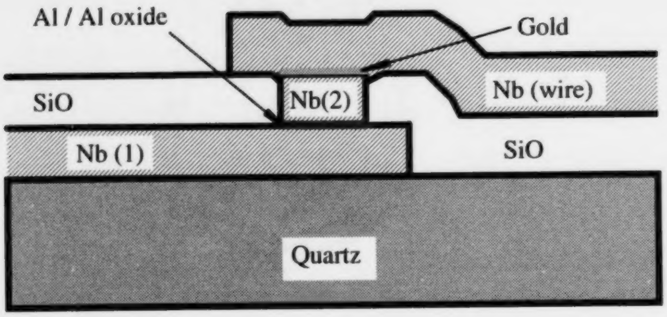

Figure 2.17: Cross-section through a niobium SIS device (not to scale).

The trilayer was then patterned using photolithography and reactive ion etching (RIE). The main advantage of etching with an RIE machine was that it produced nearly vertical cuts through the film [29]. This was particularly important for the definition of the junction, since undercut of the etch mask would reduce the area of the junction, possibly to zero.

Later on, another layer of niobium would be deposited (the wiring layer) to make contact with the top of the SIS junction. To isolate the wiring layer niobium from the base layer of niobium, a layer of SiO was thermally deposited. The vacuum system base pressure of 10^{-6} torr was maintained throughout the deposition producing a very directional flux. To minimize shadowing by topography on the wafer and to prevent thickness variations due to an uneven flux distribution, the wafers were mounted in a planetary mount. The thickness was typically 0.24 μm and was measured with a calibrated crystal thickness meter.

The SiO layer was not patterned with etching. Instead a technique called photoresist liftoff was used. In this technique photoresist was placed where the SiO was not to remain, and after the deposition, the photoresist was dissolved, removing unwanted SiO.

The final process steps placed and defined the shape of the top layer of niobium which contacts the top of the junction. Again, the niobium was deposited in the Perkin-Elmer sputter system. This layer was about 150 nm thick and was patterned by liftoff.

2.5.2 Anodization spectroscopy of trilayers

For a long time the AMC SIS production process was intermittent and produced junctions with high leakage currents. A series of experiments was initiated that isolated a problem that, when corrected, improved the reliability of the fabrication process and reduced the junction leakage current. The technique employed is called anodization spectroscopy since it provides information on the material composition of the trilayer using anodization.

It is fortunate that both niobium and aluminum can be anodized, otherwise this technique would not be possible. As a sample is anodized, the anodization front moves deeper and deeper into the material, and the rate varies according to the material. The depth of the anodization is made apparent by the voltage drop across the sample because anodization changes highly conductive metal into a resistive material. Thus, when driven by a constant current source, the voltage is proportional to the depth of the anodization front. For niobium the proportionality constant is 0.85 nm/V, and for aluminum it is 0.88 nm/V. In addition, by differentiating the voltage the rate of change is observed, identifying the material. So for a multilayer stack, the sharpness of the differentiator output step will correspond to the sharpness of the material transition.

Figure 2.18 shows the test apparatus. The sample, which had a trilayer film with an area of 2 mm^2, was immersed in an electrolyte in a vial. The vial had a diameter of ~2 cm to minimize waves set up by vibrations, and was mounted on foam rubber for the same reason. The electrolyte was a mixture of 156 grams of ammonium pentaborate in 1120 ml of ethylene glycol and 760 ml of water [30]. The negative electrode was pure aluminum wire. The constant current source was a Hewlett-Packard 6181B DC Current Source with a maximum output voltage of 100 V. This allowed films to be scanned to a depth of about 110 nm. The op-amp was protected from high voltage transients by parallel opposing small signal diodes. The two outputs were connected to the inputs of a Hewlett-Packard 7035B X-Y Recorder so that the rate of change of the voltage was plotted against the voltage or equivalently, the depth.

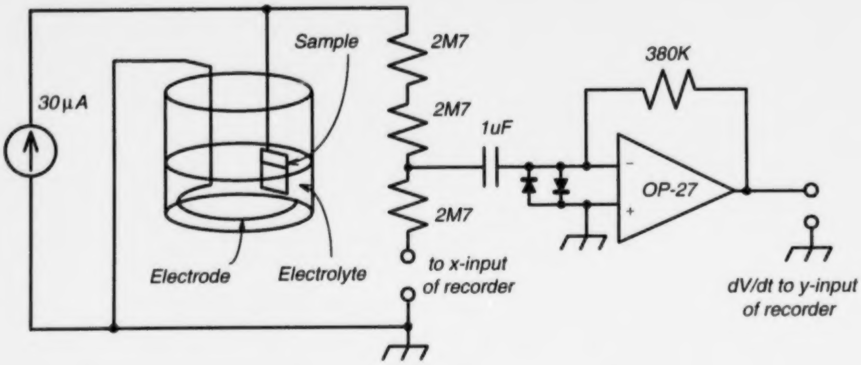

Figure 2.18: Schematic of test apparatus for anodization spectroscopy of niobium-aluminum-niobium trilayers.

The selection of component values was based upon [30, 31]. A typical anodization current used in these references was 0.5 mA/cm^2. For a sample area of 2 mm^2 this corresponds to 10 μA. In practice it was found that a higher current of 30 μA produced equivalent results and took 1/3 the time. The transfer characteristic for the differentiator is $V_{out} = -RC(dV_{in}/dt)$. Changes in cell potential of 0.05 V/s and 0.08 V/s were observed in [33], so with $R = 380$ kΩ and $C = 1$ μF, outputs of 19 and 30 mV would be expected. These are both easily measured values, well above the input noise of the X-Y recorder. The capacitor chosen was the largest high voltage monolithic available. This capacitor could not be too large otherwise it would sink a significant fraction of the current going into the cell. In this case the current into the capacitor was 0.05 μA, much less than the total current of 30 μA supplied. Three 2.7 MΩ resistors in series with the X-Y recorder x-input prevent the input voltage from being exceeded.

Good quality results were obtained with this configuration. A film could be scanned to 60V in about 4 minutes. Two types of noise artifacts were seen. One kind was occasional spiky transients, and the other was lower in amplitude, but much more frequent. The sources of this interference were not determined, but could have been the release of charged bubbles produced by the anodization process. Much of the time the spiky transients were just annoyances, but if a feature was obscured, another sample was scanned. Other interference, such as 60 Hz mains pickup, was not observed.

Two scans are shown in Figures 2.19 and 2.20. These scans are read from left to right showing the film profile from to top to bottom. There is a sudden turn-on transient at zero volts, which is not shown except near 5 volts. Large transients are visible in each of the plots; in Figure 2.19 near 28 volts and in Figure 2.20 near 36 volts. Neither of these obscured the transition between the layers so the plots were judged to be satisfactory. A vertical scale is not shown since that information is not used; it is the shape of the curves that conveys information.

The only difference between the samples that produced these curves was that the first had a base layer of 30 nm, and the second had a base layer of 120 nm. The top layers were 30 nm and the aluminum was 10 nm thick for both. The key result from this experiment was that the transitions from Nb to Al, and from Al to Nb were much sharper with the thin base layer than with the thick base layer. The conclusion from these experiments was that the niobium films were inherently rough and, as the films were made thicker, the roughness accumulated and became greater. Thus the interfaces between the materials were less sharply defined for the thicker films.

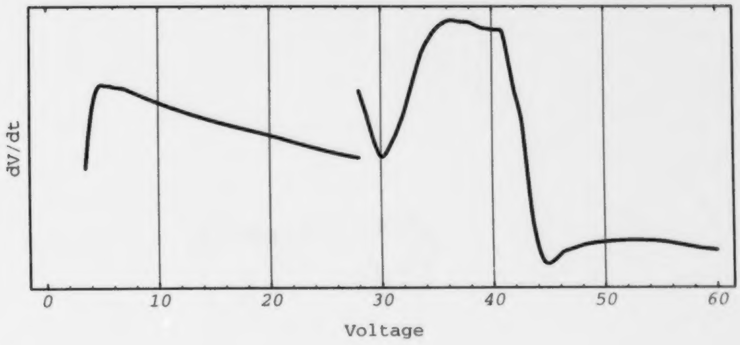

Figure 2.19: Anodization spectroscopy curve for a trilayer with a thin base layer.

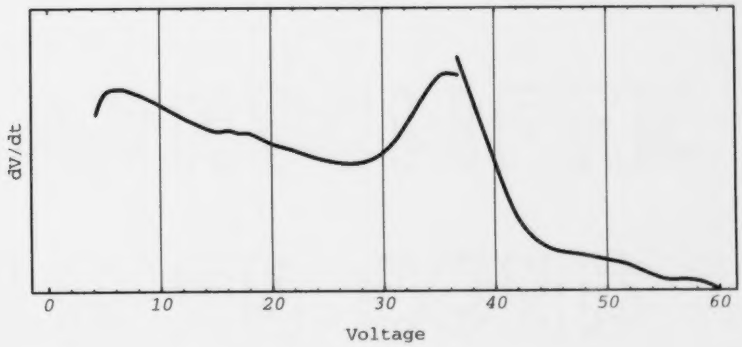

Figure 2.20: Anodization spectroscopy curve for a trilayer with a thick base layer.

There were four ways to deal with this problem. The first was to make the base Nb thinner. This was not practical since the current-carrying capacity of the film would be reduced and the RF properties would be modified if the film was thinner than a magnetic penetration depth (85 nm). The second was to make the aluminum thicker. This turned out to be the only solution that worked. The drawback of this solution is that the proximity effect at the gap voltage becomes larger [32]. The third solution was to vary the Nb deposition conditions to try to form a smoother film. For example, films sputtered with a lower argon pressure tend to be smoother. Unfortunately, films that were both smoother and had low stress could not be made in this vacuum system. The last approach was to make a thicker film with two films sandwiching a planarizing layer. Imamura and Hasuo [33] show with transmission electron microscopy that although a layer of Nb may be rough, an oxidized layer of aluminum stops the propagation of grain structure into the overlying Nb layer, thus planarizing the lower Nb. They found that the oxide layer was crucial for stopping the grain structure. Unfortunately, experiments with a composite base layer did not produce smoother films as determined by anodization spectroscopy.

2.5.3 Remaining problems with SIS devices

The anodization spectroscopy experiments and the resulting modifications improved the SIS fabrication process. Not only was there a much higher confidence that the junctions from a given batch would work, junction quality was also improved by the reduction of leakage currents. However, there were other problems which were not resolved. Figure 2.1 shows that the gap voltage is ~2.55 mV, which is much less than the expected value of 2.7 to 3.0 mV. A reduced gap voltage would be expected for a reduced transition temperature, but the Nb films used had transition temperatures of ~9.0K, very near the expected value of 9.2K. Another problem was the width of the transition at the gap voltage which was 0.35 mV or greater. This was significant because it is a large fraction of a photon step width (0.455 mV). This could have been due to a variation in electrode quality across the junction. If that was the case, then the observed I-V curve would be the sum of a large number of sub-junction I-V curves with different gap voltages, producing a smeared transition. Another disturbing feature was the lack of a clear proximity effect above the gap voltage. This flat structure in the I-V curve is a result of the normal metal (aluminum) between the superconductor and the insulator, and should have been prominent because of the thick Al layer. Again, what was observed may be due to a smearing effect from variations across the junction.

It is important to contrast these results with earlier results, and with the results of other workers. The first Nb SIS devices made at the AMC had a higher gap voltage, near 2.7 mV, and clearly showed the proximity effect. These features could not be restored by following the earlier process recipe. Perhaps this was due to contamination of the deposition equipment by different materials used in other projects. The I-V curves appearing in the literature are quite variable in quality. Some workers have made high performance receivers with SIS junctions worse than shown here. (See, for example, Walker *et al.* [34].) However, it appears that others have not had the same problems with film roughness experienced by our group. For example, most others make junctions using thinner Al layers than used here. There is also one case of a vertical stack of junctions being fabricated without significant degradation of the upper junction [35].

2.6 Measurements

The measurements to test the bias-tuning concept were of three types. The first was an operational test of the concept by finding the minimum noise temperature and corresponding bias voltage as a function of backshort setting. The second was to find the peak detected LO power and the corresponding bias voltage as a function of backshort tuning. This test examined LO coupling only and used the SIS device as a total power detector rather than a mixer. The third measurement was to record the pumped I-V curve as a function of backshort tuning. This last test was to provide the information needed to extract the junction embedding admittance so that the constant conductance operation of the mixer could be confirmed.

The experiments took place in July and September of 1994. The mixer wafer mounted was a series array of two 1×1 μm^2 junctions with CPW tuners shunted across each junction, similar to the one shown in Figure 2.12. The I-V curves obtained on July 21 and July 28, 1994 had the LO power adjusted to a moderate level for each trace. The last run on September 15, 1994 had the power fixed and at a higher level.

2.6.1 Test setup

A model HD-3(8) cryostat was used for the experiments [36]. The mixer, IF amplifier, and infrared filters were mounted on a cold plate attached to the liquid helium reservoir. A radiation shield was placed between the helium reservoir and the vacuum jacket to reduce the rate at which the helium boiled off. This shield was cooled to 77K with liquid nitrogen. Cabling from the outside of the cryostat was thermally anchored to the nitrogen shield to further minimize the heat load on the liquid helium.

The millimetre-wave signal entered the cryostat through a 32 mm diameter vacuum window made of 2 mil (50 μm) thick mylar film. To reduce the thermal load on the cryostat, and to prevent a bolometric response in the SIS mixer, a series of infrared filters was employed. A crystalline quartz filter was placed in the hole in the 77K shield, and a Fluorogold filter was attached to the front of the mixer horn. Ibruegger [37] has shown that this configuration minimizes thermal loading of a 4K blackbody.

A free-running Gunn oscillator provided a local oscillator signal between 104 and 117 GHz with power levels of about 10 mW. The output of the oscillator was fed through a waveguide variable attenuator to adjust the power level. This was followed by a directional coupler that permitted the power level to be measured with a Schottky diode detector. A pyramidal horn was used to launch the free-space wave.

Two additional components were used to couple the LO to the receiver. The first was an elliptical mirror which focused the LO signal onto the mixer horn. The other component was a mylar beamsplitter that passed about 99.5% of the signal power and coupled in about 0.5% of the LO power.

The output of the mixer at 1.5 GHz was connected to the IF amplifier via an isolator. The important property of the isolator was that it provided a 50Ω match to both of its ports. This helped prevent oscillations in the input stage of the IF amplifier due to the dynamic output impedance of the SIS mixer. The IF amplifier was a standard design [38] using GaAsFETs and had a noise temperature of about 10K and a gain of 40 dB at 1.5 GHz. The output power from the IF amplifier was measured with a Hewlett-Packard 8970A noise figure meter outside the cryostat.

From the IF power, the noise added by the receiver, or the noise temperature, was calculated. The IF power was measured with two different input powers: a black body at room temperature (about 300K) and a black body at 77K. The ratio of the two output powers is called the Y factor. The equation defining the Y-factor is

$$Y = \frac{T_{rx} + T_{hot}}{T_{rx} + T_{cold}}. \tag{2.5}$$

This can be inverted to produce an equation for calculating the receiver equivalent input noise temperature from measurements:

$$T_{rx} = \frac{T_{hot} - Y\,T_{cold}}{Y - 1}. \tag{2.6}$$

Next, by using the Friis equation the receiver noise was separated into mixer and IF amplifier components:

$$T_{rx} = T_{mix} + T_{IF}/G_{mix}. \tag{2.7}$$

A novel way of obtaining the mixer gain and noise temperature was to calibrate the IF noise at different frequencies (1.0 to 1.5 GHz) and to measure the receiver noise at these different IF frequencies. T_{mix} and G_{mix} can be solved for using Equation (2.7).

2.6.2 Noise temperatures

Tables 2.1 and 2.2 present the measured receiver noise temperatures and are an operational test of the bias-tuned mixer technique. These temperatures include the contributions from the cryostat window and the IF amplifier as well as the mixer. The bias voltages measured have been reduced by a factor of two to the single-junction equivalent voltage. The backshort position is given as both the micrometer reading in turns, and as a distance (in guide wavelengths) between the SIS device and the end of the backshort. Similar measurements were taken at 105 and 115 GHz, but are not presented here because the 110 GHz results were sufficient. For reference, the photon step size is 0.455 mV, the guide wavelength is 3.23 mm, and there were 7.11 turns of the backshort drive per wavelength.

Table 2.1: July 21, 1994 Noise measurements at 110 GHz		
Backshort	Bias (mV)	T_{rx} (K)
9.5 turns, .17λ	2.35	66
9.0 turns, .24λ	2.35	86
8.5 turns, .31λ	2.36	100
8.0 turns, .38λ	2.35	187
7.5 turns, .45λ	2.21	523
7.0 turns, .53λ	2.29	74
6.5 turns, .60λ	2.32	54
6.0 turns, .67λ	2.35	60
5.5 turns, .74λ	2.35	79

Table 2.2: July 28, 1994 Noise measurements at 110 GHz		
Backshort	Bias (mV)	T_{rx} (K)
7.0 turns, .53λ	2.35	71
6.5 turns, .60λ	2.34	50
6.0 turns, .67λ	2.37	57
5.5 turns, .74λ	2.37	66
5.0 turns, .81λ	2.35	86
4.5 turns, .88λ	2.35	195
4.0 turns, .95λ	2.33	318
3.5 turns, 1.02λ	2.35	77

2.6.3 Pumped I-V curves

The pumped I-V curves were recorded for two reasons. The first was to extract the total detected power by subtracting the dark current (the unpumped I-V curve). The second was to obtain the probe source impedance by using the voltage match method (section 2.7.2). Two sets of data were obtained. The first, recorded on July 21 and 28, 1994, were made with the LO level such that the normalized RF voltage across the SIS junction was close to 1. The backshort was moved in coarse steps of 0.5 turn over a wide range. The second set of measurements, made on September 15, 1994, differed by having a higher LO level (close to 2) and a finer variation in backshort tuning (0.1 turn) in the range of most interest. Figures 2.21 and 2.22 show representative I-V curves at 110 GHz with the higher LO level. Data at the other frequencies is similar and the curves for the lower power level have the photon step height reduced.

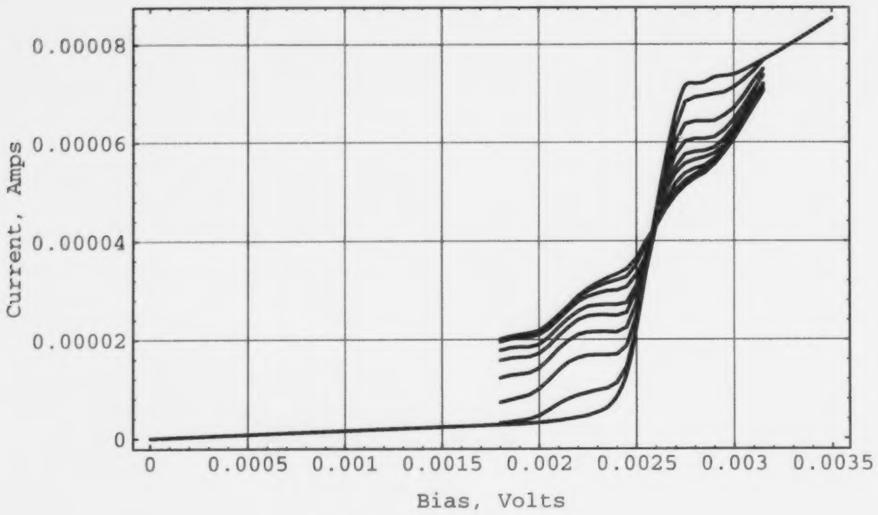

Figure 2.21: Pumped I-V curves for various backshort positions. Beginning with the highest amplitude trace, backshort position = 6.8, 6.9, 7.0, 7.1, 7.2, 7.3, 7.4, and 7.5 turns. Data has been reduced to single junction voltages. These data were taken on September 15, 1994. The normalized LO voltage is approximately 2.

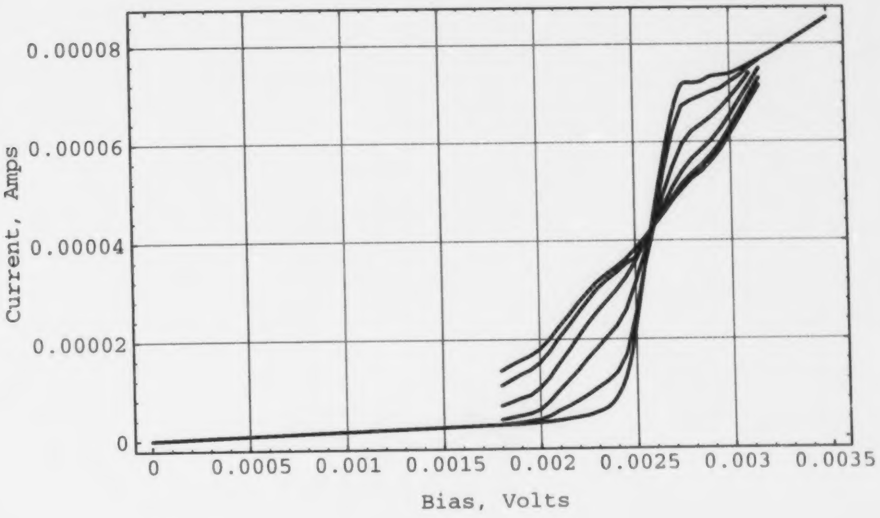

Figure 2.22: Pumped I-V curves for various backshort positions. Beginning with the highest amplitude trace, backshort position = 9.5, 9.0, 8.5, 8.0, and 7.8 turns. Data has been reduced to single junction voltages. These data were taken on September 15, 1994. The normalized LO voltage is approximately 2.

2.7 Analysis

Further analysis was required to understand these measurements. First, an error analysis of the noise temperature data will be given. Next, a method of obtaining the embedding admittance from the pumped I-V curve will be derived. Then the total power detection results will be described, followed by the embedding admittance results. Limitations to the embedding admittance results will be discussed.

2.7.1 Measurement errors

Noise temperature error was analyzed with partial derivatives of the noise temperature from Y-factor equation (Equation 2.6):

$$\Delta T_{rx} = -\left(\frac{(T_{rx} + T_{cold})^2}{T_{hot} - T_{cold}} \right) \Delta Y - \left(\frac{T_{hot} + T_{rx}}{T_{hot} - T_{cold}} \right) \Delta T_{cold} + \left(\frac{T_{cold} + T_{rx}}{T_{hot} - T_{cold}} \right) \Delta T_{hot} . \tag{2.8}$$

With receiver and load temperatures of T_{rx} = 55K, T_{hot} = 300K, T_{cold} = 80K, the equation reduces to:

$$\Delta T_{rx} = (83K)\Delta Y + (1.6)\Delta T_{cold} + (0.6)\Delta T_{hot} . \tag{2.9}$$

With typical values of ΔY = 0.05 dB = 0.012, ΔT_{hot} = 2K, ΔT_{cold} = 2K, the peak error was ~5K. This is an error of about 10% and is acceptable. This error did not affect the location of the minimum noise since that was found by looking for the peak IF output power.

Another source of error was departure from maximum power transfer from the mixer output to the IF amplifier. The equation for the coupling efficiency, the ratio of the power delivered to the available power to a matched load is:

$$\eta \equiv \frac{P_{IF}}{P_a} = \frac{4R_{mix}R_{IF}}{(R_{mix} + R_{IF})^2} \tag{2.10}$$

where R_{mix} is the SIS output resistance (the reciprocal of the slope of the photon step at the bias point), and R_{IF} is the IF input resistance (50 Ω). Typical values for R_{mix} were 77 Ω and 143 Ω, producing efficiencies of 0.96 and 0.77 respectively. The first case resulted in an insignificant error but for the second case the IF contribution to the overall noise was increased by 30% or about 3K. Again, this error did not affect the measurements.

Another possible source of error was a bolometric response. This problem originates from insufficient infrared filtering of the quasi-optical input to the cryostat. When that is the case, changing the thermal load outside the cryostat changes the SIS physical temperature. This in turn changes the IF output noise level, masking the true heterodyne response. This source of error was tested by observing the I-V curve with a room temperature input load and with a 77K load. The infrared filtering was adequate because the unpumped I-V curve did not shift, and indicated that the junction temperature was stable.

2.7.2 Voltage match method

The next analysis step was to derive the driving admittance from the pumped I-V curves. Figure 2.23 shows the equivalent circuit model for the source and the SIS junction at the LO frequency. The conductance and susceptance of the junction are known from the I-V curve, the bias voltage, and the power level by using Tucker's theory. Thus by changing the bias voltage (i.e. scanning the pumped I-V curve) the admittances on the right hand side of the circuit are varied, and from the AC voltage across the junction, the generator admittance can be deduced. An efficient method for doing this is the "Voltage Match Method" [39] and will be described below. This method is efficient because repeated calculation of junction admittances and pumped I-V curves is not required.

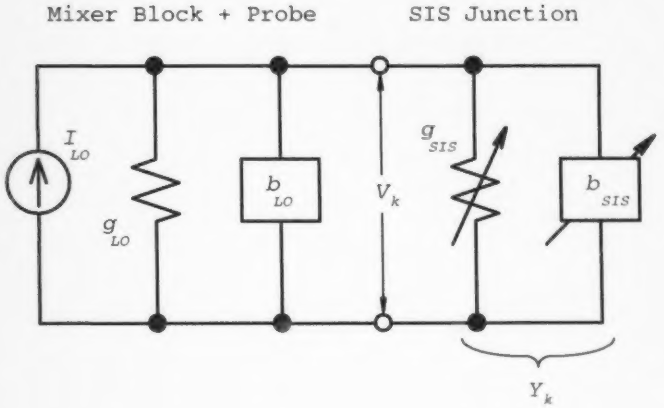

Figure 2.23: Mixer model for the voltage match method.

First, a least-squares error function is defined using primes to indicate the estimated values:

$$\varepsilon = \sum \left(V_k - \left| V_k' \right| \right)^2 = \sum V_k^{\,2} + \sum \left| V_k' \right|^2 - 2 \sum V_k \left| V_k' \right|. \tag{2.11}$$

Here the summations are taken over a number of data points recorded on the pumped I-V curve. Substituting the equation for the estimated voltage across the junction

$$V_k' = \frac{I_{LO}'}{Y_{LO}' + Y_k} \tag{2.12}$$

results in

$$\varepsilon = \sum V_k^{\,2} + \sum \left(\frac{I_{LO}'}{Y_{LO}' + Y_k} \right)^2 - 2 \sum \frac{V_k I_{LO}'}{\left| Y_{LO}' + Y_k \right|}. \tag{2.13}$$

The minimum is found by taking the partial derivative with respect to the estimated LO current and setting that to zero:

$$\frac{\partial \varepsilon}{\partial I_{LO}'} = 2 I_{LO}' \sum \frac{1}{\left| Y_{LO}' + Y_k \right|^2} - 2 \sum \frac{V_k}{\left| Y_{LO}' + Y_k \right|} = 0, \tag{2.14}$$

and rearranging to produce the best estimate of the LO current:

$$I_{LO}' = \sum \frac{V_k}{\left|Y_{LO}' + Y_k\right|} \bigg/ \sum \frac{1}{\left|Y_{LO}' + Y_k\right|^2}. \tag{2.15}$$

This is substituted back into the error function (Equation (2.13))to produce:

$$\varepsilon = \sum V_k^{\,2} - \left(\sum \frac{V_k}{\left|Y_{LO}' + Y_k\right|} \right)^2 \bigg/ \sum \frac{1}{\left|Y_{LO}' + Y_k\right|^2}. \tag{2.16}$$

A computer program was written to implement this procedure. From the I-V curves, the RF voltage at various points was known, and the junction admittance was calculated. The minimum error was then found by varying the estimated LO admittance. Note that the junction parameters were *not* calculated for every iteration of the LO admittance since the junction admittances were known at this point.

2.7.3 Results

First, the minimum receiver noise and optimum bias as functions of backshort position will be considered. From the bias-tuning hypothesis and the quantum susceptance curve in Figure 2.3, a smooth variation in mixer bias should be expected. However, the July 21, 1994 measurements did not show that. As Tables 2.1 and 2.2 show, over most of the backshort tuning range the optimum bias voltage remained near the photon step centre and did not vary significantly except where the noise performance was poor. Similar results were seen at 105 and 115 GHz. For reference, the gap voltage was 2.55 mV (from the negative peak in Figure 2.3), the middle of the first photon step was 2.32 mV, and the low end of the photon step was 2.10 mV for an LO frequency of 110 GHz.

Next, consider the total power measurements. These were obtained by taking the difference between the pumped I-V curve and the I-V curve with the LO turned off (i.e. the dark current), and finding the bias voltage corresponding to the peak. There was a significant difference between the case with the high LO power, and the case with the low LO power. The total power peaks for the high LO power were fixed at the centre of the photon step, similar to the bias points for the minimum noise temperature given in Tables 2.1 and 2.2. Hence those results are not shown here. The low LO results did show a shift in the detected power peak as the backshort was adjusted, as can be seen in Table 2.3.

Table 2.3: Total power detection peak and amplitude vs. backshort tuning

Backshort	peak (mV)	amplitude (μA)
9.5 turns, .17λ	—	—
9.0 turns, .24λ	2.45	10.5
8.5 turns, .31λ	2.475	9.0
8.0 turns, .38λ	2.50	6.0
7.5 turns, .45λ	2.20	2.75
7.0 turns, .53λ	2.20	9.75
6.5 turns, .60λ	2.35	9.75
6.0 turns, .67λ	2.45	10.75
5.5 turns, .74λ	2.45	9.2
5.0 turns, .81λ	—	—

The final analysis step was to obtain the embedding admittances by applying the voltage match method to the pumped I-V curves. Six points from the pumped I-V curves were used in the fitting procedure to obtain three unknowns. Those points were on the first and second photon steps below the gap voltage. Using these points produced the best fit below the gap voltage. The low and high LO power Smith charts are shown in Figures 2.24 and 2.25 respectively. Solutions with a negative conductance were not plotted. These figures show that the embedding admittance points are consistent with constant-conductance tuning to reasonable accuracy. The scatter in the fitted points will be considered next.

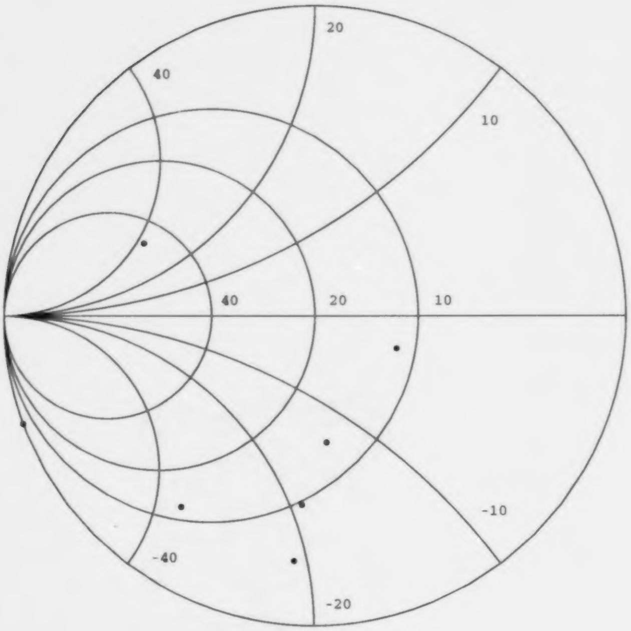

Figure 2.24: Smith chart showing the embedding admittance points at 110 GHz for various backshort settings with the normalized LO voltage amplitude of about 1. The chart is normalized to 20 mS and the full terminal admittances are displayed. The backshort was varied over λ/2 in even steps.

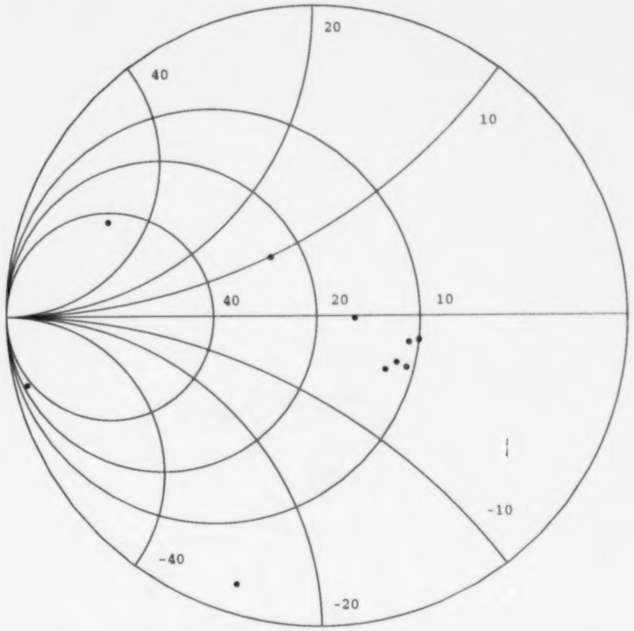

Figure 2.25: Smith chart showing the embedding admittance points at 110 GHz for various backshort settings with the normalized LO voltage amplitude of about 2. The chart is normalized to 20 mS and the full terminal admittances are displayed. The backshort was varied over less than λ/2 in uneven steps. The backshort variation size was smallest (0.1 turn) for the right hand cluster of points and for the points above the resistive axis.

The scatter in the fitted points can be better understood by observing the voltage match error function, Equation 2.16, across the reflection coefficient plane. An example of this is shown in Figure 2.26. Typically the minimum error is within a long, narrow, diagonal contour. Since the error function changes slowly, particularly in the vertical direction, the fitted value is sensitive to measurement errors. For example, Honingh *et al.* [40] estimate that the best that could be expected was an error of ~20% in the real part of the embedding admittance. Since the error contours are longer in the vertical direction, a much larger error in the embedding susceptance should be expected. Therefore the admittance points in Figures 2.24 and 2.25 are consistent with constant-conductance tuning.

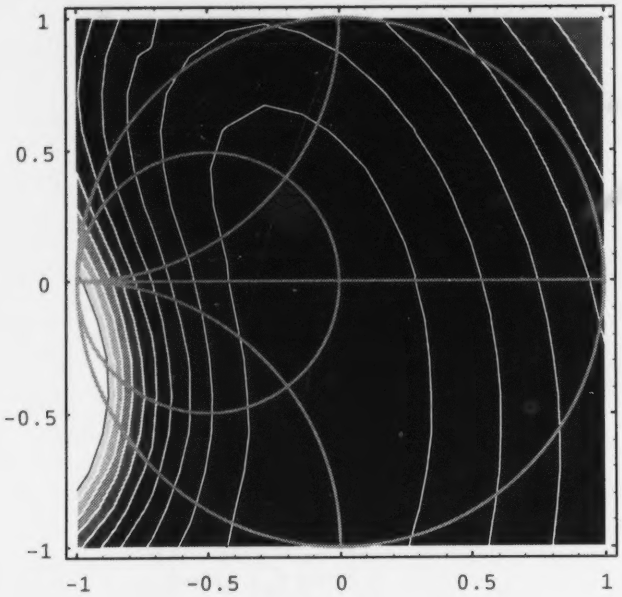

Figure 2.26: Contour plot of the voltage match error function on the reflection coefficient plane. The dark central region has the minimum error. Ten evenly spaced contour levels are shown. The Smith chart is superimposed to indicate the range of allowed admittances.

An example of the quality of fit using a fitted embedding admittance is shown in Figure 2.27. The measured unpumped I-V curve along with a section of a measured pumped I-V curve are shown as solid lines, and fitted points are shown as dots. Although the fit below the gap voltage is good, there is a significant deviation above the gap. Others have observed this [40], and for that reason only points measured below the gap voltage were used in the fit. Mears *et al.* [41] have discussed some of these problems with the voltage match method. They found that the best quality fits were obtained with single junctions because the junctions in series arrays were often not similar enough. Thus the usual assumption that the RF voltage is divided equally across the junctions will not be true. Unfortunately, the experiments in this thesis used a series array of two junctions since good quality single device wafers were not obtained from the three processing runs. Mears *et al.* also found that a large proximity effect (which should be present in the AMC junctions due to the thick aluminum layer) resulted in a poor quality fit above the gap. And finally they found that large sub-gap leakage currents also produced a poor fit. These last two factors are results of the I-V curve not being completely described by Tucker's theory. This produces an error because the fitting assumes that Tucker's theory describes the junction completely.

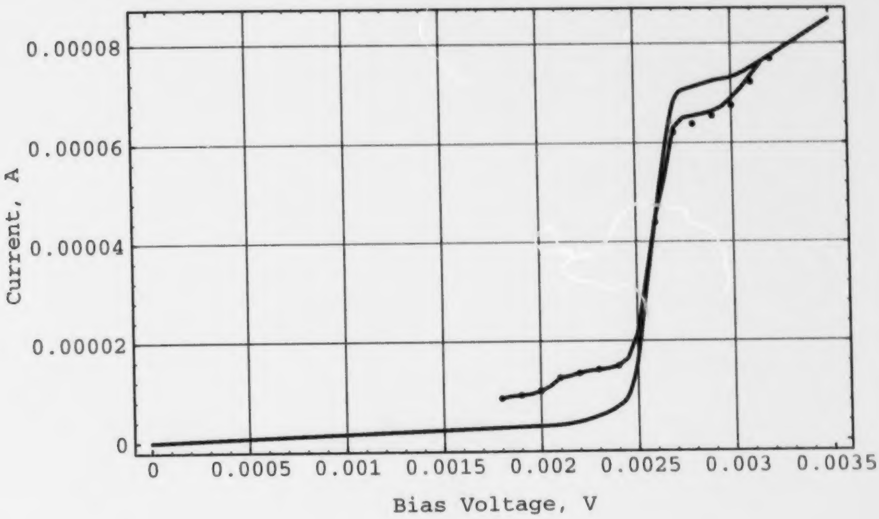

Figure 2.27: Plot of the unpumped I-V curve, photon steps below and above the gap voltage, and points calculated using the deduced embedding admittance.

2.7.4 Comparison with "ideal" SIS junction

It was useful to compare the experimental total power curves with curves obtained theoretically using the digitized unpumped I-V curve, and theoretical curves for a sharp, unpumped, "ideal" SIS junction. These calculations helped to explain what was observed experimentally.

Figures 2.28 and 2.29 show the simulated detected power curves for power levels similar to those used in the experiment. In the simulation the source conductance was equal to the junction quantum conductance and the source susceptance was varied. It can be seen that for the low power curves, the total power response tracked the change in source admittance over part of a photon step. In contrast, the peaks of the high power curves remained at nearly the same spot. This is qualitatively similar to the experimental results.

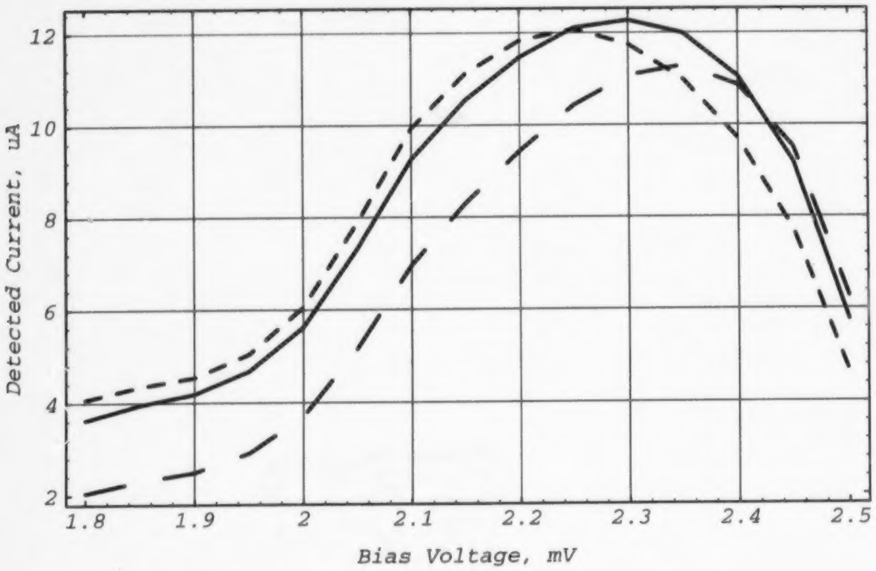

Figure 2.28: Simulated detected power curves using the measured unpumped I-V curve. These curves are for the low LO power case. The solid line represents the centre-tuned case, the line with long dashes represents tuning with a positive susceptance, and the line with short dashes represents tuning with a negative susceptance.

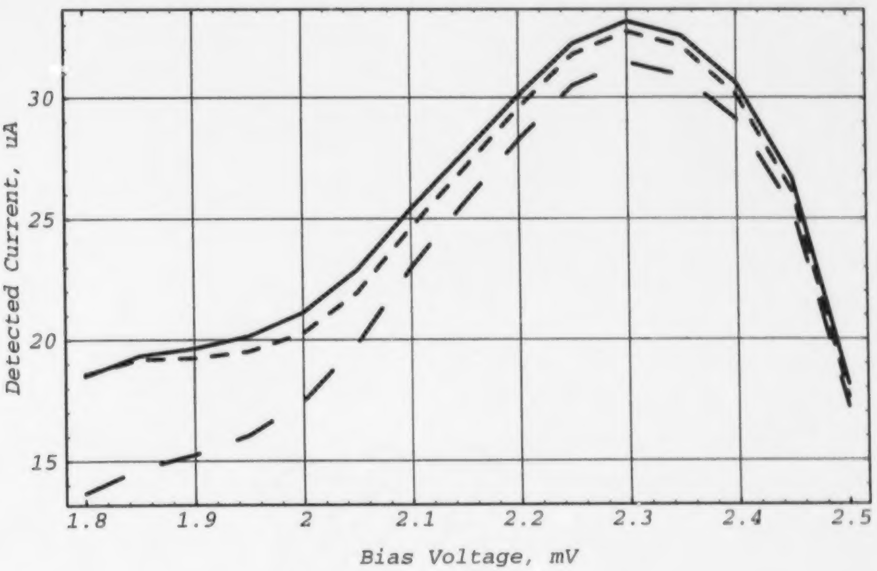

Figure 2.29: Simulated detected power curves using the measured unpumped I-V curve. These curves are for the high LO power case. The solid line represents the centre-tuned case, the line with long dashes represents tuning with a positive susceptance, and the line with short dashes represents tuning with a negative susceptance.

Similar calculations were performed using an "ideal" I-V curve that had no leakage, a very sharp current rise at a gap voltage of 2.5 mV, and a perfect resistive slope above the gap. The low power results are shown in Figure 2.30. Here the peak of the response curve can be seen to track over the entire photon step as the source susceptance is changed. This result strongly suggests that the narrowing of the total power response was due to the width and curvature of the current step at the gap voltage. This can be understood by considering the equation for the pumped curve (from section A.2.2 of the Appendix),

$$I_{pump} = \sum_{n=-\infty}^{\infty} J_n^{\,2}(\alpha) I_{DC}\left(V_0 + n\hbar\omega/e\right). \qquad (2.17)$$

This shows the pumped I-V curve to be the sum of shifted and scaled I-V curves. Thus a rounded I-V curve will result in a rounded total power response.

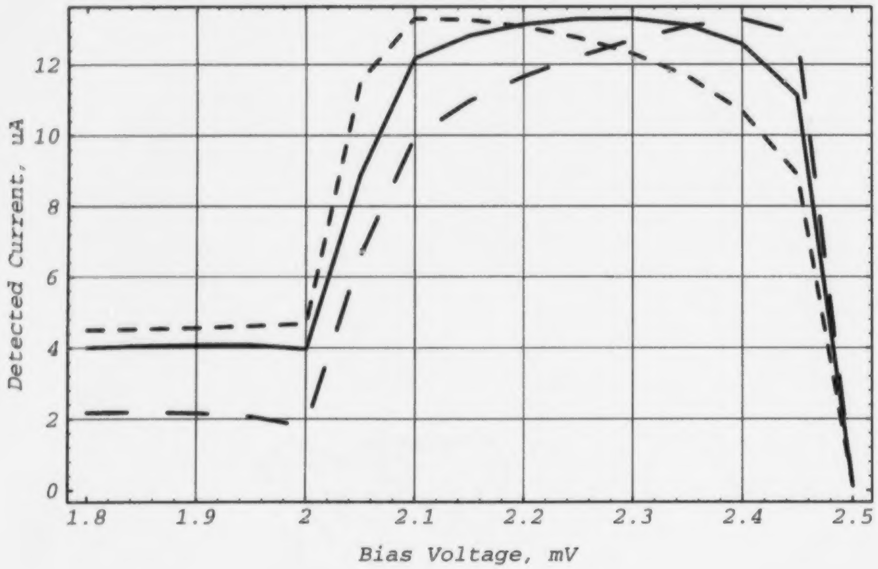

Figure 2.30: Simulated detected power curves using the ideal I-V curve. These curves are for the low LO power case. The solid line represents the centre-tuned case, the line with long dashes represents tuning with a positive susceptance, and the line with short dashes represents tuning with a negative susceptance.

This result makes the heterodyne results (noise temperatures) puzzling because those did not show a shift in minimum noise temperature bias voltage with source admittance. The theory was re-examined to find the source of this discrepancy.

The first test was to check that the admittance seen at the signal port also varied like the quantum susceptance. Expanding equation 4.51 of Tucker and Feldman [7] produces

$$B_{11} \cong \frac{e}{2\hbar\omega_1}\left[I_{KK}(V_0+\hbar\omega_1/e)+I_{KK}(V_0-\hbar\omega_1/e)-2I_{KK}(V_0)\right] \quad (2.18)$$

for small values of α. This can be compared with the susceptance seen by the local oscillator, also for small α:

$$B_Q \cong \frac{e}{2\hbar\omega}\left[I_{KK}(V_0+\hbar\omega/e)+I_{KK}(V_0-\hbar\omega/e)-2I_{KK}(V_0)\right]. \quad (2.19)$$

Since $\omega \approx \omega_1$, the susceptances are very similar. A similar analysis shows that the two conductance equations are similar. Thus the absence of bias tuning was not due to a lack of tuning susceptance at the signal port of the mixer.

The next test was to calculate the mixer gain using the actual unpumped I-V curve. Equations (4.72) to (4.77) of [7] were used for this. Several different source susceptances were used and the gain was plotted as a function of bias voltage. These results showed that the voltage for the peak gain was nearly independent of source tuning, although the amplitude of the gain did depend upon the source. This was a theoretical confirmation of what was observed, but it did not aid in understanding the reason for lack of bias tuning.

Tucker and Feldman's mixer gain equations used above are written in a form that makes it difficult to see what is happening in the mixer. To clarify the situation, their available gain equation (4.61) was rewritten from

$$L^{-1} = 4G_S G_L \left|Z_{01}\right|^2 \tag{2.20}$$

to

$$L^{-1} = 4R_S R_L \left|Y_{01}\right|^2 \tag{2.21}$$

by replacing the Norton equivalent sources on the mixer ports with Thévenin equivalent sources. The resistances and conductances are denoted by R and G respectively, and the source and load by subscripted S and L respectively. Also, $R_S = G_S / \left|Y_S\right|^2$. Now the transconductance can be observed directly rather than taking the inverse of the Y matrix to produce the Z matrix. The transconductance for a small amplitude LO signal and an IF much smaller than the LO frequency can be written as:

$$Y_{01} \cong \frac{e}{\hbar\omega} J_0(\alpha) J_1(\alpha) \left[I_{DC}(V_0 + \hbar\omega/e) + I_{DC}(V_0 - \hbar\omega/e) - 2I_{DC}(V_0) \right]. \tag{2.22}$$

When this was calculated using the real I-V curve, the result was peaked near the centre of the first photon step below the gap voltage. This is where the largest gain and lowest noise were found experimentally. A calculation was then performed using an ideal I-V curve, and this produced a nearly flat curve. Thus the rounding of the transition at the gap voltage limits the bias tuning. This can be seen from Equation (2.22) which shows Y_{01} to be the difference between the unshifted I-V curve, and the mean of the I-V curves shifted up and down by one photon step.

The operation of the mixer can now be understood. The dominant factor is the coupling from the signal port to the IF port, Y_{01}. This coupling is greatest, for the SIS junctions used here, at the centre of the photon step. The maximum LO power will not necessarily be absorbed at the centre of the photon step, as shown by the total power results. However, the overall conversion gain is greatest at the centre of the photon step because Y_{01} is only a weak function of the LO voltage amplitude. This can be seen by evaluating the product of the two Bessel functions in Equation (2.22): a maximum occurs near α of about 1, which is the usual operating point for SIS mixers. Thus Y_{01} dominates the gain of the mixer, forcing the peak gain (and minimum noise) to the centre of the first photon step below the gap voltage.

2.8 Conclusions

The receiver described here had a noise temperature of about 50K at 110 GHz which is 10× the quantum limit of 5K. This is a good result considering that the IF amplifier used had a noise temperature of about 10K. Other indications of high sensitivity were the presence of flat or negative sloping photon steps, and instabilities in the mixer as unity conversion gain was approached.

The embedding admittances as functions of backshort position were similar to those predicted by scale model measurements and a computer simulation. Thus constant-conductance tuning was achieved to a good approximation. This also verified the quality of the mixer block design and construction since any discontinuities in the waveguide were small enough that they did not significantly modify the waveguide probe terminal admittance. However, there were two discrepancies in the tuning circles. First, the measured curve was similar in size to the simulated curve, but larger than the scale model curve. Second, the measured curve had a variable step size around the circle, like the simulated results, but unlike the nearly constant steps of the scale model. There was a plan to resolve these differences by repeating the scale model measurements, but access to the vector network analyzer has become very difficult to obtain. It is possible that the connector in the model perturbed the fields sufficiently to produce an error. Another model design that has the connector off-centre may determine if this is the case.

The total power response showed the presence of the quantum susceptance. To some extent a change in waveguide probe terminal impedance could be canceled by changing the bias voltage, which in turn changed the device susceptance. However, this was the case only for signal powers similar to those used by receiver LO's; higher power levels did not show the tuning effect as strongly. The narrowing of tuning deviation with increasing power was shown to be a result of the width of the current rise at the gap voltage.

Bias tuning of the SIS junction as a mixer was not successful. Other than at tuner positions with high minimum receiver noise temperatures, the bias point for lowest noise was largely independent of the backshort tuning. However, the value of the minimum noise temperature was a function of the backshort tuning. The lack of bias tuning was shown to be a result of the finite width of the transition at the gap voltage, which forces the maximum mixer gain to occur at the centre of the photon step.

A number of recommendations can be made for future work. First, bias tuning should not be used as a matching technique. A fixed-tuned, broadband matching circuit should be used instead, and will probably give good results (see, for example, [42]). The second recommendation is that the split mixer block may be suitable for other projects since it is precise yet simple to fabricate. Since 1/5th height waveguide was used here, this has proven the machining technique for full-height guide at frequencies up to nearly 600 GHz. However, there were discrepancies between the modeled, simulated, and measured probe admittances which should be resolved. And finally, the quality of the junctions should be improved, since the voltage match analysis showed that the behavior of the AMC SIS junctions was not entirely described by Tucker's theory. This may also have been a source of error in the measured probe admittances.

2.9 References

[1] W. R. McGrath, V. Lubecke, D. B. Rutledge, "Adjustable RF tuning elements for planar millimeter wave and submillimeter wave circuits," *Digest of the 15th Int. Conf. Infrared and Millimeter Waves*, pp. 244-246, 1990

[2] N. R. Werthamer, "Nonlinear self-coupling of Josephson radiation in superconducting tunnel junctions," *Phys. Rev.* vol. 147, pp. 255-263, 1966

[3] R. E. Harris, "Josephson tunneling current in the presence of a time dependent voltage," *Phys. Rev. B*, vol. 11, pp. 3329-3333, 1975

[4] Q. Hu, C. A. Mears, P. L. Richards, F. L. Lloyd, "Quantum susceptance and its effects on the high-frequency response of superconducting tunnel junctions," *Phys. Rev. B*, vol. 42, pp. 10250-10263, 1990

[5] A. H. Worsham, N. G. Ugras, D. Winkler, D. E. Prober, N. R. Erickson, P. F. Goldsmith, "Quantum tunneling currents in a superconducting junction," *Phys. Rev. Lett.*, vol. 67, pp. 3034-3037, 1991

[6] D. Winkler, N. G. Ugras, A. H. Worsham, D. E. Prober, N. R. Erickson, and P. F. Goldsmith, "A full-band waveguide SIS receiver with integrated tuning for 75-110 GHz," *IEEE Trans MAG*, vol. 27, pp. 2634-2637, 1991

[7] J. R. Tucker, M. J. Feldman, "Quantum detection at millimeter wavelengths," *Rev. Modern Phys.*, vol. 57, pp.1055-1113, 1985

[8] S. Withington, P. Kennedy, "Numerical procedure for simulating the large-signal quantum behavior of superconducting tunnel-junction circuits," *IEE Proc-G*, vol. 138, pp.70-76, 1991

[9] R. N. Bracewell, "The Fourier Transform and its Applications," New York: McGraw-Hill, p. 274, problem 12, 1978

[10] S. B. Kaplan, C. C. Chi, D. N. Langenberg, J. J. Chang, S. Jafarey, and D. J. Scalapino, "Quasiparticle and phonon lifetimes in superconductors," *Phys. Rev. B*, vol. 14, pp. 4854-4873, 1976

[11] N. G. Ugras, A. H. Worsham, D. Winkler, D. E. Prober, "Quasiparticle-tuned superconducting mixer," *Appl. Phys. Lett.*, vol. 62, pp. 3519-3521, 1993

[12] *Em User's Manual*, Liverpool, NY: Sonnet Software, Inc, Sept. 1993

[13] J. C Rautio, R. F. Harrington, "An Electromagnetic Time-Harmonic Analysis of Shielded Microstrip Circuits," *IEEE Trans. MTT*, vol. 35, pp. 726-730, 1987

[14] R. E. Collin, *Field Theory of Guided Waves*, NewYork: IEEE Press, p. 482, 1991

[15] Y.-C. Shih, "Design of waveguide E-plane filters with all-metal insert", *IEEE Trans. MTT*, vol. 32, pp. 695-704, 1984

[16] A. Räisänen, W. R. McGrath, D. G. Crete, and P. L. Richards, "Embedding impedance measurements for mm-wave mixers," In: *Advanced Microwave Mixer Technology*, Microwave Exhibitions and Publishers, Ed.:T. Oxley, pp. 479-484, 1989

[17] B. A. Syrett, "A broad-band element for microstrip bias or tuning circuits," *IEEE Trans. MTT*, vol. 28, pp.925-927, 1980

[18] R. L. Kautz, "Picosecond pulses on superconducting striplines," *J. Appl. Phys.*, vol. 49, pp. 308-314, 1978

[19] H. K. Olsson, "Dielectric constant of evaporated SiO at frequencies between 13 and 103 GHz," *IEEE Trans. Mag.*, vol. 25, pp. 1115-1118, 1989

[20] S. -K. Pan, M. J. Feldman, A. R. Kerr, and P. Timbie, "Low-noise 115-GHz receiver using superconducting tunnel junctions," *Appl. Phys. Lett.*, vol. 43, pp. 786-788, 1983

[21] A. R. Kerr, "An adjustable short-circuit for millimeter waveguides," *NRAO Electronics Division Internal Report*, No. 280, July, 1988

[22] M. K. Brewer, A. V. Räisänen, "Dual-harmonic noncontacting millimeter wavelength backshorts: theory, design, and test," *IEEE Trans. MTT*, vol. 30, pp. 708-714, 1982

[23] B. N. Ellison, L. T. Little, C. M. Mann, and D. N. Matheson, "The quality and performance of tunable waveguide backshorts," *Electronics Lett.*, vol. 27, 1991

[24] M. Gurvitch, M. A. Washington, H. A. Huggins, "High quality refractory Josephson tunnel junctions utilizing thin aluminum layers," *Appl. Phys. Lett.*, vol. 42, pp. 472-474, 1983

[25] H. G. LeDuc, B. Bumble, S. R. Cypher, A. J. Judas, and J. A. Stern, "Sub micron area Nb/AlO$_x$/Nb tunnel junctions for submm mixer applications," *Proc. Third Int. Symposium on Space Terahertz Tech.*, pp. 408-418, 1992

[26] J. M. Dutta, C. R. Jones, H. Davé, "Complex dielectric constants for selected near-millimeter-wave materials at 245 GHz," *IEEE Trans. MTT*, vol. 34, pp. 932-936, 1986

[27] Aremco Products, Inc., P. O. Box 429, Ossining, NY 10562 USA

[28] J. M. Eldridge, J. Matisoo, "Measurement of tunnel current density in a metal-oxide-metal system as a function of oxide thickness," *Proc. 12th Int. Conf. on Low Temp. Physics*, pp. 427-428, 1970

[29] S. M. Sze, *VLSI Technology*, New York:McGraw-Hill, second edition, 1988

[30] H. Kroger, L. N. Smith, and D. W. Jillie, "Selective niobium anodization process for fabricating Josephson tunnel junctions," *Appl. Phys. Lett.*, vol. 39, pp. 280-282, 1981

[31] P. Feautrier, M. Hanus, P. Febvre, "Nb/Al-AlO$_x$ /Nb junctions for a 380 GHz SIS receiver," *Supercond. Sci. Technol.*, vol. 5, pp. 564-568, 1992

[32] H. Yamamori, T. Miura, A. Fujimaki, Y. Takai, and H. Hayakawa,"Study on the transition width at gap voltage caused by the proximity effect in Nb-based Josephson junctions," *Supercond. Sci. Technol.*, vol. 7, pp. 284-286, 1994

[33] T. Imamura, S. Hasuo, "Cross-sectional TEM observation of Nb/AlOx-Al/Nb junction structures," *IEEE Trans. MAG*, vol. 27, pp. 3172-3175, 1991

[34] C. K. Walker, J. W. Kooi, M. Chan, H. G. LeDuc, P. L. Schaffer, J. E. Carlstrom, and T. G. Phillips, “A low-noise 492 GHz SIS waveguide receiver,” *Int. J. Infrared Millimeter Waves*, vol. 13, pp. 785-798, 1992

[35] K. H. Gundlach, D. Billon-Pierron, M. Rosengarten, A. Karpov, T. Lehnert, H. Rothermel, “Double-barrier tunnel junctions for quasiparticle mixers,” *J. Appl. Phys.*, vol. 75, pp. 4097-4102, 1994

[36] Infrared Laboratories, Inc., 1808 East 17th Street, Tucson, AZ 85719

[37] J. Ibruegger, “Transmission of room-temperature radiation by materials at low temperatures,” *Int. J. Infrared Millimeter Waves*, vol. 5, pp. 655-665, 1984

[38] S. Weinreb, D. L. Fenstermacher, R. W. Harris, “Ultra-low-noise 1.2- to 1.7 GHz cooled GaAsFET amplifiers,” *IEEE Trans. MTT*, vol. 30, pp. 849-853, 1982

[39] A. Skalare, “Determining embedding circuit parameters from DC measurements on quasiparticle mixers,” *Int. J. Infrared Millimeter Waves*, vol. 10, pp. 1339-1353, 1989

[40] C. E. Honingh, J. J. Wezelman, M. M. T. M. Dierichs, G. de Lange, H. H. A. Schaeffer, T. M. Klapwijk, and Th. de Graauw, “Extensive test of the three-port quantum mixer theory on 345 GHz superconductor-insulator-superconductor mixers,” *J. Appl. Phys.*, vol. 74, pp. 4762-4773, 1993

[41] C. A. Mears, Q. Hu, P. L. Richards, A. H. Worsham, D. E. Prober, and A. Räisänen, “Quantum limited quasiparticle mixers at 100 GHz,” *IEEE Trans. Mag.*, vol. 27, pp. 3363-3369, 1991

[42] R. Blundell, C.-Y. E. Tong, D. C. Papa, R. L. Leombruno, X. Zhang, S. Paine, J. A. Stern, H. G. LeDuc, and B. Bumble, “A wideband fixed-tuned SIS receiver for 200-GHz operation,” *IEEE Trans. MTT*, vol. 43, pp. 933-937, 1995

Chapter 3:

An Integrated Josephson Current Suppression Electromagnet for SIS Receivers†

3.0 Introduction

Over the last decade there has been much progress in building integrated superconductor-insulator-superconductor (SIS) mixers. Two major accomplishments were the development of integrated circuit antennas [1], and planar transmission line matching circuits which provide broadband low noise performance for micron-scale junctions [2, 3]. These mixers are now competitive in performance with traditional designs using feed horns and waveguide, but are simpler to fabricate and assemble [4]. In this chapter a further level of integration is described in which the Josephson effect suppression electromagnet is also put on the mixer chip through a simple modification of the microstrip matching transformer [5].

SIS mixers operate by the photon-assisted tunneling of quasiparticles. Unfortunately, at zero bias voltage a Cooper pair tunneling current flows due to the Josephson effect. At frequencies higher than ~300 GHz the optimal DC bias for the SIS junction is low enough that the instantaneous local oscillator voltage swing will cause the bias point to switch from the quasiparticle tunneling branch of the IV curve, to the Cooper pair tunneling branch, and back [6]. This generates noise at the intermediate frequency port. However, it is well known that if an integral number of flux quanta pass through an SIS junction, the Josephson effect tunneling current will be suppressed. Rudner *et al.* [7] have shown that suppressing the Josephson effect dramatically reduces excess noise and this technique is now standard for submillimetre SIS receivers.

The Josephson effect is usually suppressed with a solenoid of superconducting wire mounted close to the mixer. The new on-chip RF matching circuitry has helped by permitting larger area junctions to be used which have a larger cross-sectional area with which to catch the flux lines. The technique described here goes one step further and uses the matching line itself to generate the magnetic field.

3.1 Theory of Josephson current suppression

To understand how a magnetic field suppresses the Josephson effect, begin by considering a simple superconducting loop. It is well known that the superconducting wavefunction has long-range phase coherence [8]. This means that if the phase and momentum are known at one point, the phase can be calculated for any other point on the line. An analogy is an electromagnetic wave on a transmission line: knowing the phase and wavelength at one point allows one to calculate the phase at other points. A result of this property is that a superconducting loop will only support wavefunctions that have a phase change around the loop equal to an integer multiple of 2π. This quantization of the phase around a superconducting loop in turn leads to the quantization of the flux passing through the loop. It has been shown that the relationship between the superconducting phase and the flux around a conductor is $\Delta\varphi = 2e\Phi/\hbar$ [8 and Appendix A.4.2]. With a complete loop, the minimum flux passing through the centre required to produce a phase change of 2π is the magnetic flux quantum $\Phi_0 = h/2e$.

---

† A version of this chapter has been published: B. Veidt, K. Kornelsen, J. F. Vaneldik, D. Routledge, and M. J. Brett, "Integrated Josephson effect suppression electromagnets for SIS receivers," *Int. J. Infrared Millimeter Waves*, vol. 16, pp. 1223-1230, 1995

Next take a junction and divide it into m parallel sub-junctions, as shown in Figure 3.1. The sub-junctions are joined with loops that have a flux line at the centre. The two end junctions are half width and have half the critical current to maintain a constant flux density throughout the junction. For a single sub-junction, the current as a function of the wavefunction phase is $I = I_k \sin\varphi_k$ and for all the sub-junctions it is $I = \sum_{k=1}^{m} I_k \sin\varphi_k$. For the end sub-junctions the junction critical current is $I_1 = I_m = I_o/2(m-1)$ and for the inner sub-junctions it is $I_k = I_o/(m-1)$ The flux is divided equally so that the flux passing through each loop is $\Phi/(m-1)$. For a single loop the phase is not restricted to integer multiples of 2π since the loops are not continuous superconductors. The phase around a loop is $\Delta\varphi = \varphi_k - \varphi_{k-1} = \dfrac{2e\Phi}{\hbar(m-1)}$. Going across the junction these phases and their effect on the Josephson current can be summed up with the equation:

$$I = \frac{I_0}{2(m-1)}\sin\varphi_1 + \sum_{k=2}^{m-1}\frac{I_0}{(m-1)}\sin\left(\frac{2e\Phi}{\hbar(m-1)} + \varphi_{k-1}\right) + \frac{I_0}{2(m-1)}\sin\left(\frac{2e\Phi}{\hbar(m-1)} + \varphi_{m-1}\right). \quad (3.1)$$

Next, by setting the flux equal to one flux quantum and the phase at one edge of the junction equal to zero, Equation (3.1) is simplified to

$$I = 0 + \frac{I_0}{(m-1)}\sum_{k=2}^{m-1}\sin\left(\frac{2\pi}{m-1} + \varphi_{k-1}\right) + 0. \quad (3.2)$$

Thus for any m, if the angles are plotted on a unit circle, it can be seen that the points are all paired with points on the opposite side of the circle and thus cancel. This is the case for any φ_1 or integer m. This is one way to understand how the Josephson effect can be suppressed with a magnetic field.

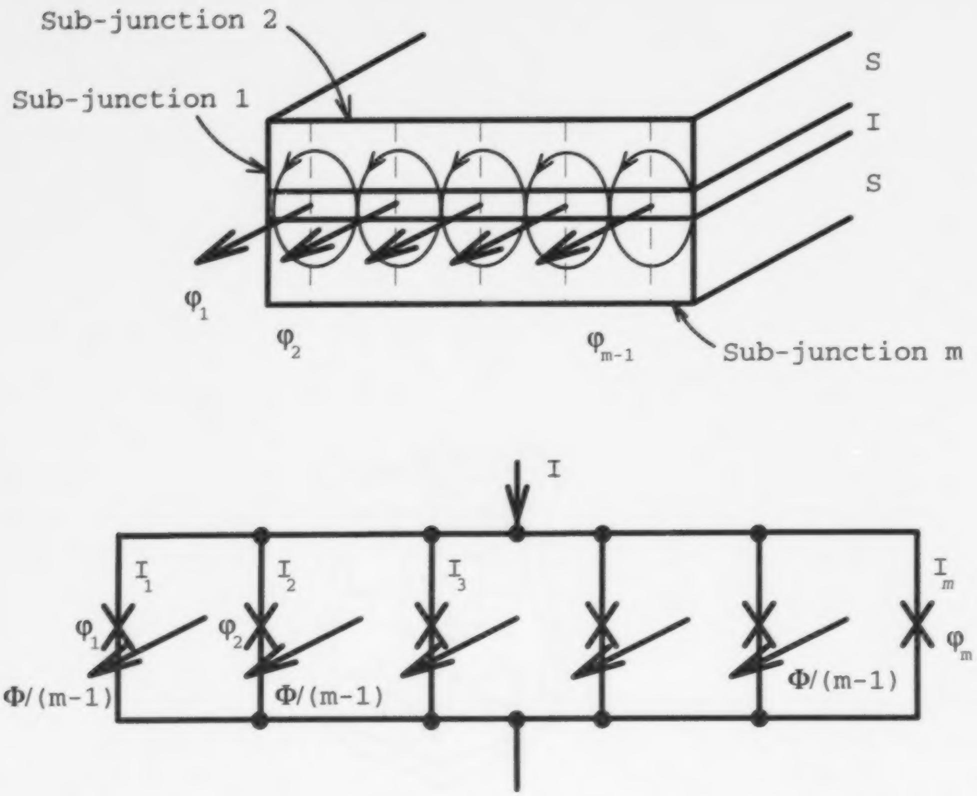

Figure 3.1: The suppression of the Josephson current by a magnetic field can be explained using a junction and magnetic flux divided into many discrete pieces. The top sketch shows a junction with magnetic flux passing through the insulator, and the bottom schematic shows the equivalent circuit.

3.2 The technique

Figure 3.2 shows an SIS mixer without integrated Josephson current suppression. At the top is a schematic representation of DC bias and intermediate frequency circuitry standard to all SIS receivers. Below that is an antenna which is coupled to an SIS device through a microstrip line which transforms the antenna admittance to match the quantum conductance of the SIS junction. The junction susceptance caused by the geometric capacitance of the parallel-plate structure of the device is then tuned out with a shunt stub. Such circuitry allows for a broader bandwidth and permits the use of larger area junctions than would be the case if the junction was connected directly to the antenna [3].

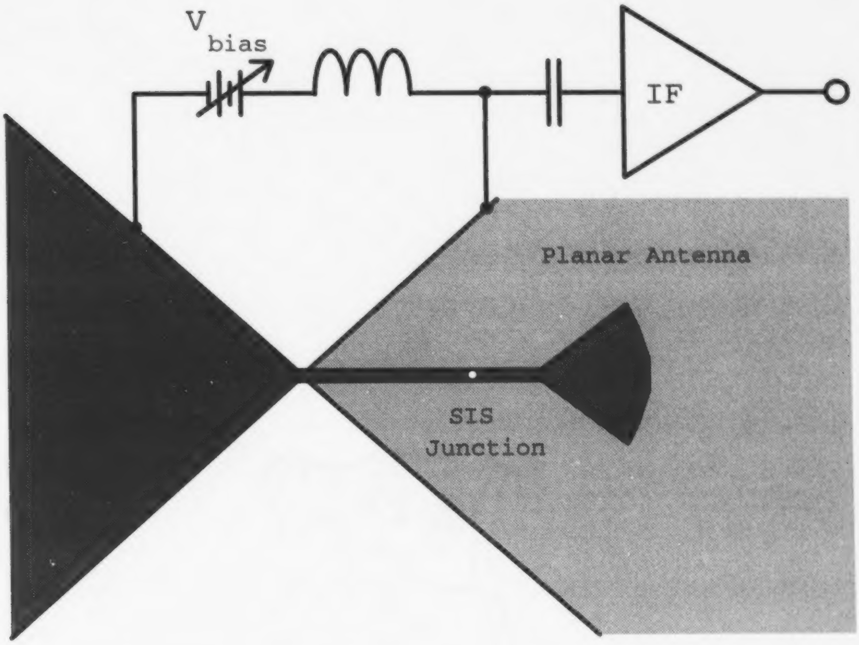

Figure 3.2: Schematic of SIS mixer before modifications.

The modified circuit is shown in Figure 3.3. An additional bias line (without shading) has been added to the right-hand side of the radial stub so that a DC current can be passed through the microstrip line to generate a magnetic field. Because of the Meissner effect, the flux is concentrated in the gap between the line and the ground plane, and also through the junction. At the bottom of the figure is the electromagnet current source with decoupling to prevent leakage of the IF signal down this path.

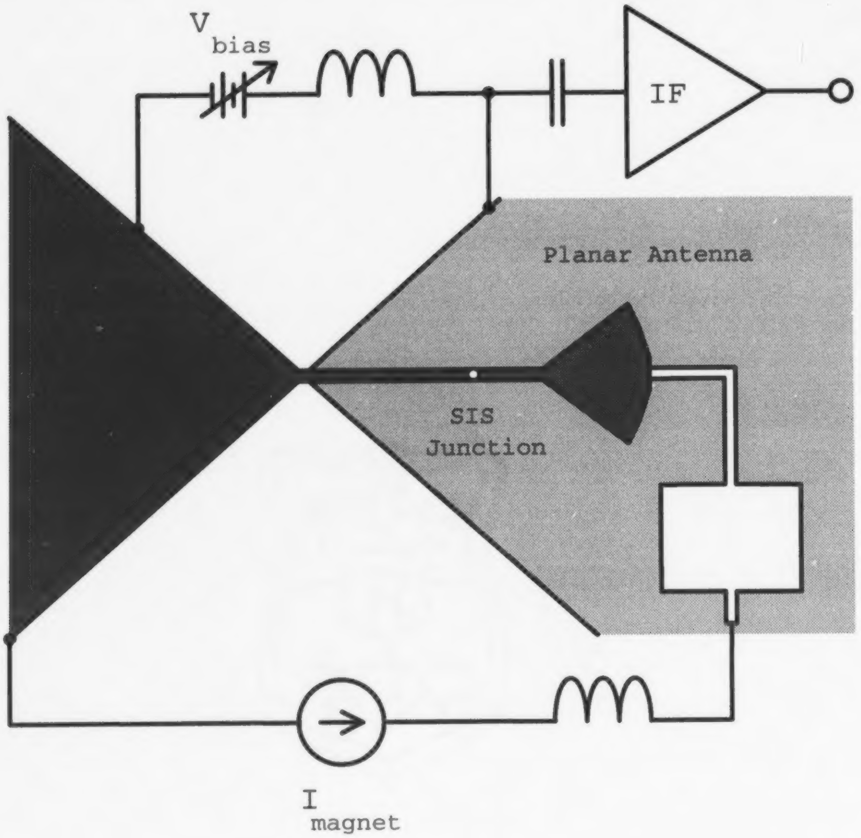

Figure 3.3: Schematic of SIS mixer modified with an integrated Josephson effect suppression electromagnet.

The current required to suppress the Josephson effect is calculated below. Precise numbers are not needed, since the current supply must be adjustable to account for ambient flux passing through the SIS junction. Thus details such as field fringing have been neglected. These calculations should be regarded as estimates to be used by the receiver designer to determine if the design exceeds the critical current of the superconducting film and to specify the current source size.

Beginning with Ampère's law, the flux strength as a function of current can be calculated:

$$\int_S \mathbf{J} \cdot d\mathbf{a} = \oint \mathbf{H} \cdot d\mathbf{l} \tag{3.3}$$

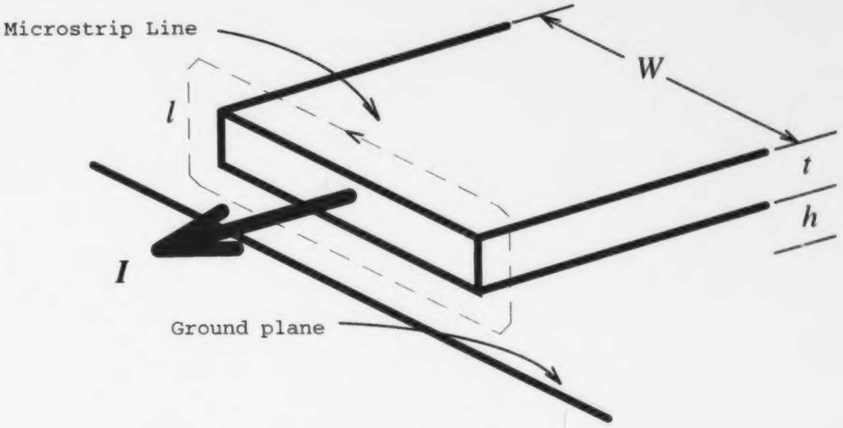

Figure 3.4: A perspective view of a cut through a microstrip line carrying current **I**. The dashed line of length *l* follows a magnetic field line around the conductor. The microstrip line has width *W*, thickness *t*, and height *h* above the ground plane.

where the quantities are defined in Figure 3.4. Equation (3.3) is simplified to

$$I = H\,l \tag{3.4}$$

because the path of integration is along a flux line. The integration path length is approximated by $l = 2\,W$ since the line width is much greater than both the film thickness and the gap between the ground plane and the line. Additional relationships are $B = \mu_0 H$ and $\Phi = B\,A_j$ where A_j is the area that the flux lines pass through. A_j equals the junction length L multiplied by the height, which is twice the magnetic penetration depth λ_L (assuming that the insulator thickness is much less than λ_L). The effect of the ground plane is included by using the method of images [8] which shows that the flux is simply doubled. Substituting these relations into Equation (3.4) produces:

$$\Phi = \frac{\mu_0 I A_j}{W} = \frac{2\mu_0 I \lambda_L L}{W}. \tag{3.5}$$

The first null occurs with one flux quantum passing through the junction, that is with $\Phi = \Phi_0 = 2.07\times10^{-15}$ Wb or when the current is

$$I = \frac{\Phi_0 W}{2\mu_0 \lambda_L L}. \tag{3.6}$$

A practical minimum current can be found if the junction is assumed square and if the overlying line is the same width. The *W* and *L* terms cancel leaving a minimum current equal to .82 Amp/λ_L with λ_L in nanometres. For niobium based mixers where $\lambda_L \cong 85$ nm, the minimum current is about 9.7 milliamps. Niobium nitride has $\lambda_L \cong 380$ nm and thus requires a minimum current of 2.2 milliamps. Although a number of approximations have been made, including the assumption that fringing fields are negligible, these are useful rules of thumb for receiver designers.

A final concern is whether the superconducting thin films can carry the necessary currents. Imamura *et al.*[9] have measured a critical current density of 25 milliamps per μm of line width for niobium films ~100 nm thick. Since most line widths will be at least several μm, the current-carrying capacity of niobium is adequate for this application. Of course, in actual receivers the line width will probably be larger than the junction length, but this could be compensated by using a rectangular junction.

3.3 Verification

A receiver designer will have two concerns before implementing this technique. The first is that the Josephson current is actually suppressed as predicted, and the second is that this structure can be implemented without degrading the RF performance of the mixer. Those concerns will be addressed here.

3.3.1 Verification with a receiver

Originally this idea was to be tested with an actual receiver, but out of three processing runs there were no suitable devices. The first batch was made on substrates covered with small pits, and only a few locations were clean enough to produce working RF devices. Unfortunately none of the working devices had the integrated Josephson suppression magnet. The second and third batches had a series resistance of several tens of ohms, making them unsuitable for use. The mask design was based on the assumption that *all* niobium layers exposed to air would be capped with gold to prevent oxidation of the surface, but only the trilayer had gold on it. This oxide layer was the source of the series resistance. There was an unsuccessful effort to penetrate the oxide using wiring bonding. Other factors worked to prevent an RF test such as the change to part-time status of the junction maker and the near exhaustion of funds to buy the junction maker's services. Nevertheless, it is useful to look at the RF design.

The design for this mixer was based on a 110 GHz waveguide mixer block. There are several reasons for this particular choice. The first is that the 110 GHz receiver system worked very well and was well understood. So although the Josephson effect usually does not cause problems at such low frequencies, it would be possible to see if the circuit modifications affected receiver performance. As well, the Josephson noise is visible in lower frequency mixers if the bias is adjusted low enough, so it would be possible to see if it was suppressed. This technique will be best suited for planar designs which have large area contact pads, but I felt that I could contact an additional pad on a 0.5 mm wide 110 GHz device.

The main problem in this design was to find a way to get the additional bias line to the microstrip line. Waveguide mixers usually have two bias lines leaving the centre of the chip, going to opposite ends. The lines are in the form of low-pass filters to prevent signal power at 110 GHz from leaking down the lines. Since the IF signal also leaves the mixer on these lines, the low-pass filter must not affect that signal. Thus there are two design specifications: the additional bias line must not provide a leakage path for 110 GHz signals, and it must not interfere with the IF signal.

The solution was to place two narrower lengths of low-pass filters in parallel, as shown in Figure 3.5. The low-pass filters are constructed using alternating sections of high and low impedance line, each λ/4 long, and corrected in length for field fringing. Although the first sections of high impedance line to the right of the bow-tie probe are closely spaced, the second and third have a wide separation. The reason for doing this is to prevent slot line modes at 110 GHz from propagating down the gap between the high impedance sections of the bias filter. This works because the velocity of propagation is similar for slot line and microstrip, and each section is a quarter wave long. At low frequencies the magnet bias line is at ground potential, so there should be little leakage of IF signal down this line. To ensure that, an external inductance was to be placed in series to provide a blocking impedance (see Figure 3.3).

Figure 3.5 provides a scale representation of the design. The overall dimensions of the substrate are 6 mm long × 0.5 mm wide × 70 μm thick. The dimensions of the ground contact pad are 800 μm × 250 μm, the electromagnet bias pad are 430 μm × 185 μm, and the IF/junction bias pad are 370 μm × 250 μm. The waveguide probe and the low impedance sections in the ground bias line are 400 μm wide. The low impedance sections in the other two bias lines are 195 μm wide. All low impedance sections are 350 μm long. The high impedance lines are 10 μm wide and 420 μm long. The minimum line spacing is 10 μm.

Due to their small size, the junction and matching circuitry are not shown in Figure 3.5, but are very similar to Figure 3.3. The microstrip line is 6 μm wide and is on 0.3 μm of SiO, giving a characteristic impedance of 9.3 Ω and a velocity of propagation 0.35 that of radiation in free space. A radial stub with a radius of 135 μm provides a low impedance at 110 GHz, and with a series line of 83 μm to place it in shunt with the junction. This will resonate with the junction capacitance and quantum susceptance. A further 240 μm (λ/4) of microstrip matches the junction area of 9 μm^2 and 2.2 Ω normal resistance to the waveguide probe impedance of 40 Ω. Variations on this design kept the junction area constant, but varied the dimensions: square junctions with sides of 3 μm × 3 μm, rectangular junctions with sides of 2 μm × 4.5 μm, and line junctions with sides of 1 μm × 9 μm were drawn. The reason for doing this was to try longer junctions that would require less electromagnet current to intercept one flux quantum.

This design was verified using an electromagnetic simulator suitable for planar transmission line circuits [10, 11]. The first test was of the parallel bias filter design. The model tested consisted of the low impedance section adjacent to the triangular probe, the first high impedance sections, and the following low impedance sections. The electromagnet bias line was connected to the first low impedance section through resistors of various values: 0.5 Ω, 5 Ω, and infinity. This model was compared with a similar model that did not have a parallel filter. The reflection coefficient was measured for these different configurations, and the largest change in phase was ~0.2°. The conclusion from this is that the parallel filter design had essentially no effect on the waveguide probe.

The second test involved a model of the microstrip circuit. The electromagnet bias line was left open circuited (as it should appear if the filters work properly), the input end was terminated with the waveguide probe impedance, and the reflection coefficient was measured at the junction location. When compared with the same circuit without the bias line, the change in the reflection coefficient was less than 1%.

Although it was not possible to perform an RF test with this design, the computer simulations provide strong support that the modifications needed to implement integrated Josephson current suppression will not adversely affect the RF performance of the mixer. The parallel bias lines may have application in waveguide circuits where the probe is formed on thin silicon nitride films [12].

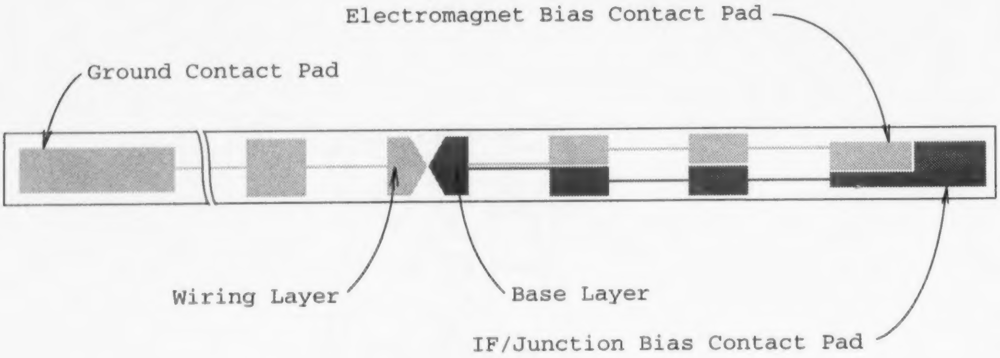

Figure 3.5: Design of RF mixer circuit with an integrated Josephson suppression electromagnet. An additional bias line for the magnet has been added to the right-hand side of the device.

3.3.2 Verification with a DC SQUID

Fortunately, much of this technique could be tested using a DC superconductive quantum interference device (SQUID), as shown in Figure 3.6. This SQUID was originally designed for measuring the inductance of superconducting microstrip lines, but the geometry was well suited for this experiment. This circuit consisted of two 4 μm × 4 μm niobium junctions on a ground plane joined by a wiring layer 6 microns wide. The dielectric was 0.3 μm of SiO. The DC bias circuit allowed the IV curve to be monitored while current was passed through the wiring layer.

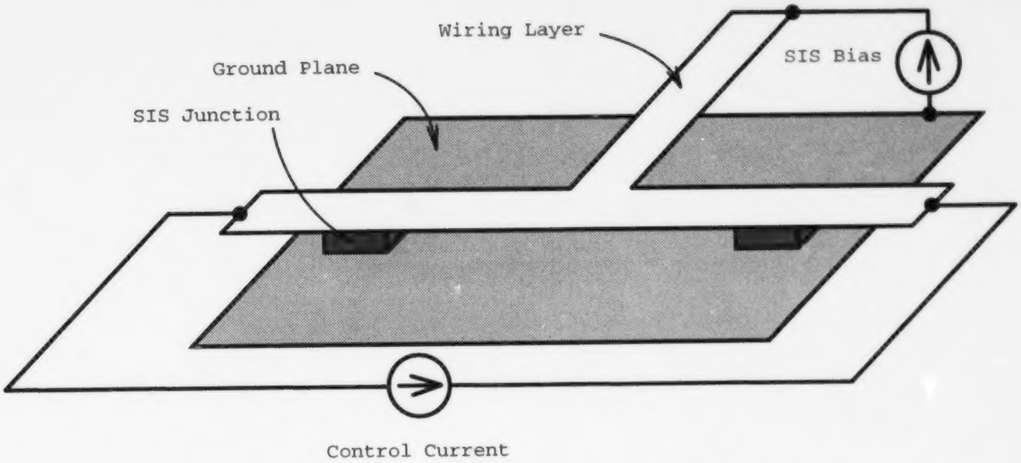

Figure 3.6: Schematic representation of the DC SQUID circuit used to demonstrate Josephson current suppression. The wiring, junctions, and ground plane are not to scale and are drawn with a perspective view to show the different layers.

Figure 3.7 shows the normalized Josephson current as a function of the control current through the wiring layer. The errors on these points is about ±0.01. Points for the Josephson current below about 0.1 were not recorded because the jump between the Josephson tunneling curve and the quasiparticle tunneling curve became rounded, making measurement of the height of the Josephson current difficult. These points were very close to zero. The solid line is the curve $\sin(\pi\Phi/\Phi_0)/(\pi\Phi/\Phi_0)$ rewritten in terms of current and fitted to the data points. This function is what should be expected when the junctions have a uniform current density distribution [7]. The control current (13.1 mA) that produces the first null is about 10% lower than predicted by the simple theory, but that could be due to errors in the line dimensions, junction size, or the magnetic field penetration depth. There is a slight horizontal offset in the curve which is probably due to flux trapped in the junctions as they were cooled.

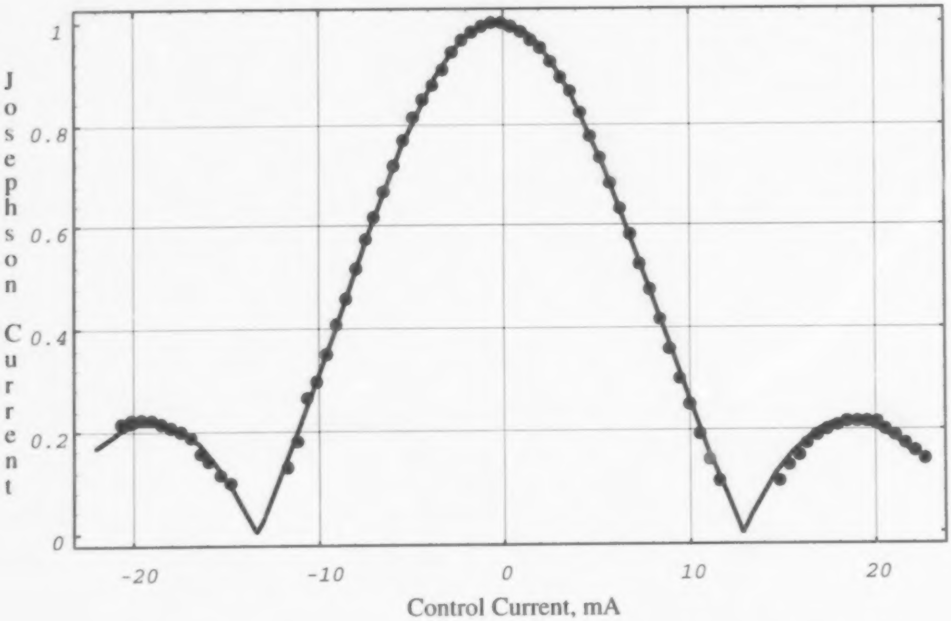

Figure 3.7: Plot of Josephson current as a function of control current through overlying microstrip line. The Josephson current has been normalized to the peak value. The solid line is a fit of the theoretically expected function to the data points.

3.4 Practical concerns

The main limitation of this particular implementation is expected to be that some matching circuits require a wide microstrip line to cover the junction [4], which would then require a large DC magnet current.

Another possible problem is the current carrying capacity of the niobium film. This is usually not a concern for most receiver builders since most SIS junctions do not require large bias currents. However, it was found that the films produced in the AMC SIS process had lower critical currents than reported in [9]. Part of this was due to thinning of the film as it passed over steps in SiO thickness. The solution used was to extend the SiO coverage so that the wiring layer always had a layer of SiO beneath it, minimizing steps below the wiring. An alternative solution would be to rearrange the order of layers so that the electromagnet layer is directly on the quartz substrate.

A final problem is contacting to the bias pads. This design requires that at least one more bias pad be placed on the mixer chip. Waveguide mixers are on substrates between 50 and 100 microns wide, so contacting a third pad would be extremely difficult. However, planar antenna mixers usually have a much larger substrate; therefore contacting an additional bias pad should not be a problem. Having additional pads will be very useful for this technique since that will permit separate current supply pads and voltage sensing pads, and thus minimize the interaction between the low current junction bias and the high current magnet bias.

3.5 Conclusions

A new method of suppressing the Josephson current in SIS mixers has been described. This technique requires only a simple modification to the style of tuning circuit shown in Figure 3.2. In most cases, the magnet current should be on the order of a few tens of milliamps. Because of the need for an additional bias connection pad, the method will be best suited to quasi-optical receiver designs which usually have larger substrate areas than do waveguide mixers. Also, this method will help to reduce the cost, size, and mass of mixers, which will be important concerns for future focal plane arrays.

3.6 References

[1] M. J. Wengler, D. P. Woody, R. E. Miller, and T. G. Phillips, "A low noise receiver for millimeter and submillimeter wavelengths." *Int. J. Imfrared Millimeter Waves*, vol. 6, pp. 697-706, 1985

[2] J. A. Carpenter, A. D. Smith, E. R. Arambula, L. P. S. Lee, T. Nelson, and L. Yujiri, "100 GHz SIS mixer with improved RF matching," *IEEE Trans. Magn.* vol. 27, pp. 2654-2657, 1991

[3] G. Pance, M. J. Wengler, "Integrated tuning elements for millimeter and submillimeter SIS mixers," *IEEE International Microwave Symposium*, pp.337-340, 1992

[4] J. Zmuidzinas, H. G. LeDuc, J. A. Stern, and S. R. Cypher, "Two-junction tuning circuits for submillimeter SIS mixers," *IEEE Trans. MTT*, vol. 42, pp.698-706, 1994

[5] B. Veidt, K. Kornelsen, J. F. Vaneldik, D. Routledge, and M. J. Brett, "Integrated Josephson effect suppression electromagnets for SIS receivers," *Int. J. Infrared Millimeter Waves*, vol. 16, July, 1995

[6] J. R. Tucker and M. J. Feldman, "Quantum detection at millimeter wavelengths," *Rev. Mod. Phys.*,vol. 57, pp. 1055-1113, 1985

[7] S. Rudner, M. J.Feldman, E. Kollberg, and T. Claeson, "Superconductor-Insulator-Superconductor mixing with arrays at millimeterwave frequencies," *J. Appl. Phys.*, vol. 52 pp. 6366-6376, 1981

[8] T. Van Duzer, C. W. Turner, *Principles of Superconductive Devices and Circuits*, New York: Elsevier, 1981

[9] T. Imamura, T. Shiota, and S. Hasuo, "Fabrication of high quality Nb/AlO$_x$-Al/Nb Josephson junctions: I - Sputtered Nb films for junction electrodes," *IEEE Trans. Applied Superconductivity*, vol. 2, pp.1-14, 1992

[10] J. C Rautio, R. F. Harrington, "An electromagnetic time-harmonic analysis of shielded microstrip circuits," *IEEE Trans. MTT*, vol. 35, pp. 726-730, 1987

[11] *Em User's Manual*, Liverpool, NY: Sonnet Software, Inc., Sept. 1993

[12] J. W. Kooi, M. S. Chan, M. Bin, B. Bumble, H. G. LeDuc, C. K. Walker, and T. G. Phillips, "The development of an 850 GHz waveguide receiver using tuned SIS junctions on 1 μm Si_3N_4 membranes," *Int. J. Infrared Millimeter Waves*, vol. 16, pp. 349-362, 1995

Chapter 4:

Evaluation of a Diagonal Horn Fed with Micromachined Waveguide[†]

4.0 Introduction

One of the obstacles to greater use of submillimetre wavelengths is the difficulty in fabricating the antennas and the transmission line structures. Although it is possible to build horns and hollow metal waveguides for frequencies as high as 2 THz, this can only be attempted for very special applications. Other workers have used photolithography and etching techniques from integrated circuit processing to create new types of radiating structures [1]. This chapter examines an intermediate approach using integrated circuit processing technology to fabricate components similar to those made by standard metal machining. The specific problem looked at is the coupling between a waveguide micromachined in silicon to a diagonal horn machined in metal. This chapter will be organized as follows: silicon micromachined waveguide will be discussed followed by an introduction to diagonal horns. With this background covered, a series of scale model experiments will be described and the chapter will end with a set of conclusions.

4.1 Silicon micromachined waveguide

A hollow rectangular silicon micromachined waveguide suitable for millimetre and submillimetre wavelengths is described Katehi [2] and Yap *et al.*[3]. The finished waveguide (see Figure 4.1) consists of two halves, each composed of a pair of wafers bonded together. Each wafer has a thickness of a quarter wavelength in air at the cutoff frequency for the guide. The half-width waveguide channel has been formed by an anisotropic etch through the inner wafer. The outer wafer provides a sidewall and the surfaces are coated with a metallic conductor.

What makes this structure so attractive is that it will be possible to fabricate structures such as waveguide probes with active devices on thin silicon nitride films [4, 5, 6] suspended across the waveguide channel. This will eliminate the problem of mechanically mounting devices. Another advantage is that where necessary or beneficial, conventionally machined devices, such as sliding noncontacting backshorts, could be used. And finally, there is an advantage in the dimensions of the substrates used. For example, stripline has been suggested as a transmission line for millimetre- and submillimetre-wavelength work [7], but as Figure 4.2 shows, waveguide substrates can be several times thicker than stripline substrates without allowing higher-order modes. This is an important practical advantage since it will allow the use of substrates that are more robust and easier to obtain.

However, there are severe limitations to the application of this type of waveguide, as

---

[†] A version of this chapter has been published: B. Veidt, K. Kornelsen, J. F. Vaneldik, D. Routledge, and M. J. Brett, "Diagonal horn integrated with micromachined waveguide for sub-millimetre applications," *Electronics Letters*, vol. 31, pp. 1307-1309, 1995

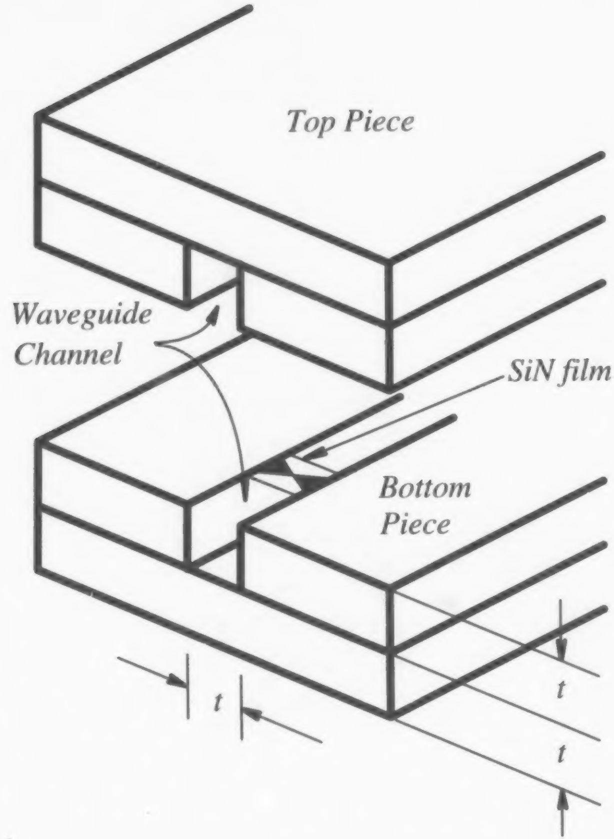

Figure 4.1: Silicon micromachined waveguide. The two halves have been separated to show the interior of the structure.

will be discussed later.

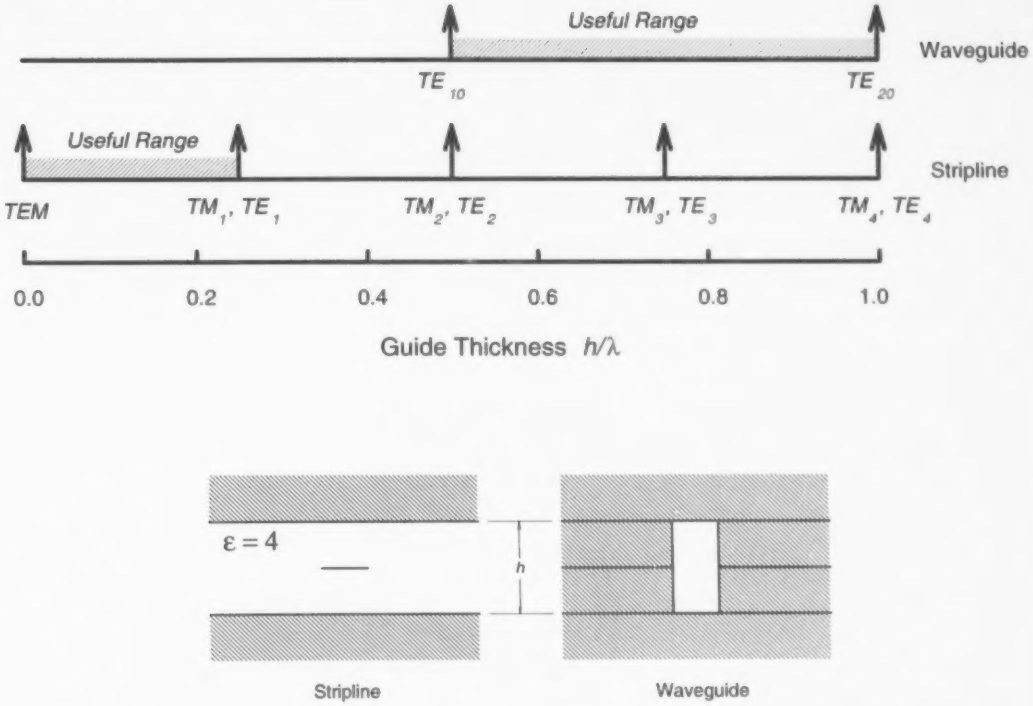

Figure 4.2: Comparison of modes in waveguide and stripline against substrate thickness. (Based on Fig. 26 in Rutledge *et al.*, "Integrated Circuit Antennas," *Infrared and Millimeter Waves*, vol. 10, K. J. Button, ed., p. 38, 1983)

4.1.1 *Etching of silicon*

To understand the fabrication process and some of the problems involved, a review of silicon micromachining is necessary. Petersen [8] has written a classic review that is followed here. Given the deep etches that are needed (between 0.1 and 1 mm), wet etching by immersion in a chemical solution is probably the only means of etching. The two types of etching that are of concern to this project are anisotropic etching that etches along crystal planes, and isotropic etching which etches through the silicon independent of crystal orientation and defined only by a masking layer. Figure 4.3, based on Figure 4.4 of Petersen, illustrates these two types of etches.

Several chemical solutions are available for etching. A mixture of hydrofluoric acid (HF), nitric acid (HNO_3), and acetic acid (CH_3OOH), also called HNA, is often used for isotropic etching. Depending on the concentrations of the constituents, the etch rate can vary between 1 and 40 μm per minute. The etching is also very dependent upon other factors such

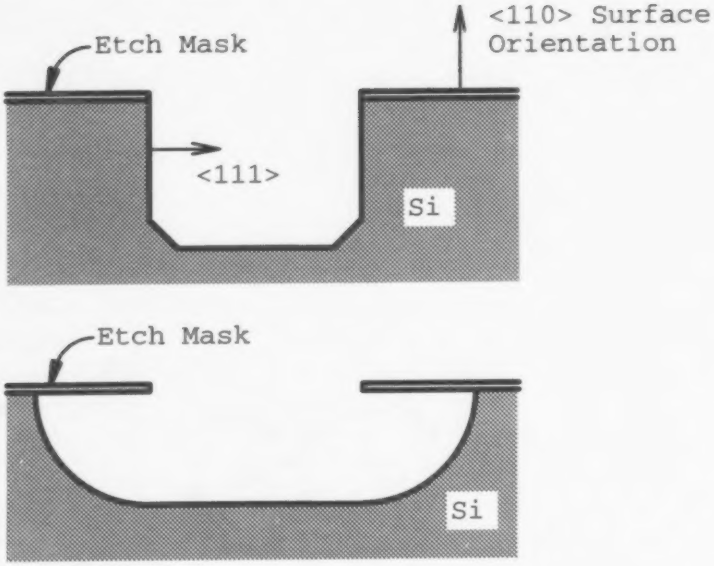

Figure 4.3: An illustration of anisotropic and isotropic etching. The top cross-section shows silicon that has undergone anisotropic etching. Note that the masking layer accurately defined the vertical etch profile. The lower cross-section shows the isotropic etching of silicon. In this case, the silicon below the masking layer has been etched or undercut. Also note that the crystal orientation is important for anisotropic etching , but not for isotropic etching.

as temperature and agitation of the solution. This solution etches the silicon equally well in all directions so that the etch profile is semicircular with a constant radius measured from the edge of the masking layer. The actual shape of the etch profile will also depend upon the agitation of the solution. Silicon nitride (Si_3N_4) and gold make resistant masking layers, but silicon dioxide (SiO_2) is removed and thus can only be used for short etches.

With anisotropic etching the etch rate into the <111> crystal plane is much slower than that into other planes. One etchant is ethylene diamine pyrocatechol (EDP) which has an anisotropic etch rate ratio of 35:1. This solution has the advantage of being compatible with a large variety of masking layers. Unfortunately it has an etch rate of about 1 micron per minute, so etch times will be several hours for wafer thicknesses of interest.

Another anisotropic etchant is potassium hydroxide (KOH). This solution has an even higher anisotropic etch rate ratio of 400:1. However, fewer materials are suitable for use as masking layers: silicon dioxide is slowly etched but silicon nitride is largely untouched.

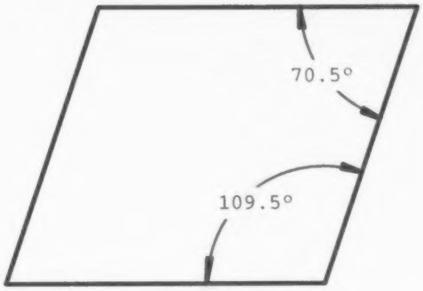

Figure 4.4: The family of <111> planes looking down into a <110> Si wafer. Vertical etches into the silicon will be aligned with these planes.

4.1.2 Problems with micromachined waveguide

A severe limitation is the requirement that the vertical cuts be aligned along the crystal planes, shown in Figure 4.4. Thus arbitrary geometries are not possible; only cuts either parallel to the wafer flat, or at an angle of 109.5° are possible. This allows high quality straight-walled rectangular waveguide to be made, but structures such as bends, tapers, or corrugations will not be possible. Therefore the waveguide must be connected to external waveguide components for practical uses. Unfortunately this re-introduces problems that were to be eliminated by integrated circuit techniques, such as reflections from the waveguide joints and precision machined components.

Arbitrary geometry is possible by using isotropic etching of silicon. The limitation of this technique is that undercutting of the masking layer produces curved walls. However, a two-step process that uses both isotropic and anisotropic etching would make it possible to combine vertical walled waveguide with structures that have curved walls but non-parallel shape. One configuration of interest is a waveguide coupled to flared walls that become part of the walls of a diagonal horn antenna. This is shown in Figure 4.14.

4.2 Diagonal horn antenna

There has been a renewed interest in diagonal horn antennas because they provide a good compromise between performance and ease of fabrication. This horn is simply a flared square waveguide with the E-field excitation at a 45° angle to the walls. Thus it is simple to construct. It also has radiation patterns that are better than simple pyramidal horns but are inferior to corrugated horns. However, corrugated horns are very difficult to build, especially for submillimetre wavelengths. Love [9] provides one of the earliest descriptions of diagonal horns and more recent analyses ([10, 11]) have looked at this antenna as a submillimetre device.

Most of the properties of this horn can be understood based on the Fourier relationship between the antenna aperture fields and the radiation pattern [12] and elementary waveguide theory. The modes in the horn are a set of TE_{10} and TE_{01} modes parallel to the horn walls. The electric field vectors for the two modes are shown in Figure 4.5. In the E plane direction (parallel to the electric field vectors) the amplitude is constant, and in the H plane direction (perpendicular to the E plane) the field amplitude follows a cosinusoidal relation. Individually, each of these modes will have a poor radiation pattern since the field amplitude is constant in one direction, resulting in a pattern with high sidelobes. In the other direction the amplitude distribution is tapered to zero, reducing sidelobes. It also has a narrower effective width, producing a wider main beam width. Obviously what is needed is a field distribution that is similar in the two principle planes, and is also tapered in amplitude. Superimposing the two modes with equal amplitudes produces the vector field plot in Figure 4.6. The new E plane runs from the lower left to the upper right corner. To understand this better, plots have been generated that show the amplitudes of the co-polarized and cross-polarized components. Figure 4.7 shows the co-polarized field amplitude with a 3-D surface plot and with a contour plot. Note how the amplitude is tapered to zero along both lines joining diagonal corners. This results in far-field radiation patterns that are nearly Gaussian and are very similar in the E and H planes. The contour plot shows good radial symmetry, except near the walls. Going across the square waveguide from the centre of one wall to the centre of the opposing wall the field does not taper down to zero. This produces sidelobes in the diagonal or D plane.

Figure 4.8 explains the cross-polarized response. This plot shows the saddle-shaped field amplitude with zero average and equal negative and positive excursions. Viewed on-axis, the negative and positive fields cancel and there should be no cross-polarized response. Viewing the horn off-axis is equivalent to placing a linear phase shift across the aperture, and the negative and positive fields may no longer cancel. The cross-polarization viewed in the E

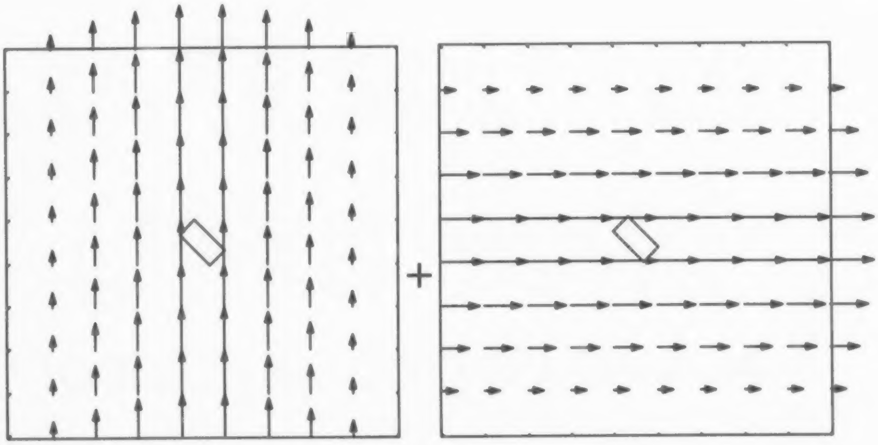

Figure 4.5: Vector plots of the electric fields for the TE_{10} and TE_{01} modes in the diagonal horn. The location of the field point is the tail of the vector. The rectangle represents the waveguide.

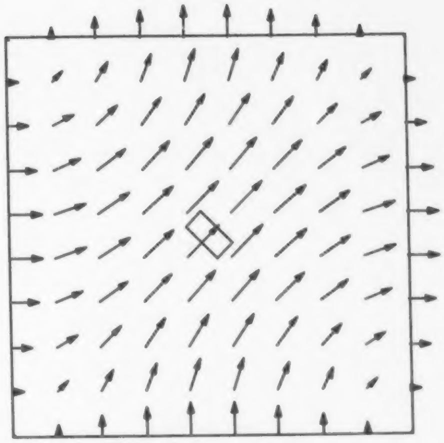

Figure 4.6: Vector field plot of the resultant of the addition of the TE_{10} and TE_{01} modes shown in the previous figure.

or H planes is zero because the saddle is anti-symmetric about a line joining diagonal corners and in the plane of rotation. Thus a point mirrored to the other side of the diagonal line will be paired with a point with equal magnitude and opposite sign, and also equal phase shift, maintaining the cancellation. Unfortunately, in the D plane this pairing of canceling points does not occur, and off-axis cancellation is not maintained.

With real diagonal horns, on-axis cross-polarization is sometimes observed (see Figure 4.8 (d) of Johansson and Whyborn [10]). How can this happen? In Withington and Murphy's analysis they allow the ratio between the amplitudes of the two orthogonal modes to deviate from unity, and they show that this results in a non-zero on-axis cross-polarized response. This can also be seen if Figure 4.8 is replotted with unequal field components. Then, although the saddle shape is preserved, the average across the aperture is not zero and, at a distance, the cross-polarized response is also not zero. Withington and Murphy also show that the co-polarized response is negligibly affected by a mode imbalance.

To feed the horn with rectangular waveguide, Love [9] used a rectangular-to-circular-to-horn transition. This was done because of the similarity between the hybrid mode and TE_{11} in circular waveguide. Johansson and Whyborn [10] have shown that a simple transition consisting of the intersection of the flared horn walls and the rectangular waveguide works well. This suggests that the transition is not critical.

There is interest in fabricating the waveguide in silicon along with circuitry, and then to sandwich this between two metal blocks that have the flared V-grooves, forming the horn antenna. This would have several advantages: the critical components (active device, waveguide probe and waveguide) will be integrated together, less-critical components (the horn itself) can be easily machined in metal, and waveguide joints would be eliminated. The questions that need to be answered are: can a suitable waveguide-to-horn transition be constructed using the restrictions inherent in the silicon micromachining geometry, and will

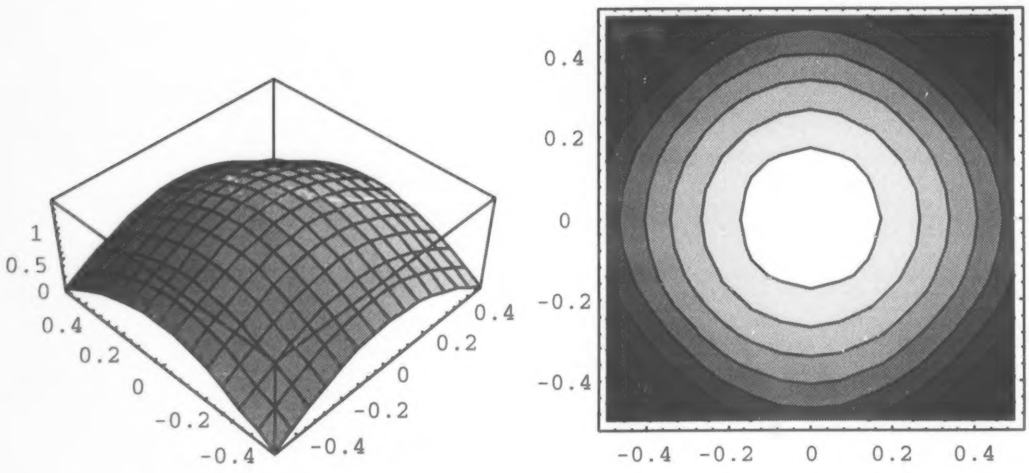

Figure 4.7: Plot of the amplitude of the diagonal horn electric fields aligned in the co-polarized direction.

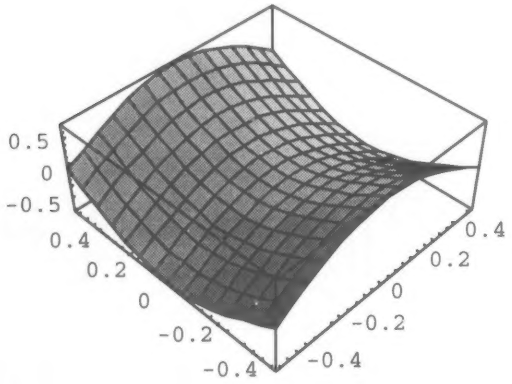

Figure 4.8: Plot of the amplitude of the cross-polarized electric fields in the diagonal horn.

the radiation pattern be affected by truncation of two of the horn corners by the silicon wafers?

4.3 Experiments

Since the electromagnetic structure was to be validated before developing a silicon micromachining process, these experiments used machined aluminum pieces as models for the silicon micromachined wafers. The measurement frequency was 110 GHz, which allowed reasonably accurate models to be constructed. A Schottky diode detector [13] was attached to the backend of the waveguide. The horn dimensions used by Johansson and Whyborn [10] were used: a horn length of 55 mm and a corner-to-corner distance of 14 mm at the aperture. The use of wafers 1.27 mm thick was simulated. To provide a comparison, a standard diagonal horn was constructed in the conventional way (Figure 4.9).

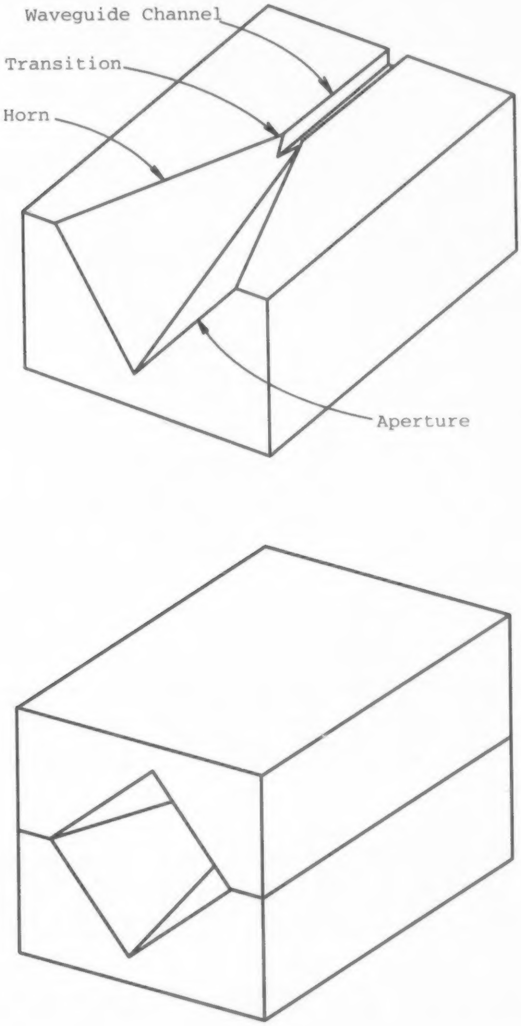

Figure 4.9: Perspective view of diagonal horn used as a comparison standard in experiments. The top view shows one of the two identical pieces; the bottom view shows the assembled horn.

The antenna patterns below were measured on a table-top antenna range with the source and test horns separated by the usual far-field distance of $2D^2/\lambda$. A Gunn oscillator [14] provided a signal with 10 milliwatts of power. A directional coupler placed between the oscillator and the horn allowed the power level to be monitored by a second Schottky diode detector. A variable attenuator preceding the directional coupler was used to adjust the power level. Even though reflections did not appear to be a problem in this test range, sheets of Eccosorb RF absorbing foam [15] were placed on nearby metal surfaces to reduce reflections.

The antenna patterns were measured with the antenna rotated in three planes: the E plane which is parallel to the electric field vector in the waveguide, the H plane which is parallel to the magnetic field in the waveguide and perpendicular to the E plane, and the diagonal or D plane which is at 45° to the E and H planes. In each case, two patterns were measured, one with the source horn positioned with the polarization parallel to the test horn, and a second with the source horn polarization perpendicular to the test horn polarization.

It had been hoped to measure the return loss of the various horns by using a directional coupler to measure the reflected power from the test horn. However, the modeled silicon micromachined pieces were not made accurately enough to align well to the directional coupler flange. Therefore this experiment was not done because reflections from small discontinuities at the joint would mask reflections from the horn.

4.3.1 Standard horn

Figure 4.9 shows the standard diagonal horn. The top view shows the bottom piece, and the lower view shows the complete horn with the top piece added. The top and bottom pieces are identical. This horn was constructed out of aluminum on a milling machine. The waveguide section was cut with a slitting saw to a depth and width of 1.27 mm to match standard WR-10 specifications. The horn section was fabricated by tilting the block by 10.2° and cutting it with an end mill tilted sideways by 45°. The transition between the waveguide and the horn is simply the intersection of the two forms. Not shown are the screw holes for assembling the horn and the holes for mounting the Schottky diode detector to the end of the waveguide.

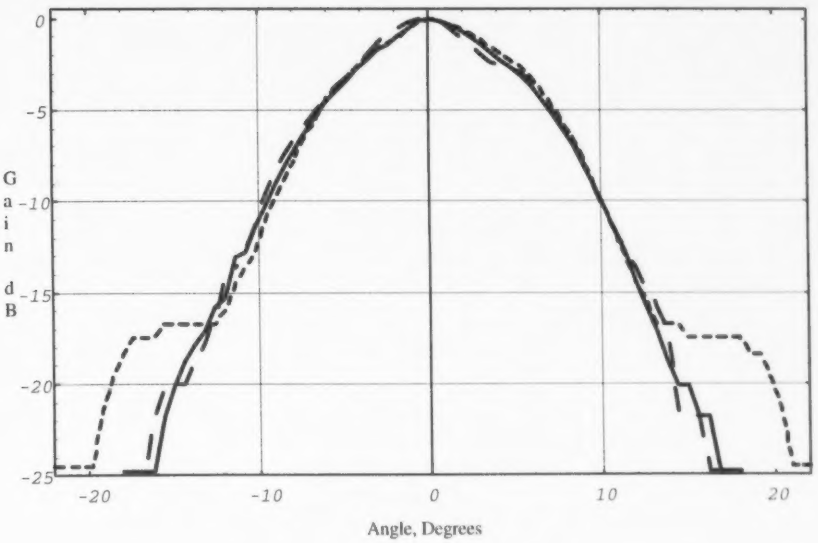

Figure 4.10: Co-polarization radiation patterns for standard diagonal horn. The solid line represents the E plane, the line with long dashes is the H plane, and the line with short dashes is the D plane.

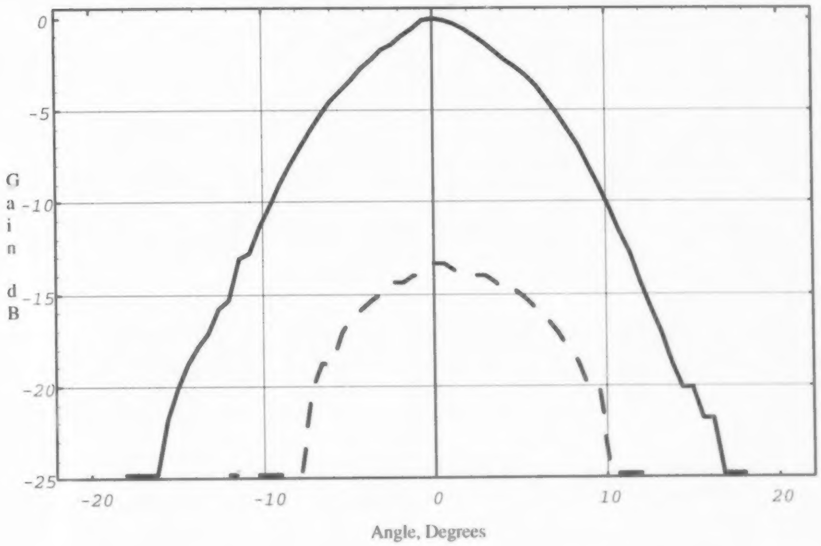

Figure 4.11: E plane cross-polarization radiation pattern (dashed line) plotted with co-polarized pattern (solid line) for standard diagonal horn.

4.3.2 Four-wafer waveguide experiments

The first experiments used inserts based on the standard four-wafer stack waveguide, shown in Figure 4.12. No attempt was made to model the etch undercut that would be present with real silicon wafers. Good radiation patterns were not obtained with this configuration. The probable cause of this failure is the step in waveguide width at the waveguide to horn transition. This step occurs because the outer wafers must be removed in the horn. This can be seen near the apex of the V cut into the wafers in Figure 4.12. The waveguide width is equal to the height of the two inner wafers. A large step like this will launch unwanted higher order modes into the horn.

Note that in Figure 4.12 and in subsequent drawings of antennas, the inserts are drawn as though they are constructed with silicon wafers, even though in the model they were made of aluminum and were made of fewer layers.

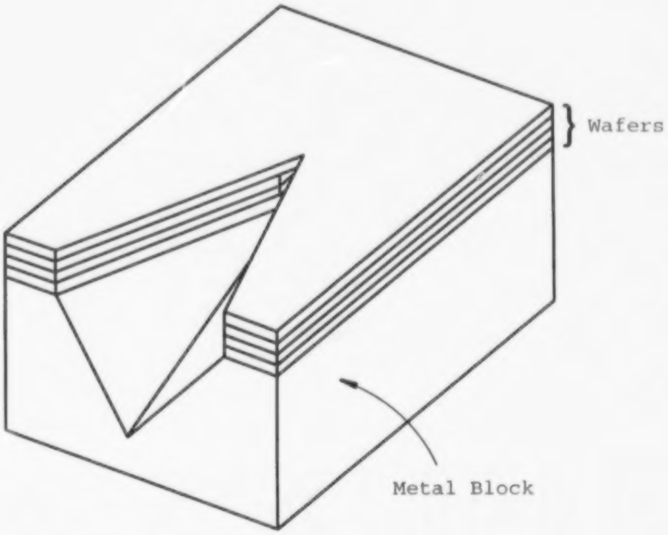

Figure 4.12: Diagonal horn using micromachined waveguide based on a four wafer stack The top metal block has been removed for clarity.

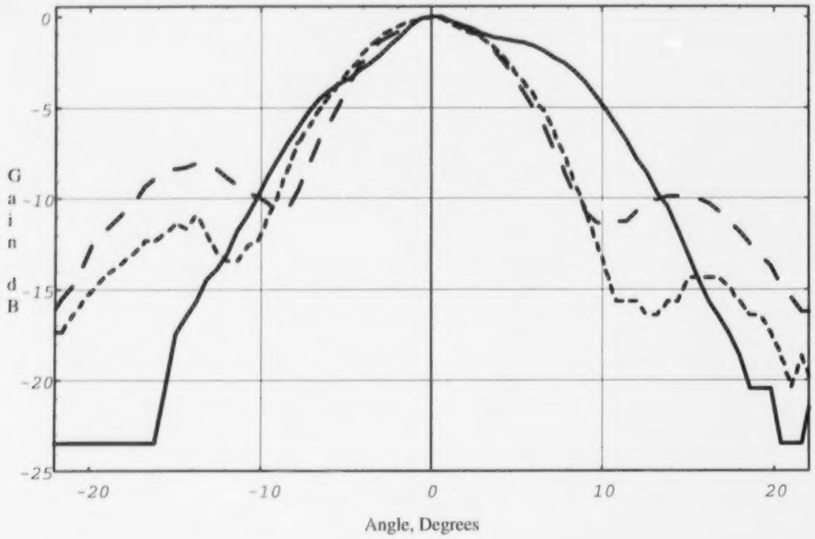

Figure 4.13: E plane (solid line), H plane (long dashes), and D plane (short dashes) radiation patterns for diagonal horn shown in Figure 4.12.

4.3.3 Modified waveguide structure

These poor results led us to produce a modified waveguide structure. Instead of using four wafers across the entire device, only two were used near the horn. In this configuration the metal blocks provided the waveguide sidewalls. This change eliminated the step at the start of the horn flare. For some simple systems which have the far end of the waveguide closed, only two wafers could be used, as shown in Figure 4.14. Note that the metal block is simpler than the standard horn since the waveguide groove is not required.

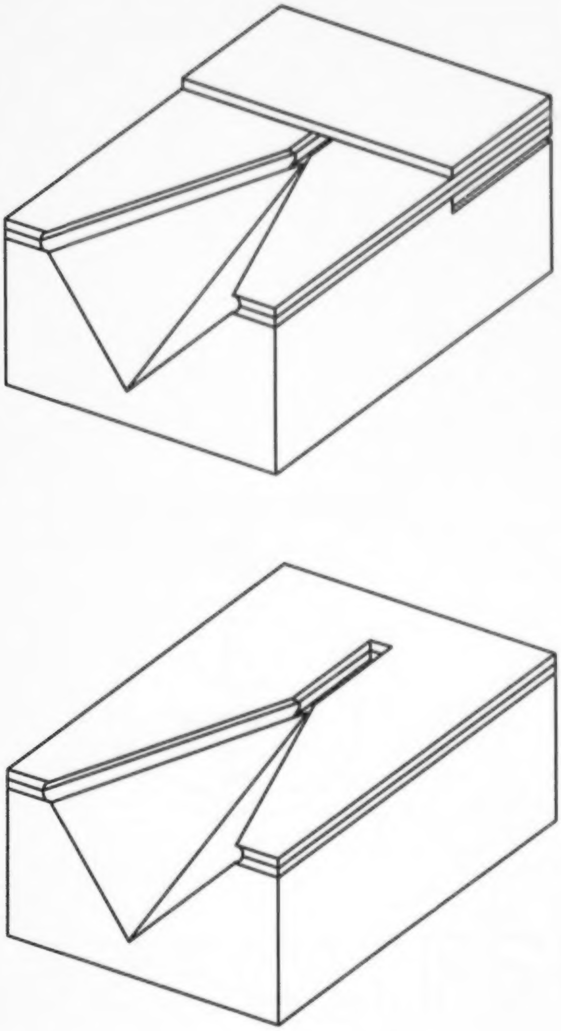

Figure 4.14: Diagonal horns with the modified silicon micromachined waveguide. The top drawing shows a system using a four wafer stack, the lower drawing shows a system based on a two layer stack. The top metal blocks have been removed for clarity.

4.3.4 Flat-sided inserts

Before cutting the groove simulating etch undercut into the flared walls of the model pieces, the model was assembled and the antenna pattern was measured (see Figure 4.15). The reason for doing this was to establish what the radiation pattern looks like for several different etching conditions since the isotropic etch is somewhat variable. This case provided information on wafers with minimal undercut.

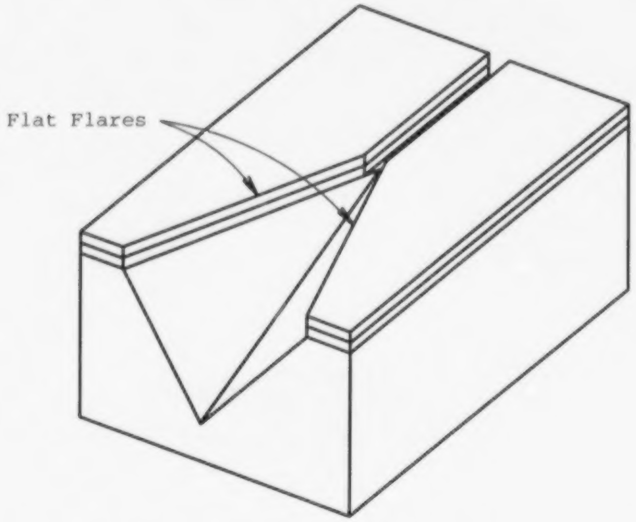

Figure 4.15: Horn with inserts that have flat flare sides representing minimal isotropic undercut. The top metal block has been removed for clarity.

The radiation patterns, Figure 4.16 and 4.17, are very similar to standard horn patterns. The three planes are all within a decibel of each other to the -13 dB level. The cross polarization response is interesting. The E and H plane cross polarized response was below the -24 dB level and thus was not shown here. In the D plane, the on-axis cross polarization was not visible, while the sidelobes at ±11° remained. Withington and Murphy show that the on axis cross polarization should not exist, but appears if the orthogonal TE_{10} modes in the horn have unequal amplitudes. Johansson and Whyborn also observe the excess cross polarization. But why was the on-axis cross-polarization present in the standard horn but not in this one? One possibility is that the more gradual transition from the waveguide to the horn is more sensitive to machining inaccuracies. If the V-groove is displaced from the centreline of the waveguide, the division of power between the two orthogonal modes will not be equal. This is apparently not a problem with the blunt transition in this design. This hypothesis will be tested in further iterations of this horn design.

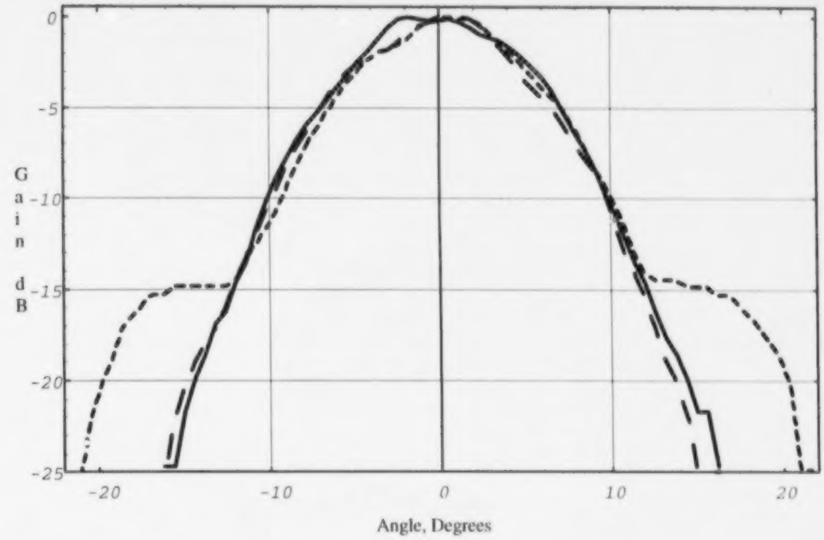

Figure 4.16: Co-polarized radiation pattern of diagonal horn with modified micromachined waveguide. The flares have flat walls. The solid line is E plane, long dashed line is H plane, and short dashed line is D plane.

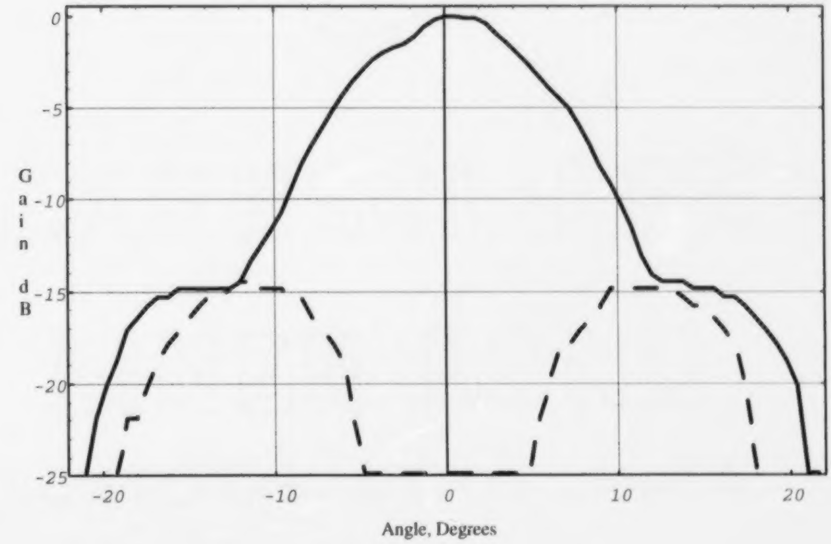

Figure 4.17: Co-polarized (solid line) and cross-polarized (dashed line) radiation patterns in the D plane of diagonal horn with modified micromachined waveguide. The flares have flat walls.

4.3.5 *Inserts with curved walls*

The next step was to mill half-circular grooves into the flared walls to simulate etch undercut. This is shown in Figure 4.18. Again, the co-polarized patterns in the E, H, and D planes (Figure 4.19) are very similar to those of the standard horn. However, milling the half-circular grooves into the flare walls degraded the on-axis cross-polarization response. Figure 4.20 shows the D plane cross-polarized pattern, which now has some response between the two sidelobes. This agrees with an earlier hypothesis on the origin of the on-axis cross-polarized response, since the intersection of the waveguide wall and the half-cylindrical flare wall is sensitive to lateral alignment.

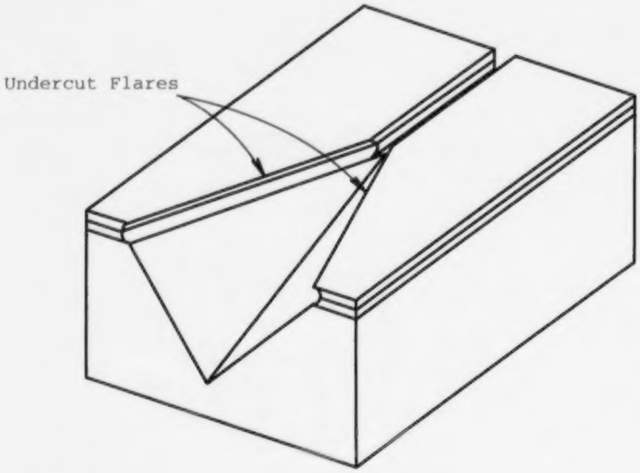

Figure 4.18: Diagonal horn with inserts simulating a constant radius undercut along the flare.

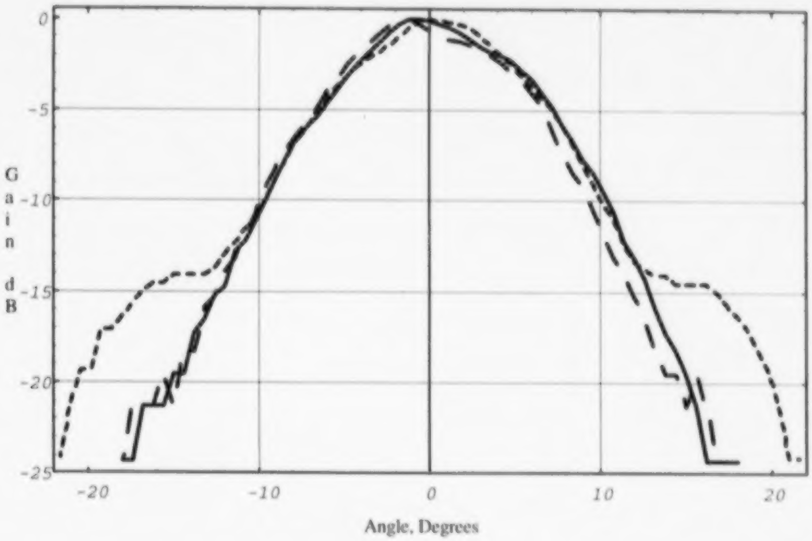

Figure 4.19: Co-polarized radiation patterns for horn with inserts simulating a constant radius undercut along the horn flare. The solid line is E plane, long dashed line is H plane, and short dashed line is D plane.

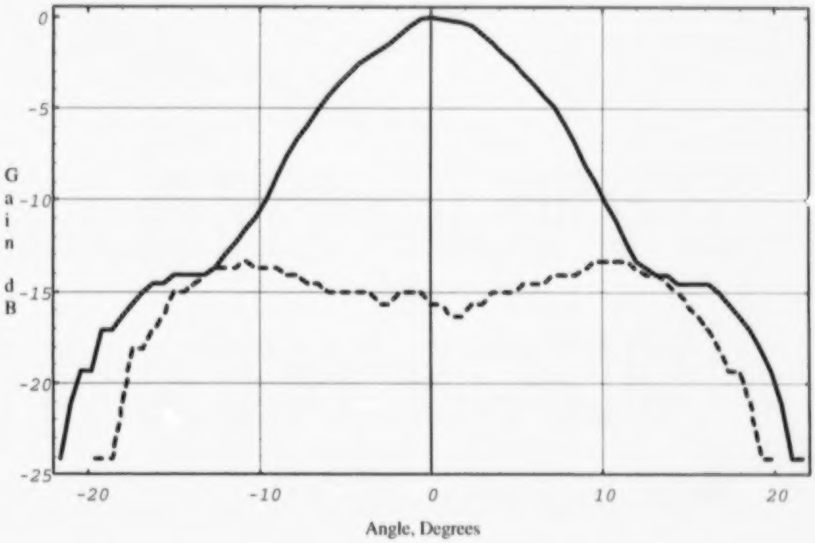

Figure 4.20: D plane radiation patterns of horn with inserts simulating constant radius undercut. Co-polarized (solid line) and cross-polarized (dashed line) shown.

4.3.6 Proper modeling of undercut

The previous model of undercut micromachined wafers was not completely correct. The waveguide-to-horn transition is not a simple intersection of a cylindrical walled flare and the straight-walled groove. The intersection is more complicated because the narrow end of the isotropic etch does not come to a point, but is itself a curve with the undercut radius. Figure 4.21 shows a view down onto an etched wafer. Thus the transition is actually blunter than previously modeled. The overall antenna is otherwise the same as shown in Figure 4.18.

Once again, the co-polarized response (Figure 4.22) is similar to that of the standard horn. The on-axis cross-polarized response has also dropped below -24 dB, as shown in Figure 4.23. This again confirms the hypothesis on the origin of the on-axis cross-polarized response.

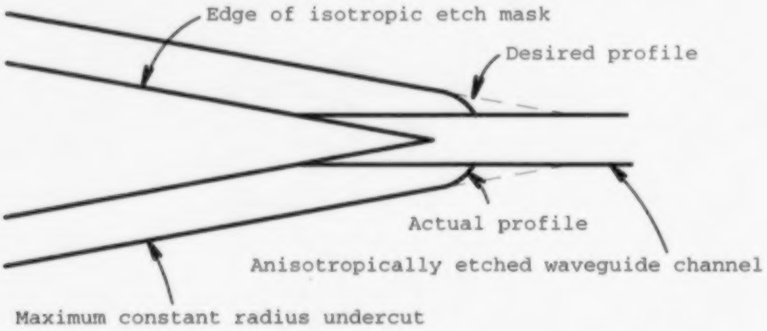
Edge of isotropic etch mask
Desired profile
Actual profile
Anisotropically etched waveguide channel
Maximum constant radius undercut

Figure 4.21: Geometry of the intersection of the isotropic and anisotropic etches in the transition from waveguide to horn. The view is looking onto the wafer.

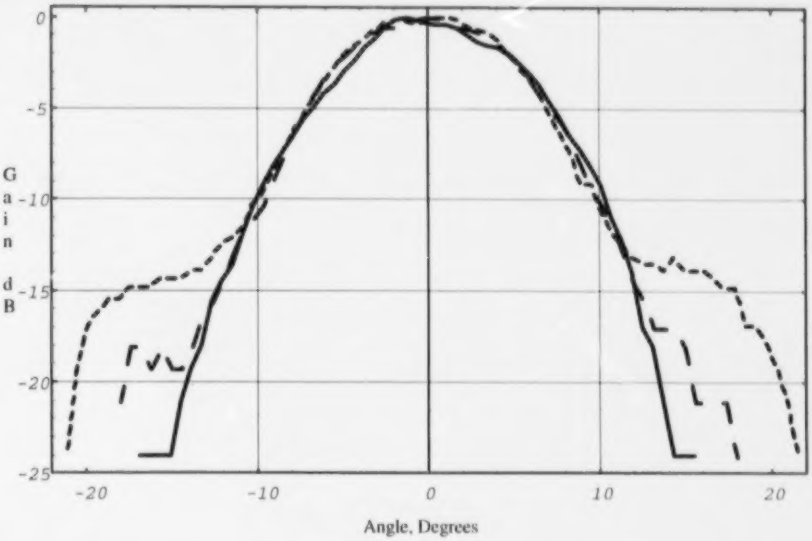

Figure 4.22: Co-polarized radiation patterns of the diagonal horn with the undercut properly modeled. The solid line is E plane, long dashed line is H plane, and short dashed line is D plane.

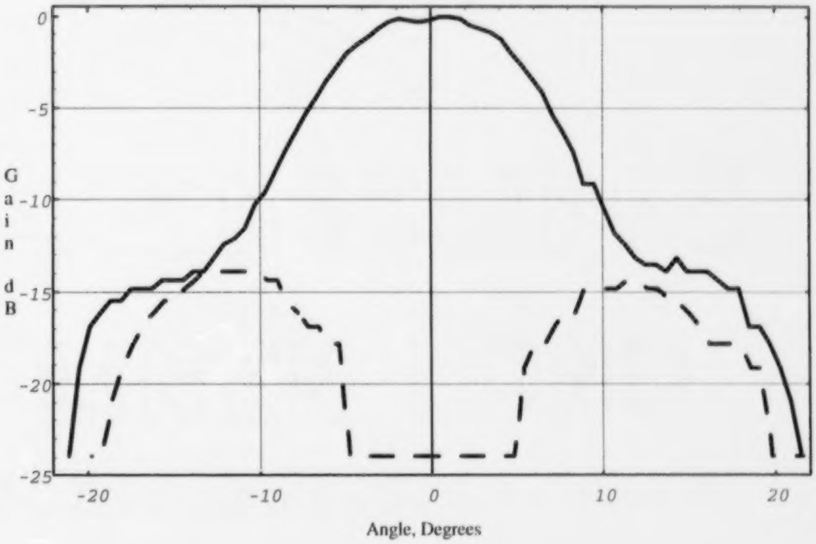

Figure 4.23: Co-polarized (solid line) and cross-polarized (dashed line) radiation patterns for the horn with undercut properly modeled.

4.4 Discussion

4.4.1 Conclusions

This work has demonstrated the feasibility of using silicon micromachined waveguide with a simple diagonal horn structure. The radiation patterns were very similar to those obtained with a conventional diagonal horn. However, to get good patterns the micromachined waveguide was modified by eliminating the outer wafers near the horn.

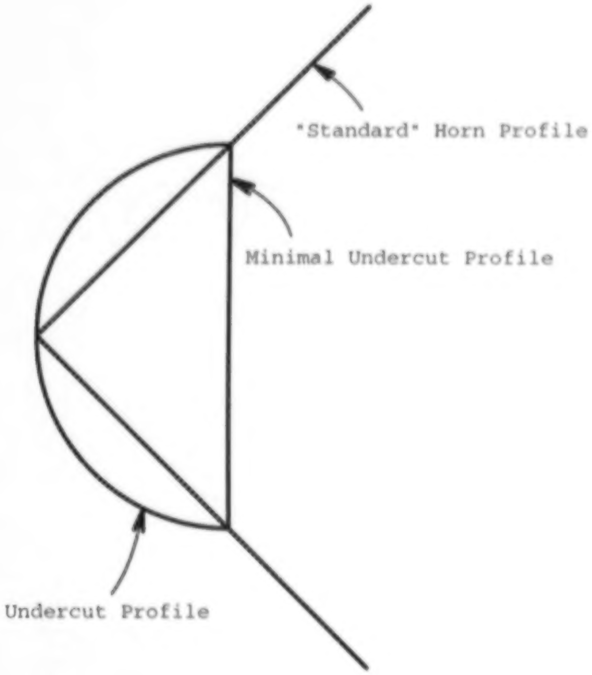

Figure 4.24: A section through the diagonal horn showing the profiles of the standard horn, flat sided flare (minimal undercut etch), and undercut flare, all superimposed.

It is interesting how insensitive the horn is to the cross-sectional profile of the silicon inserts. As Figure 4.24 shows, a large variation in the insert cross section has been tested. This is a promising result. Although anisotropic etches are somewhat variable, this will not have a harmful effect on the performance of the horn.

The cross-polarized results are interesting. A significant reduction in the on-axis cross-polarization response was seen when the flared section either had flat walls or had the undercut properly modeled. This work shows that this is because transitions that have a "blunt" intersection with the waveguide rather than a long and gradual intersection are less sensitive to machining errors that upset the mode balance in the horn. There are two implications of this result. First, the parameters of the isotropic etch (such as etchant agitation) should be adjusted to reduce sidewall curvature. Second, this result could lead to an improved waveguide-to-horn transition for molded or electroformed diagonal horns for longer wavelengths.

However, these cross-polarization results should be cautiously extrapolated to a silicon micromachined structure. In the model, two layers of silicon were modeled with a single piece of aluminum. Thus perfect symmetry and alignment were assured for the model, but this will not be the case for a silicon implementation. The mode balance may not be perfect, and cross-polarization may be seen where it is not present with the model.

4.4.2 Recommendations for future work

Since the silicon micromachined waveguide coupled to a diagonal horn works as an electromagnetic structure, it is worthwhile to spend some time considering future work. The obvious next step is to make the antenna and waveguide out of silicon. The proposed two step etching process should be feasible. The first etching step would be the isotropic etch to define the horn flare, followed by the anisotropic etch to form the waveguide channel. Since the lithography will take place from opposite sides of the wafer, the anisotropic etch lithography will not have to be done on curved isotropically etched surfaces. Thus the two etches will be compatible with each other

Once the details of the etching have been worked out, an actual millimetre-wave system should be constructed. These experiments were performed at 110 GHz and used large area inserts - 25 mm x 66 mm. It may be advantageous to work at a higher frequency where the area of each insert would be smaller and more could be fabricated on a wafer. For example, a 345 GHz source is available. Therefore, dimensions could be reduced by a factor of 3. Another issue is the detector technology to use. Superconducting tunnel junctions are one possibility, but they are difficult to fabricate and must be cooled to 4K. Although less sensitive, bismuth bolometers are easy to fabricate, are easier to match to antennas since they are purely resistive, and can be calibrated with DC measurements [6].

With a fully integrated system, measurements in addition to antenna patterns will be possible. For example, directional coupler could be integrated on the wafer for return loss measurements. At that point it will become possible to go back and modify the processing steps to optimize the electromagnetic performance of the millimetre-wave system. For example, the present design for the waveguide-to-horn transition probably has a low return loss. This could be improved by making the transition more gradual, by modifying the shape of the isotropic etch mask.

4.5 References

[1] G. M. Rebeiz, "Millimeter-wave and terahertz integrated circuit antennas," *Proc. IEEE*, vol. 80, pp.1748-1770, 1992

[2] L. P. B. Katehi, "Novel transmission lines for the submillimeter-wave region," *Proc. IEEE*, vol. 80, pp. 1771-1787, 1992

[3] M. Yap, Y.-C. Tai, W. R. McGrath, and C. Walker, "Silicon micromachined waveguides for millimeter and submillimeter wavelengths", *Proc. Third International Symposium on Space Terahertz Technology*, pp. 316-322, 1992

[4] E. Garcia, B. R. Jacobson, Q. Hu, "Fabrication of high-quality superconductor-insulator-superconductor junctions on thin SiN membranes," *Appl. Phys. Lett.*, vol. 63, pp. 1002-1004, 1993

[5] J. W. Kooi, M. S. Chan, M. Bin, B. Bumble, H. G. LeDuc, C. K. Walker, and T. G. Phillips, "The development of an 850 GHz waveguide receiver using tuned SIS junctions on 1 μm Si_3N_4 membranes," *Int. J. Infrared Millimeter Waves*, vol. 16, pp. 349-362, 1995

[6] C. C. Ling, G. M. Rebeiz, "A wide-band monolithic quasi-optical power meter for millimeter- and submillimeter-wave applications," *IEEE Trans. Microwave Theory Tech.*, vol. 39, pp. 1257-1261, 1991

[7] T. H. Legg, "Quasi-optical stripline devices," *United States Patent*, Number 5,117,237, May 26, 1992

[8] K. E. Petersen, "Silicon as a mechanical material," *Proc. IEEE*, vol. 70, pp. 420-457, 1982

[9] A. W. Love, "The diagonal horn antenna," *Microwave Journal*, vol. 5, pp. 117-122, 1962

[10] J. F. Johansson, N. D. Whyborn, "The diagonal horn as a sub-millimeter wave antenna," *IEEE Trans. Microwave Theory Tech.*, vol. 40, pp. 795-800, 1992

[11] S. Withington, J. A. Murphy, "Analysis of diagonal horns through Gaussian-Hermite modes," *IEEE Trans. Antennas Propagation*, vol. 40, pp. 198-206, 1992

[12] R. N. Bracewell, *The Fourier Transform and its Applications*, New York: McGraw-Hill, Chapter 13, 1978

[13] Model WD, Pacific Millimeter Products, 64 Lookout Mountain Cir. Golden, CO 80401, USA

[14] J. E. Carlstrom, R. L. Plambeck, D. D. Thorton, "A continuously tunable 65 - 115-GHz Gunn oscillator," *IEEE Trans. Microwave Theory Tech.*, vol. 33, pp. 610-619, 1985

[15] Emerson and Cuming, Inc., 869 Washington St., Canton, MA 02021

Chapter 5:

Conclusions

The objective of this thesis was to develop new techniques that would enhance millimetre- and submillimetre-wave receivers for radio astronomy. Three innovations were tested; of these techniques, two were successful and one was not.

Chapter 2 described an attempt to make a mixer with an electrically-adjustable tuning element. That work was not successful because of the limited sharpness of practically realizable superconducting devices. However, that work demonstrated a method for precise construction of a waveguide mixer block and the computer-aided design of the waveguide probe. It also produced a receiver within a factor of 10 of the theoretical sensitivity limit.

Chapter 3 described the integration of a Josephson effect suppression magnet onto the mixer integrated circuit. From theory, the design relations were derived and confirmed with an experiment. This contribution is important because it has added another component to the mixer integrated circuit that already contains the active device, matching network, and antenna. This technique should aid in the development of focal plane array receivers because it will reduce the volume and mass required for each mixer element by eliminating external superconducting electromagnets and flux concentrators.

Chapter 4 described a test of the feasibility of combining silicon micromachined waveguide with a diagonal horn antenna. Micromachined waveguide has been developed as a means of fabricating high quality waveguide by integrated circuit techniques. Unfortunately there did not seem to be a way to integrate other components with the waveguide, and it appeared that flanges would be needed. This chapter shows how the structure of the waveguide could be modified to allow it to be easily coupled to a diagonal horn. This work is important because it has shown another way to build integrated systems at millimetre- and submillimetre-wavelengths. This work has demonstrated some of the problems with diagonal horns and has shown one method to reduce the undesired characteristics.

Appendix:

An Outline of Superconducting Electronics[†]

A.0 Introduction

The purpose of this appendix is to provide a background in superconductivity with an emphasis on applications that are important to RF engineering at millimetre wavelengths, namely active devices and superconducting transmission lines. The motivation for including this appendix is that such information is not a common component in electrical engineering curricula. Keeping this material separate also helps smooth the flow of the chapters in this thesis.

In this appendix the applicable theory will be reviewed and a set of tools will be developed to help understand the theory and to be used for design. The first section will cover Bardeen-Cooper-Schrieffer (BCS) theory, with emphasis on why superconductivity works, and on quasiparticle excitations. Excitations are critical for understanding the next section which covers superconducting tunnel diodes. That section will show how to obtain the fundamental circuit parameters of superconducting tunnel diodes for the design of sensitive mixers. Excitations are also important in the understanding of superconducting transmission lines. Here a phenomenological theory is developed from the observed bulk properties of superconductors and Maxwell's Equations. The final section covers superconducting circuits that can be used to measure the properties of transmission lines.

Several topics are beyond the scope of this work. Superconducting antennas will not be covered since these are usually electrically small, which is not the case for millimetre antennas. High transition temperature (high T_c) superconductors will be ignored since "conventional" superconductors are still the dominant material for electronic applications, and because much of the theory presented here will also apply to the new materials when they become widely used. Also ignored is the behavior of superconductors in the presence of strong magnetic fields.

A.1.0 Microscopic superconductivity

The purpose of this section is to help to understand the mechanism of superconductivity. Although later sections will show how some problems are solved successfully without knowing how superconductivity works, tunneling and other problems require an understanding of what happens to electrons within superconductors. This discussion will begin by examining conduction in normal metals and then expand upon that knowledge to include superconductors. In many ways, the theme of this section is to study paired superconducting electrons so that the properties of *unpaired* electrons can be known, since it is unpaired electrons that are responsible for quasiparticle tunnel diodes and controlling kinetic inductance.

[†] This material was originally presented to meet the requirements of a directed-study course EE602 (B2): Superconducting Electronics in April, 1993.

A.1.1 Conduction in normal metals[†]

Basic solid state physics will be discussed here to lay out the concepts and terminology needed to understand electrical conduction in metals.

First, consider the plot in Figure A1 that shows the occupancy for states of different energies. Beginning at low energies, the states are completely filled. This is because electrons are fermions and by the Pauli exclusion principle, there is a limit to the number in one state. The dotted line shows the probability distribution when the temperature is at absolute zero: the probability remains at one up to the Fermi energy (ε_F) and then drops to zero. This rectangular ground state distribution has the high energy edge smeared out by electron excitations at temperatures above absolute zero. Note that these excitations from the ground state can have arbitrarily small energies above the Fermi energy.

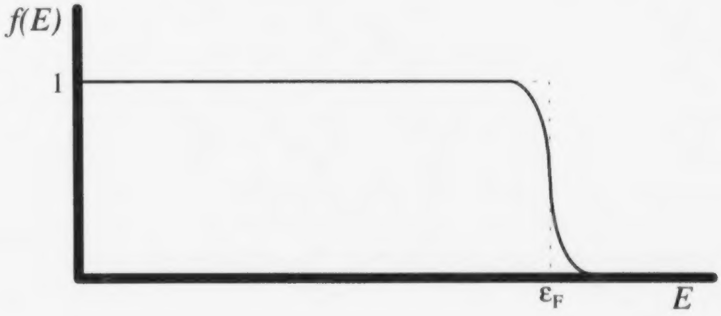

Figure A.1: Probability of occupancy versus electron energy.

Another useful tool in visualizing the properties of electrons is a Fermi surface, which is a three-dimensional surface in **k** (momentum) space for values of **k** where the energy is equal to the Fermi energy. Since conduction electrons behave similarly to free particles, it is reasonable to assume that they can be described by a plane wave. Using Schrödinger's equation, it can be shown that the energy is proportional to the momentum squared, and that there is no direction dependence. Thus in this case the Fermi surface is a sphere (real Fermi surfaces may be more complex). The states within ~*kT* (*k* is Boltzmann's constant) of the surface are the ones important for electrical conduction. States deeper in the sphere are completely filled and are essentially inaccessible.

Excitations in a normal conductor will be considered now. Figure A.2 shows the probability of occupancy as a function of momentum. Also shown are a hole excitation and an electron excitation. Every excitation in a normal metal must produce both a hole and an electron since the electron must come from somewhere.

[†] This section follows Chapter 1 of Van Duzer and Turner, [1], with occasional material from Blakemore, [2].

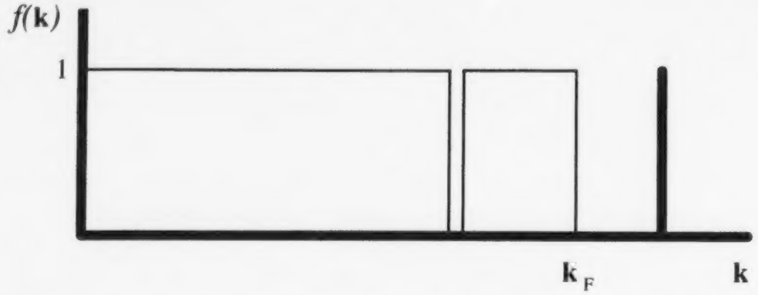

Figure A.2 Hole and electron excitations in a normal metal.

Figure A.3 shows a representation of excitation energy as a function of momentum. The top curve is parabolic due to the relationship between energy and momentum. The total energy to excite an electron at ε_e from ε_h is $\varepsilon_e - \varepsilon_h$. The second plot is the first replotted using the function $E = |\varepsilon - \varepsilon_F|$, or simply taking the part of the curve below ε_F and folding it upwards. On this graph, the excitation energy is just the sum of the electron energy, E_e, and the hole energy, E_h. Note that there is no energy gap between the excitation curve and the E=0 axis; a similar curve for superconductors has a gap.

The remaining topic to cover for a normal conductor is the electron-phonon interaction. Such interactions are important since they not only result in resistance in normal materials, but also result in zero resistance for superconductors. When an electron is scattered by a phonon, both momentum and energy are conserved. Since essentially no unoccupied electron states exist below the Fermi surface, the momentum of a scattered electron must be close to the Fermi surface. The situation is somewhat different for phonons since the occupancy of states is highly temperature dependent while for electrons only very small changes in the occupied states occur as the temperature is increased. At low temperatures only low phonon momentum states are occupied, and thus only small changes in electron momenta are possible. With high temperatures the phonon momenta become comparable to electron momenta so large angle deflections are possible.

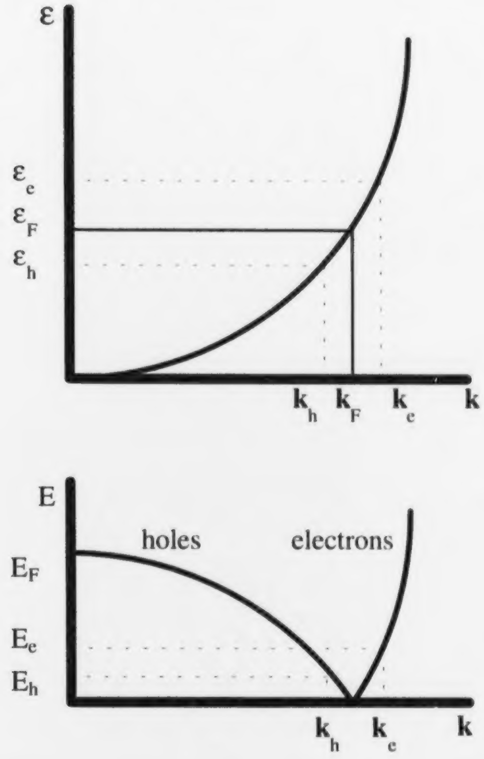

Figure A.3: Two representations of electron and hole excitations in a normal conductor.

A.1.2 BCS superconductivity[†]

The Bardeen-Cooper-Schrieffer (BCS) theory of superconductivity is abstract and the mathematics are complex. It is beyond the scope of this paper to cover the derivation of this theory in any depth. Instead results will be presented that will be useful later on.

The fundamental phenomenon that makes superconductivity possible is the pairing of electrons at low temperatures. Pairing occurs since the total energy of the system is minimized. Although free electrons will repel each other due to Coulomb's force, in a superconductor the electrons interact with the lattice through the exchange of phonons and a net attractive force is produced. A simple picture to describe what happens can be made by considering an electron (negative particle) moving through a lattice of positively charged nuclei. The electron will attract each nucleus slightly as it goes by, and after it has passed, the nucleus will spring back to its original position. If the nucleus overshoots its original position, a second following electron will feel an *attractive* force since the positively charged nucleus is closer than it would have been if the first electron had not gone past first. Thus the two electrons have communicated by way of a lattice vibration (a phonon) and the force between them can be attractive under the right circumstances.

[†] This section follows chapter 2 of Van Duzer and Turner [1], which is based upon Bardeen, Cooper, and Schrieffer [3]. Cooper [4] has also written a readable introduction to superconductivity.

The isotope effect was used as experimental evidence to come to this conclusion. It was found that the transition temperatures of different isotopes of a superconductor follow the law:

$$T_c \propto 1/\sqrt{M} \tag{A.1}$$

where M is the mass of the ion. Since the electron configuration is the same for different isotopes of the same element, this meant that the lattice itself is involved in superconductivity. More evidence of the importance of electron-lattice interactions is that very good normal conductors like silver, gold, and copper do not superconduct. The high conductivity of these materials is due to the very small interaction between the lattice and the electrons, which is too small to allow electron pairing to occur.

There is more to be said about this superconducting ground state. With zero current flow, the pairing occurs between electrons of opposite spin and opposite momentum. For a non-zero current, the momenta have a non-zero sum. Phase-locking also occurs between pairs so that the ensemble can be described by a single wave function.

Since the energy of the system is reduced with each pair formed, a finite energy is required to break the pair. This energy is called the gap energy and is represented by the symbol Δ. A typical value for Δ is 1.5 meV for niobium. It is this energy that gives superconductivity its properties of persistence; perturbations to the system that are below the pair-breaking energy cannot cause a dissipation of energy. A crude analogy can be made by representing the Fermi sphere of a normal conductor by a glass of water filled to the brim, and a superconductor by a glass of water filled to a small distance below the brim. Any motion will cause the first glass to lose water, whereas the second glass will only lose water with more violent movements. Likewise the Fermi sphere of a superconductor has pairing occurring at the surface and this pairing sets up a buffer of height Δ that prevents excitations of arbitrarily small energy.

Thus it can be seen that the only excitations that are permitted in a superconductor are those that split a Cooper pair. Like excitations in a normal metal, excitations in a superconductor involve the creation of a hole (unoccupied state) and a new surely occupied state. This is shown schematically on Figure A.4 where the probability of occupancy is plotted against momentum. Since the superconducting ground state consists of pairs of electrons with equal and opposite momentum, this plot has both negative and positive wings. The first plot has an electron added well below the Fermi level ($\mathbf{k}_F$) at $\mathbf{k}_1$, which already has an occupation probability of one, so there is no change in the occupation. However, a hole is clearly excited at $-\mathbf{k}_1$ and this excitation is called a quasihole with the loss of one electron.

The next graph shows an excitation at $\mathbf{k}_2$. Since this state is empty, an electron can be placed here. At $-\mathbf{k}_2$ the state is empty and an electron cannot be removed. Thus there is a net gain of one electron and the excitation is called a quasielectron. Excitations nearer to the Fermi level where occupation probabilities are between zero and one will clearly involve both the loss and gain of an electron. Since the probabilities are fractional, the net excitation will involve the loss or gain of a fraction of an electron.

Note how two difficulties have arisen: electrons have been created or destroyed, and in fractional numbers. These problems are avoided since the breaking of each Cooper pair involves two excitations. It can be shown that for **k'** and **k''** which are spaced equally on either side of $\mathbf{k}_F$, the probabilities of these two momenta are related by

$$v_{\mathbf{k}''}^{2} = 1 - v_{\mathbf{k}'}^{2}. \qquad \text{(A.2)}$$

It is now easy to show that the quasielectron created from one excitation is canceled by the quasihole of the other excitation, so that the net gain in charge is always zero. As a result, the energy required to break a pair is 2Δ.

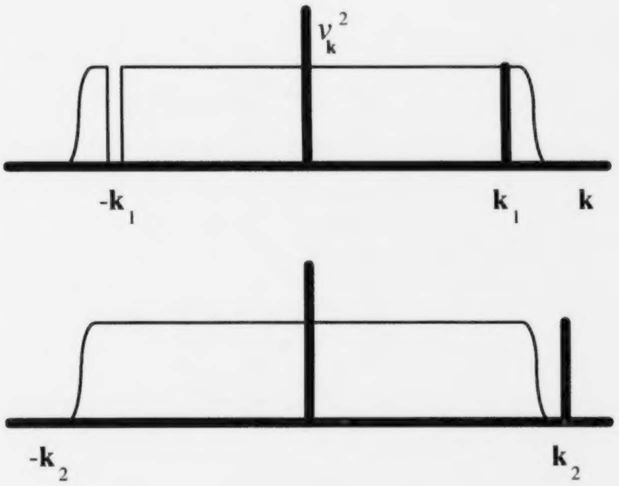

Figure A.4: Excitations from the superconducting ground state.

To prevent possible confusion, several points about quasiparticles should be noted. These excitations are very much like electrons - they can be scattered - but they cannot be within Δ of the Fermi surface and they have a finite lifetime. Unlike Cooper pairs, there is no phase correlation between particles. Between 0 and T_c a superconductor has populations of both Cooper pairs and quasiparticles. As T_c is approached, thermal energy breaks more pairs, until, at T_c, all pairs are broken and all electrons are normal electrons. Although much of the theory and terminology used is shared with semiconductor solid state physics, the term “hole” has a different meaning in superconductivity: it simply implies an unoccupied state and does not have the attributes of a hole in a semiconductor such as an effective mass.

The energy of excitations can be plotted against momentum, as in Figure A.5. Note again the minimum excitation energy Δ. In this plot the ground state is along the horizontal axis.

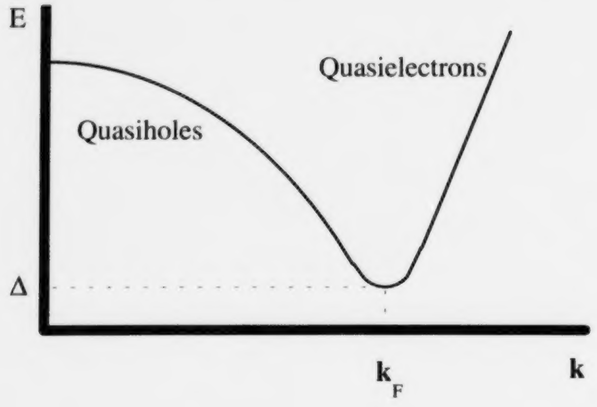

Figure A.5: Energies of quasiparticle excitations

One interesting property of quasiparticles is the lifetime before recombining with another quasiparticle to form a Cooper pair. Kaplan *et al.* [5] have studied this and the results will be given here. For niobium they calculate that for quasiparticles with excitation energies ~ Δ and T ~ 5.5K, the recombination time is ~ $6\text{x}10^{-10}$ seconds. Later it will be shown how the injection of quasiparticles will modify the inductance of a transmission line. Knowing how long this nonequilibrium quasiparticle injection survives will be important in determining the number of injection points along the line.

Before moving onto devices, the density of states for excitations must be explained. For most purposes the density of excitation states can be written as

$$N_s(E) = \frac{N_n(0)E}{\sqrt{E^2 - \Delta^2}} \tag{A.3}$$

for $|E| > \Delta$ and zero otherwise. This shows that at energies far from Δ, the density of states approaches that of a normal conductor. Figure A.6 shows the density of states for a superconductor in a semiconductor representation. In this figure, energy increases in both directions away from the origin and quasihole states are assumed to be full. The superconducting ground state is a horizontal line through the horizontal axis. This diagram is an important tool for understanding tunneling.

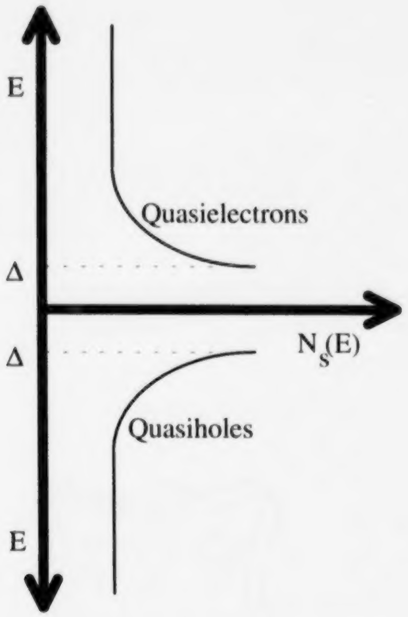

Figure A.6: Density of quasiparticle states.

A.2.0 Quasiparticle tunnel junctions

Now that a foundation of theory has been laid, active devices called superconducting tunnel junctions can be understood. This discussion will be in two parts. The first will explain tunneling and the DC properties of the devices, and the second part will examine the RF properties.

First, terminology will be explained. Superconducting tunnel junctions are often identified by the physical construction, such as superconductor-insulator-superconductor (SIS) junctions, or as superconductor-insulator-normal (SIN) junctions. If the devices are used in ways where the Josephson effect is important, they may be called Josephson junctions, although they may physically be SIS junctions.

A.2.1 Tunneling theory†

Tunneling is a phenomenon where a particle crosses a region with a potential barrier that could not be crossed according to classical physics. The usual explanation for this process is that the position of an electron is best described by a probability distribution function that decays beyond the edge of the metal. If two metals are brought close enough that the distribution functions overlap into the other material, then there is a finite possibility that a particle from one metal can be found in the other.

---

† This section follows sections 2.13 to 2.16 of Van Duzer and Turner, [1].

Tunneling between two normal electrodes at absolute zero temperature will be presented here. The density of states is filled up to the Fermi energy and available unfilled states exist immediately above the Fermi energy. If a small voltage is applied across the electrodes, the curves for the two electrodes are shifted so that part of the filled states on one side overlap some of the unfilled states in the other conductor. Thus electrons can tunnel from one side of the barrier while conserving energy. As the voltage is increased, more states become available so the current will increase. If the densities of states are rectangular functions then the tunneling current follows $I_{nn} = G_n V$, or the tunnel junction behaves like a resistor. Note that in this discussion no mention of superconductivity was made: tunneling will occur at any temperature.

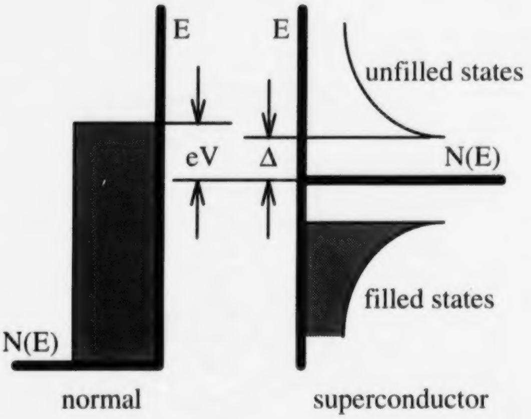

Figure A.7: Density of states representation of normal - superconductor tunneling.

If one of the electrodes is changed to a superconductor, the DC characteristics change. This can be best understood by observing Figure A.7. Here it can be seen that tunneling cannot occur unless there is a potential of $V > \Delta/e$ across the junction, upon which current begins to flow.

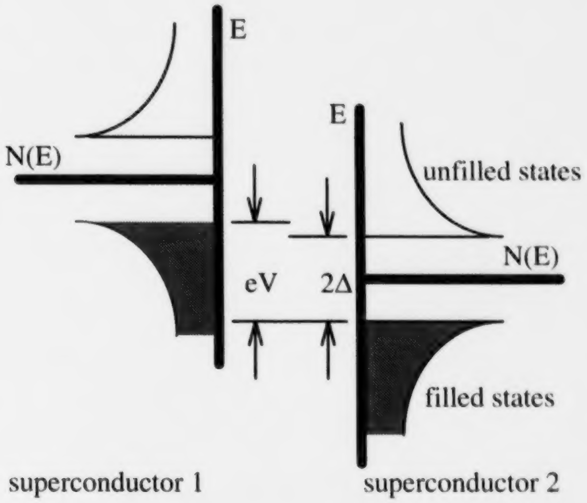

Figure A.8: Density of states representation of SIS quasiparticle tunneling.

Changing the normal electrode to a superconductor changes the junction properties yet again. See Figure A.8. In this case current will not flow until the filled states of one electrode are displaced vertically so that a horizontal movement will put them into the unfilled states of the other electrode. For identical superconductors a potential difference of eV = 2Δ is required.

The density of states representation is quite useful since it not only helps to visualize the process that is occurring, but it can be used to calculate the current as a function of voltage. For the case of T = 0, the quasiparticle tunneling current can be written as

$$\begin{aligned} I_{ss} &= \frac{2\pi eA}{\hbar}\int_{-\infty}^{\infty}|T|^2 N_s(E'-eV)N_s(E')dE' \\ &\cong \frac{G_n}{e}\int_{\Delta}^{eV-\Delta}\frac{|E'-eV|}{\sqrt{(E'-eV)^2-\Delta^2}}\frac{|E'|}{\sqrt{E'^2-\Delta^2}}dE' \end{aligned} \tag{A.4}$$

where *A* is the junction area, *T* is the tunneling matrix coefficient, and G_n is the conductance of an equivalent junction with normal electrodes. The integrand of the first integral can be seen to be the product of the two overlapping density functions along with factors such as the *T* that take into account the physical geometry. The second integral is obtained after substituting a simplified expression for the density of states. At large voltages *V* the Δ term becomes insignificant and the second integral reduces to the form for an NIN junction. Thus the current-voltage characteristic for an SIS junction has no current flowing until $2\Delta/e$ (also called the gap voltage) is reached, and then the current at higher voltages approaches that of a resistor. This is shown in Figure A.9.

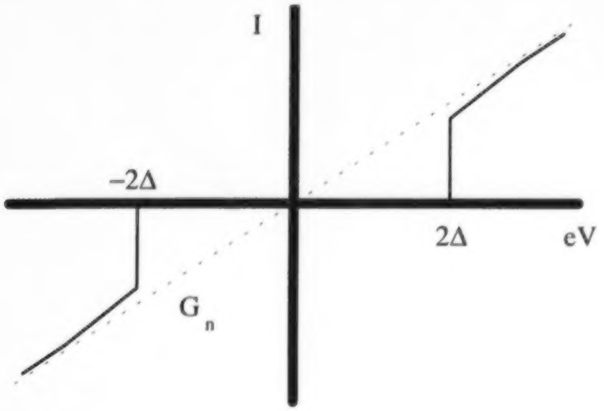

Figure A.9: IV characteristic of a SIS junction.

Real SIS junctions depart from this idealized characteristic. For example, junctions are typically operated at T_c /2 and there will be thermally excited quasiparticles that can tunnel and produce currents at less than the gap voltage. There can be tunneling of Cooper pairs and other types of multiparticle tunneling that also produce sub-gap currents. The current rise in real junctions is also not infinitely sharp since the density of states functions are not actually step-like. One other reason for less than ideal IV characteristics is that a single junction can be thought of as a number of small junctions in parallel. These small junctions may not be identical, so the IV curve is a composite of the smaller junctions.

A.2.2 RF properties of a superconducting tunnel junction[†]

In the previous section it was described how a DC potential can provide the energy to split a Cooper pair and produce a quasiparticle that can tunnel through the insulator. As well the absorption of a photon of sufficient energy can break a pair and thus enable tunneling. This section is concerned with the behavior of SIS junctions with a sinusoidal driving voltage and how to make practical circuits with these devices.

The first problem to attack is how to describe the junction with an AC signal applied. The response of the junction has been derived for a real excitation; now the response to a complex excitation has to be determined. To do this, Cauchy's Integral Formula is used [7]:

$$f(z_0) = \frac{1}{j2\pi} \int_C \frac{f(z)dz}{z - z_0}. \qquad \text{(A.5)}$$

This formula gives values *f* for points z_0 inside the contour *C* along which the values of *f* are known. To be valid, *f* must be an analytic function (that is, the derivative must exist at a point and at all points in the neighbourhood) throughout the complex plane.

[†] Van Duzer and Turner cannot be followed here since that text was written at the time when important theoretical and experimental results for SIS devices were being obtained. The key reference to this section is the review by Tucker and Feldman [6].

Equation (A.5) can be made to apply to the problem of SIS junctions. First consider a half-plane so that the path of integration goes along the real axis from -R to +R, and then along a counterclockwise circular contour back to -R. Cauchy's integral can be broken into two parts,

$$f(z_0) = \frac{1}{j2\pi} \int_{CR} \frac{f(s)\,ds}{s - z_0} + \frac{1}{j2\pi} \int_{-R}^{+R} \frac{f(t)\,dt}{t - z_0} \tag{A.6}$$

a path along the half-circular contour, and another path along the real axis. It can be shown that if $f(z)$ is a bound function, then as $R \to \infty$ the first integral approaches zero. Thus it has been shown that the values in the positive complex plane are completely determined by knowledge of the values along the real axis:

$$f(z_0) = \frac{1}{j2\pi} \int_{-R}^{+R} \frac{f(t)\,dt}{t - z_0}. \tag{A.7}$$

By taking the Cauchy Principal Value (limit as $R \to \infty$) and taking the real part, the Kramers-Kronig Transform (or Hilbert Transform) is obtained.

However, this still isn't adequate to analyze the SIS response since as the voltage across a junction tends to infinity, so does the current. This problem can be worked around by subtracting out the normal state resistance:

$$I(V) - \frac{V}{R_n}. \tag{A.8}$$

This will shift the result of the Kramers-Kronig transform up or down, but in subsequent calculations only the differences between points are used, so this change will be transparent. An earlier assumption about the analytic nature of the function being transformed is also apparently broken by the current step at the gap voltage. But in real junctions the current rise is not infinitely sharp, so the Kramers-Kronig transform can still be used.

One additional crucial piece of information is needed before the response to a sinusoidal voltage can be calculated. The applied voltage modulates the phase of the quasiparticle wave functions according to

$$\exp\left(-j\frac{e}{\hbar}\int_0^t V\cos(\omega t)\,dt\right) = \exp\left(-j\frac{eV}{\hbar\omega}\sin(\omega t)\right). \tag{A.9}$$

The reason why this is so important is that it shows the junction does not react instantaneously to the applied voltage; rather the history of the excitation up to time t will determine the current state of the device. Later it will be shown that the admittance of the junction at some frequencies has a reactive component in addition to the classical geometric capacitance. It is this memory that is the origin of the quantum susceptance.

Now having the reactive current through the junction and the phase factor across the junction, the current with sinusoidal excitation can be calculated. The details of the mathematics involved are given by [6], and only the results will be given here. Since the junction I-V curve is very nonlinear, many harmonics should be generated, increasing the complexity of the problem. However, it is reasonable to assume that signals at twice the local oscillator (LO) frequency and higher will be shorted out by the geometric capacitance of the junction. It is also usually reasonable to assume that the downconverted frequency (the intermediate frequency or IF) is small compared to the LO frequency so that the loads at the LO and signal frequencies will be very similar. Thus a quasi-sinusoidal analysis is valid.

The first result is the total current at the LO frequency through the junction:

$$\begin{aligned}
I_{LO} &= I'_{LO} + jI''_{LO} \\
I'_{LO} &= \sum_{n=-\infty}^{\infty} J_n(\alpha)\left[J_{n-1}(\alpha) + J_{n+1}(\alpha)\right] I_{DC}(V_0 + n\hbar\omega/e) \\
I''_{LO} &= \sum_{n=-\infty}^{\infty} J_n(\alpha)\left[J_{n-1}(\alpha) - J_{n+1}(\alpha)\right] I_{KK}(V_0 + n\hbar\omega/e) \\
\alpha &= V_{LO}/(\hbar\omega/e)
\end{aligned} \qquad \text{(A.10)}$$

where α is the normalized LO amplitude, V_0 is the DC bias voltage, I_{KK} is the Kramers-Kronig Transform of the DC I-V curve, and J_n is the n-th order Bessel function. From this the quantum conductance and susceptance can be written:

$$\begin{aligned}
G_Q &= \frac{1}{V_{LO}} \sum_{n=-\infty}^{\infty} J_n(\alpha)\left[J_{n-1}(\alpha) + J_{n+1}(\alpha)\right] I_{DC}(V_0 + n\hbar\omega/e) \\
B_Q &= \frac{1}{V_{LO}} \sum_{n=-\infty}^{\infty} J_n(\alpha)\left[J_{n-1}(\alpha) - J_{n+1}(\alpha)\right] I_{KK}(V_0 + n\hbar\omega/e)
\end{aligned} \qquad \text{(A.11)}$$

or for small values of α where the Bessel functions can be replaced with zeros and ones:

$$\begin{aligned}
G_Q &\cong \frac{e}{2\hbar\omega}\left[I_{DC}(V_0 + \hbar\omega/e) - I_{DC}(V_0 - \hbar\omega/e)\right] \\
B_Q &\cong \frac{e}{2\hbar\omega}\left[I_{KK}(V_0 + \hbar\omega/e) + I_{KK}(V_0 - \hbar\omega/e) - 2I_{KK}(V_0)\right]
\end{aligned} \quad . \qquad \text{(A.12)}$$

Thus for small signals these parameters can be obtained graphically from plots of the I-V curve and its transform. Note that as the frequency is reduced the quantum susceptance approaches zero, which is the result for classical mixers

Since the SIS junction is being used as a mixer to convert a signal at one frequency to another frequency, Tucker then derives an admittance matrix that relates the voltage at one frequency to the current at another frequency. This analysis confirms that the admittance seen by the LO generator is indeed the quantum admittance. The output impedance at the IF frequency is calculated to be:

$$G_{IF} = \sum_{n=-\infty}^{\infty} J_n^2(\alpha) \frac{d}{dV_0} I_{DC}(V_0 + n\hbar\omega/e) . \qquad \text{(A.13)}$$

$$B_{IF} = 0$$

This is simply proportional to the slope of the pumped I-V curve at the bias point, as can be seen if the DC current is calculated:

$$I_{DC} = \sum_{n=-\infty}^{\infty} J_n^2(\alpha) I_{DC}(V_0 + n\hbar\omega/e). \qquad \text{(A.14)}$$

Again, the IF output impedance is a number that can be obtained by graphical means from a measured I-V curve.

It is now instructive to apply these equations to an I-V curve and to observe the junction parameters. The I-V curve used here is that of an ideal niobium SIS junction with a gap voltage of 2.8 mV, a normal state resistance of 18 Ω, and a local oscillator frequency of 115 GHz. Similar plots were obtained by Worsham *et al.* [8] by direct measurements to confirm this theory. Figure A.10 shows the IV curve and its Kramers-Kronig transform.

If a constant amplitude local oscillator signal is applied to the junction, steps will be induced into the I-V curve with a width of $\omega\hbar/e$. The depth of the steps is determined by the local oscillator amplitude. Figure A.11 shows the curve when the normalized amplitude is $\alpha = 1$. SIS mixers are typically biased in the middle of the first photon step below the gap, so the IF output admittance is the slope at the middle of the step.

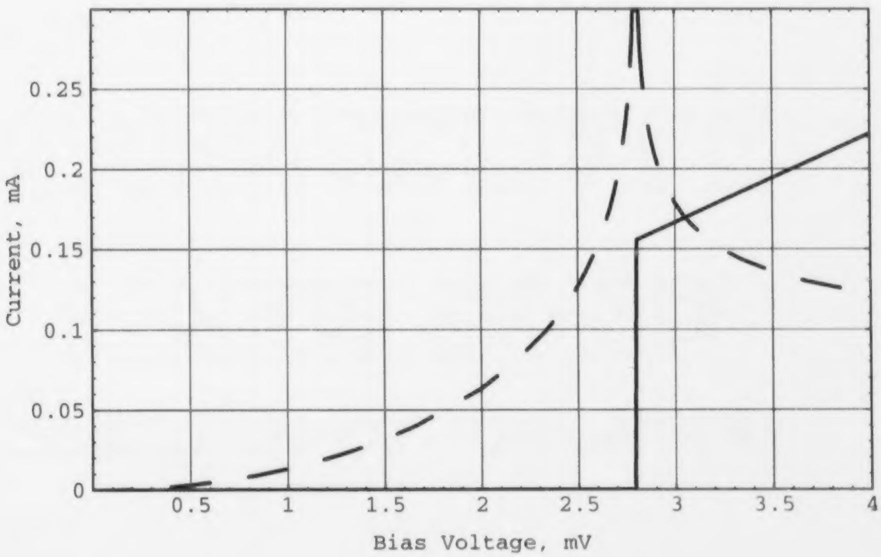

Figure A.10: Junction IV curve (solid line) and its Kramers-Kronig transform (dashed line).

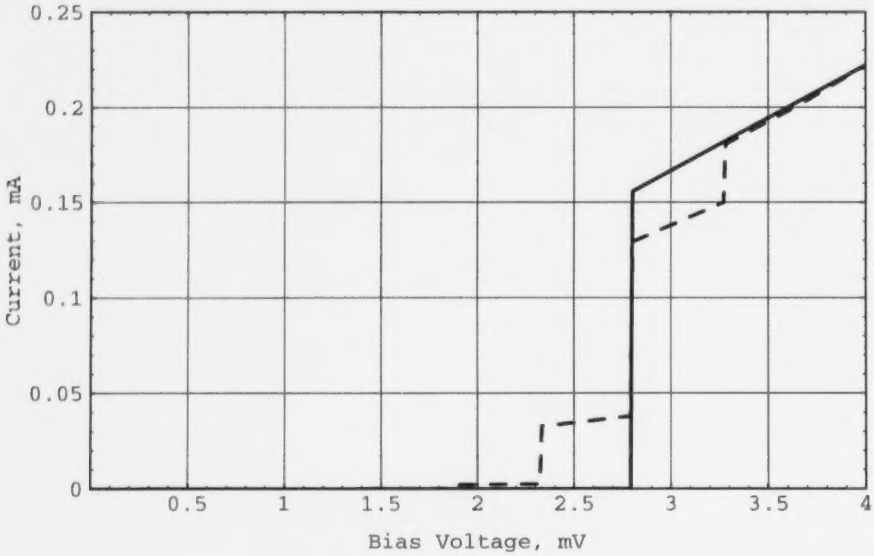

Figure A.11: Junction IV curve without (solid line) and with (dashed line) local oscillator applied.

Knowledge of the junction admittance is important if one is to design low-noise mixers which have efficient coupling between the antenna and the junction. Figures A.12 and A.13 show the real and imaginary parts of the junction admittance as a function of bias. It can be seen that the conductance obtained by measuring the slope between points one photon step below the bias point and one step above is close to the actual value. This value changes a small amount within a photon step of the gap voltage and for most purposes can be considered constant. At voltages well above the gap voltage the conductance approaches the normal state value.

However, the susceptance changes greatly over this bias voltage range. Moving from one photon step below the gap voltage up to the gap voltage, the susceptance starts mildly capacitive, and then becomes inductive with a singularity at the gap voltage. For real junctions which are not infinitely sharp, the value at the gap voltage will be finite. Again it should be emphasized that this reactive component is a result of the quantum basis for the operation of tunnel junctions and is not found in classical mixers or SIS mixers operated at low frequencies. This phenomenon has interesting effects and possible applications.

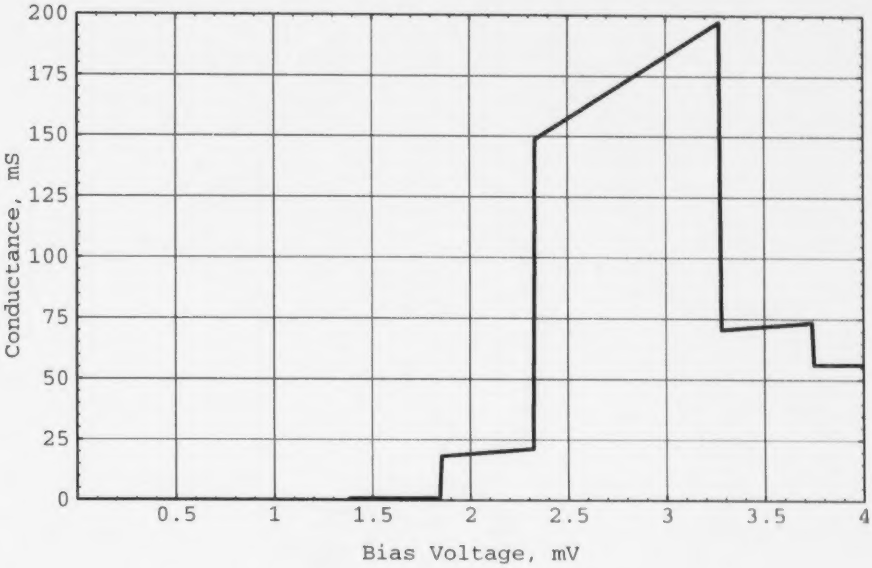

Figure A.12: Quantum conductance of SIS junction.

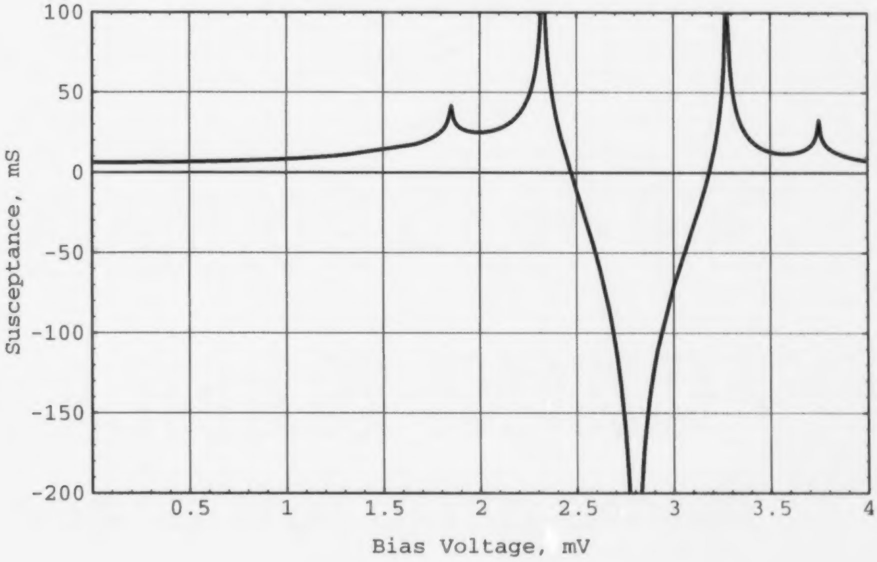

Figure A.13: Quantum susceptance of SIS junction.

Earlier it was stated that these plots were generated for the case of a normalized LO voltage amplitude of one. This is an artificial case since microwave signal generators have a finite output impedance, and there will be a voltage division between the LO and the junction. Since the junction susceptance is not constant with bias voltage, the LO voltage will also not be constant, which in turn changes the susceptance. For this reason actual pumped IV curves will not have straight steps as shown in Figure A.11. In fact they can have *downward* sloping steps which means the IF output impedance is negative. This has been observed [9, 10], but in practice is avoided so that the mixer does not display any instabilities. Some workers have used the distortion of the pumped IV curve to deduce the impedance of the circuit connected to the junction [11].

An interesting application of quantum susceptance is to use it to cancel out the geometric capacitance of a junction. For example, a junction with IV characteristics like those in Figure A.10 would have a susceptance due to the geometric capacitance of ~ 0.13 Siemens at 110 GHz. This can clearly be resonated out by the quantum susceptance.

The material presented here is sufficient to design SIS mixers. Further material provided by Tucker will permit a detailed analysis of the performance of the mixer including noise and conversion gain. Wengler [12] provides a summary of current design practice and of recent results.

A.3.0 Electromagnetic properties of superconductors

In this section a set of equations will be derived that describes the electromagnetic behavior of superconductors. Unlike a previous section where an accurate physical description of the mechanism of superconductivity was shown, the theory to be developed here simply modifies Maxwell's equations so that they fit two observed phenomena. When this theory was first developed, it was realized that electrons were somehow involved in conduction in superconductors, but it was not known that pairs of electrons were involved or that an energy gap existed for normal excitations. Thus these results will lack precision, but the derivation will be less obscure than it would otherwise be and the equations will be sufficient for most engineering applications.

A.3.1 London equations[†]

The most widely known property of superconductors is the flow of DC current without resistance. Since resistance is a result of the scattering of charge carriers by lattice imperfections and impurities in a metal, it can be assumed that no such scattering (and limiting velocity) occurs in a superconductor. Thus if an electric field is applied, an electron will be accelerated at the rate:

$$\dot{\mathbf{v}} = \frac{e}{m}\mathbf{E} \tag{A.15}$$

where m and e are the mass and charge of the superelectrons. If n_S is the superelectron density, the current density is

$$\mathbf{J} = en_S\mathbf{v} \tag{A.16}$$

[†] This section and the next follow chapters 2 & 3 of Rose-Innes and Rhoderick, [13].

and by taking the time derivative and substituting in Equation (A.15) the change in current density can be found:

$$\dot{\mathbf{J}} = \frac{e^2 n_S}{m} \mathbf{E}. \tag{A.17}$$

For the next step begin with the point forms of Faraday's and Ampère's Laws:

$$\begin{aligned} \dot{\mathbf{B}} &= -\nabla \times \mathbf{E} \\ \nabla \times \mathbf{H} &= \mathbf{J} + \dot{\mathbf{D}} \end{aligned} . \tag{A.18}$$

Ampère's Law can be simplified to

$$\nabla \times \mathbf{B} = \mu_0 \mathbf{J} \tag{A.19}$$

because the fields do not vary rapidly with time, making the derivative of **D** small compared with **J**. Using the earlier result for superconductors, Faraday's Law can be written as

$$\dot{\mathbf{B}} = -\frac{m}{e^2 n_S} \nabla \times \dot{\mathbf{J}}. \tag{A.20}$$

This can be combined with Ampère's Law to give

$$\begin{aligned} \dot{\mathbf{B}} &= -\alpha \nabla \times \nabla \times \dot{\mathbf{B}} \\ \alpha &= m/(\mu_0 e^2 n_S) \end{aligned} . \tag{A.21}$$

Using Gauss' Law for magnetic fields ($\nabla \cdot \mathbf{B} = 0$) the double curl can be reduced to grad squared. To further simplify things assume that the flux is perpendicular to the x-axis. The differential equation then becomes

$$\frac{\partial^2 \dot{B}}{\partial x^2} = \frac{1}{\alpha} \dot{B}. \tag{A.22}$$

The bounded solution to this common differential equation can be written by inspection:

$$\dot{B}(x) = \dot{B} \exp\left(-x/\sqrt{\alpha}\right). \tag{A.23}$$

Equation (A.23) predicts that the time rate of change in the magnetic flux approaches zero inside a perfect conductor. Thus if a superconductor were a perfect conductor, cooling it through the transition temperature in the presence of a magnetic field would trap the flux lines through the material since the equation states that they cannot change with time. In 1933 Meissner and Ochsenfeld showed that this is not the behavior of superconductors. They found that regardless of the state of the external magnetic field above the superconducting transition temperature, when the material became superconducting all fields were excluded from the interior. Therefore a superconductor is a perfect diamagnetic material since **B** = 0 in the material.

A.3.2 Magnetic penetration depth

With this second observation, the above derivation is restricted even further. Not only must the time derivative of the field decay with distance into the superconductor, but the field itself must also decay. Thus **B** must obey

$$\nabla^2 \mathbf{B} = \frac{\mathbf{B}}{\alpha} \tag{A.24}$$

which gives an exponential decay of the field as

$$B(x) = B_a \exp\left(-x/\lambda_L\right) \tag{A.25}$$

with the penetration depth defined as

$$\lambda_L = \sqrt{\alpha} = \sqrt{m/(\mu_0 e^2 n_S)}\,. \tag{A.26}$$

A typical value is several tens of nanometres.

Working backwards from these results, a second London equation can be derived that relates the magnetic field to the currents in the superconductor:

$$\mathbf{B} = -\mu_0 \lambda_L^2 \nabla \times \mathbf{J}\,. \tag{A.27}$$

Thus the current density as a function of depth is

$$J_y(x) = \frac{B_a}{\mu_0 \lambda_L} \exp\left(-x/\lambda_L\right) = J_a \exp\left(-x/\lambda_L\right). \tag{A.28}$$

This shows that the current in the superconductor flows within a penetration depth of the surface. The magnetic field also penetrates to this depth. Within this thin shell, screening currents are set up that produce magnetic fields deeper inside the superconductor to cancel the external field.

An empirical expression has been obtained for the penetration depth as a function of temperature, which is

$$\lambda_L(T) = \frac{\lambda_L(0)}{1-\left(T/T_C\right)^4}\,. \tag{A.29}$$

This shows that as the temperature is raised towards T_C, the penetration depth approaches infinity or the current and field fill the entire metal and it becomes a normal conductor. Also note that at half the critical temperature, the penetration depth is only 7% larger than the value for absolute zero.

A.3.3 Superconducting transmission lines

It is now interesting to look at the properties of transmission lines constructed with superconducting metal. Although superconductivity does not alter the capacitance of a transmission line, with certain line geometry the inductance can be modified due to kinetic energy storage by the Cooper pairs. It is possible to use thin-film deposition techniques to make very thin conducting and insulating layers that will enhance this effect.

The starting point for this derivation is to consider an infinite parallel-plate waveguide which has all of the magnetic field confined between the plates. It can be shown that the solution for the field as a function of depth y into the metal is

$$B_x(y) = \mu_0 J \frac{\sinh(y/\lambda_L)}{\sinh(b/\lambda_L)} \tag{A.30}$$

where J is the current density and b is the metal thickness.

A more practical type of transmission line consists of a large (effectively infinite) ground plane covered with an insulating layer of thickness d and a narrower conductor of width w on top. A cross section through this line is shown in Figure A.14. The superconducting film thicknesses are denoted by b, the magnetic penetration depths by λ, and the volume of integration is shown with the dotted line. The inductance will be found by equating the energy stored in the inductance to the total energy stored in the line, as shown by:

$$W = \frac{Li^2}{2} = \frac{1}{2}\int_V \mathbf{B}\cdot\mathbf{H}\,dV + \frac{1}{2}\int_V mv^2 dV \tag{A.31}$$

where i is current, V is volume, and m, e, and v are electron mass, charge, and velocity.

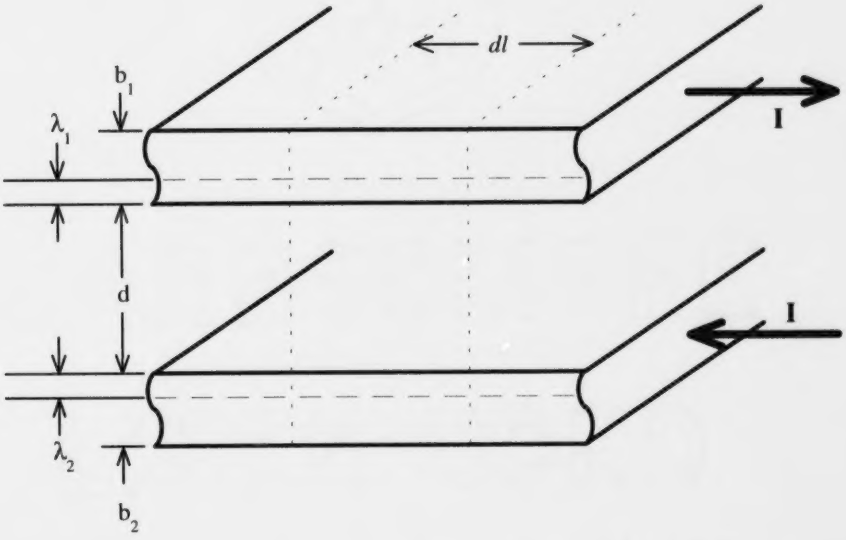

Figure A.14 Geometry of microstrip transmission line showing the volume of integration.

A number of substitutions can be made to simplify the analysis:

$$\begin{aligned}&\mathbf{H}=\frac{\mathbf{B}}{\mu_0},\\&m=n_S m_S,\\&v=J_S/(en_S),\\&\lambda_L=\sqrt{m_S/\mu_0 n_S e^2}\end{aligned}\qquad\text{(A.32)}$$

where n_S and m_S equal the density and mass of the Cooper pairs. Thus Equation (A.31) becomes:

$$Li^2=\frac{1}{\mu_0}\int_V\left(B^2+\mu_0{}^2\lambda_L{}^2J_S{}^2\right)dV.\qquad\text{(A.33)}$$

The first part of the integral is a result of the energy stored in the magnetic field, and the second part is due to the kinetic energy of the Cooper pairs. The integration is performed by breaking the volume into parts: within the metal the earlier equation for B is used, and J is obtained by applying Ampère's Law ($\nabla\times\mathbf{B}=\mu_0\mathbf{J}$). In the dielectric the current density is obviously equal to zero and the magnetic flux density is a constant value and continuous with the flux density at the surface of the superconductor. After evaluating this integral and simplifying the result, the equation for the inductance of a microstrip line of width w is obtained:

$$L=\frac{\mu_0 d}{w}\left(1+\frac{\lambda_1}{d}\coth\left(\frac{b_1}{\lambda_1}\right)+\frac{\lambda_2}{d}\coth\left(\frac{b_2}{\lambda_2}\right)\right).\qquad\text{(A.34)}$$

It is instructive to look at several limiting cases. If the film thicknesses are large relative to the magnetic penetration depth, then the hyperbolic cotangent functions approach unity and Equation (A.34) becomes

$$L\cong\frac{\mu_0}{w}\left(d+\lambda_1+\lambda_2\right),\qquad\text{(A.35)}$$

and if the dielectric thickness is also large compared with the penetration depth, the usual equation for a normal conductor microstrip line is obtained ($L=\mu_0 d/w$). Thus the case when d is not large can be understood by increasing the dielectric thickness by the two penetration depths. This change in inductance is strictly a result of the geometry of the films and the penetration depth.

Now consider the other extreme, where the film thickness is less than the penetration depth. By using a series expansion of the hyperbolic cotangent function, the inductance equation can be approximated by:

$$L \equiv \frac{\mu_0}{w}\left(d + \frac{b_1}{3} + \frac{b_2}{3} + \frac{\lambda_1^{\,2}}{b_1} + \frac{\lambda_2^{\,2}}{b_2}\right). \tag{A.36}$$

The first three terms in the sum clearly form the normal result modified by field penetration into the metal. The last two terms must be the kinetic components since they increase as the films are made thinner. If these terms were due to geometry only, the inductance would be expected to decrease with thinner films. This assertion that the last two terms are kinetic inductance terms is made stronger by replacing the penetration depth with the value derived from fundamental parameters:

$$L_K = \frac{1}{wb}\frac{m_S}{n_S e^2}. \tag{A.37}$$

The kinetic inductance can be obtained directly by taking the first London equation,

$$\dot{\mathbf{J}} = \frac{e^2 n_S}{m}\mathbf{E}, \tag{A.38}$$

and solving for a sinusoidal current. Using the usual definitions for current density and electric field, this simplifies to

$$V = j\omega\frac{m}{e^2 n_S wb} I \tag{A.39}$$

and comparing with $V = j\omega LI$, it is seen that these two expressions for inductance are the same.

The relation between the inductance and the number of superconducting electrons may seem strange since as the number of superconducting carriers increases, the kinetic inductance (which is a result of the existence of superconducting electrons) decreases. This apparent paradox can be resolved by way of a simple analogy. Consider two water pipes with different cross-sectional area that deliver the same flow (volume per unit time). The density of water (volume per unit length) is lower in the smaller pipe, so the velocity of that water must be greater to deliver the same volume. Thus the water in the narrower pipe will possess greater kinetic energy.

And finally, a reminder of how the kinetic inductance modifies observed transmission line parameters. Since the velocity of propagation is $1/\sqrt{LC}$, wave propagation down the line is slowed. The characteristic impedance of the line is $\sqrt{L/C}$, so the impedance is increased. Thus it can be seen that a transmission line constructed with the kinetic inductance enhanced could be very useful. For example it may have a higher impedance than what could be constructed with normal metals, or the physical length could be reduced while maintaining the same phase length. Also, if the population of superconducting electrons could be controlled, the transmission line would be adjustable. Several ways to do this are by heating the line, injecting quasiparticles with a current through a tunnel junction, or by illuminating the metal with photons of energy great enough to split pairs.

A.3.4 Two-fluid model

Until now, only the superconducting electrons in the metal have been considered. However, between absolute zero and the transition temperature normal electrons will be present, and will influence the electrical properties for an AC signal. The two fluid model is based on a superconductor with populations of both types of carriers and densities described by this empirical equation:

$$\frac{n_S}{n} = 1 - \left(\frac{T}{T_C}\right)^4. \qquad \text{(A.40)}$$

Thus the total current can be written as the sum of the normal and super currents:

$$\mathbf{J} = \mathbf{J}_s + \mathbf{J}_n = (\sigma_1 - j\sigma_2)\mathbf{E}. \qquad \text{(A.41)}$$

Up to frequencies where the period of the electric field is comparable to the momentum relaxation time (several hundred GHz), the conductivity can be approximated as

$$\begin{aligned} \sigma_1 &= \sigma_n (n_n/n), \\ \sigma_2 &= 1/(\omega\mu_0\lambda_L{}^2) \end{aligned} \qquad \text{(A.42)}$$

where σ_n is the normal state conductivity just above T_c. Figure A.15 shows a simple circuit model to explain the two fluid model.

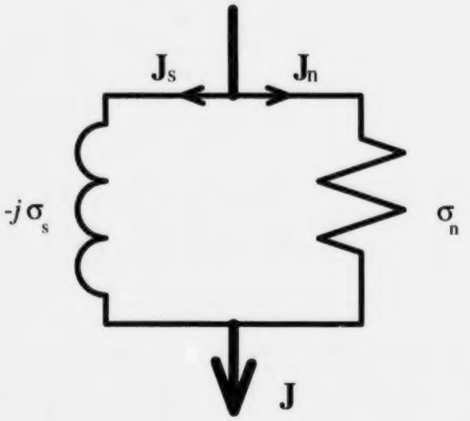

Figure A.15 Schematic representation of two fluid model of current through a superconductor.

The surface impedance for a superconductor can be obtained by substituting the two conductivities into the classical equation for surface impedance:

$$Z_s = \sqrt{j\omega\mu_0/\sigma} \qquad \text{(A.43)}$$

and after several approximations obtain

$$Z_s \cong \omega^2\mu_0{}^2\lambda_L{}^2 n_n\sigma_n/(2n) + j\omega\mu_0\lambda_L. \tag{A.44}$$

This result is important from a design point of view since it provides an alternate way of calculating the properties of a transmission line. For example, it is often more convenient to use an electromagnetic simulation program to obtain the properties of microstrip transmission lines. Rather than simulating the geometric inductance, and then adding the kinetic inductance, a program can use the surface impedance as a boundary condition and obtain the correct transmission line properties directly.

A.4.0 Superconducting quantum interference devices (SQUIDs)†

So far only quasiparticle tunneling in SIS devices has been discussed. However, Cooper pairs are also capable of tunneling if the wave functions on either side of the barrier overlap. Since Cooper pairs are boson-like, there is no restriction on the number that can tunnel into a particular energy level, so tunneling can occur with a zero potential between the electrodes. If a potential is applied, this excess energy is dissipated by the emission of a photon. Thus we can see that a tunnel junction can be used as a radio frequency signal generator. And since the junction has a coherent superconducting wave function tunneling through, the boundary conditions on superconducting loops can be used to realize circuits capable of measuring magnetic fields and thus inductances. The next sections will outline how measuring circuits that exploit pair tunneling can be formed.

A.4.1 The Josephson junction as an RF signal source

Consider two superconductors far apart. The wave function in each can be described by the phasor

$$\Psi = \Psi_0 e^{j(\mathbf{P}\cdot\mathbf{r})/\hbar} \tag{A.45}$$

where **P** (the momentum of a pair) and **r** (the position) determine the phase and $|\Psi|^2$ is the density of pairs. If the two superconductors are brought very close together the wave functions, which extend ~100 nm beyond the surface of the metal, begin to overlap the other metal. Thus it is now possible for the Cooper pairs to tunnel across the gap. Since Cooper pairs are boson-like, they all occupy the same ground state and there is no restriction on the number in this state. Therefore it is possible for a Cooper pair to tunnel with no potential across the junction. This is clearly unlike quasiparticle tunneling which had an energy gap and a limited number of states to tunnel into.

It is also important to note that as the superconductors are brought together and tunneling becomes possible, the phases of the wave functions become coupled. Feynman *et al.* [14] derive the Josephson equations:

$$\begin{gathered} J = J_c \sin\phi \\ f = \frac{1}{2\pi}\frac{\partial\phi}{\partial t} = \frac{qV}{h} \cong \frac{482\text{GHz}}{\text{meV}}V \end{gathered} \tag{A.46}$$

---

† This section is based largely on Feynman, Leighton and Sands,[14] pp. 21-1 to 21-18

with J_c the critical current density of the junction, ϕ is the wave function phase across the junction. If the junction is biased to a voltage V the current will oscillate at a frequency f.

Using a tunnel junction as a voltage-controlled oscillator has several possible applications. One is to provide the local oscillator signal in an integrated circuit millimetre-wave receiver. Another is to form a circuit to measure the properties of thin-film materials at cryogenic temperatures. In this configuration the junction is coupled to an unterminated transmission line that contains the materials under test. The bias is swept which in turn sweeps the oscillator frequency. As the frequency passes through transmission line resonances, the DC bias current is perturbed. Thus the resonance frequencies can be determined, and from this information the material properties can be extracted.

A.4.2 Inductance measurement using SQUIDs

Superconducting Quantum Interference Devices (SQUIDs) are constructed with one or more junctions connected to a superconducting loop and to a bias supply. These devices are famous for being able to measure very minute magnetic fields. Here we will discuss the DC-biased SQUID used for measurement of superconducting transmission lines.

The physical basis of the operation of a SQUID is simple once one accepts the long-range coherence of the Cooper pair wave function. By "long-range coherence" it is meant that once the phase, amplitude, and wavelength of the wave function are known at one point, the phase and amplitude can be calculated for any other point in the (continuous) super conductor. This is analogous to electromagnetic wave propagation in a transmission line. This coherence is maintained throughout the superconductor: for example, if a large superconducting magnet is made of a kilometre of wire, then the wave function extends the full kilometre.

Now consider a property of superconducting loops. Starting at one point, and going around the loop back to that point, the phase change experienced must be an integral number of revolutions on the complex plane, that is

$$\begin{aligned} &\Delta\phi = 2n\pi \\ &n = 0,1,2,\ldots \end{aligned} \tag{A.47}$$

This is a necessary condition so that the wave function has only one value at any point. Note that the wavelength of the wave function is a function of the momentum of the electron pair, as can be seen by $\lambda = h / P$. Thus the phase around the loop is

$$\Delta\phi = 2\pi\oint\frac{\hat{\mathbf{x}}\cdot d\mathbf{l}}{\lambda} = \frac{1}{\hbar}\oint\mathbf{P}\cdot d\mathbf{l} \tag{A.48}$$

where $\hat{\mathbf{x}}$ is a unit vector in the direction of propagation. It can be shown that the momentum of a pair of electrons in a magnetic field actually has two components, the well known velocity dependent term, and a term that is the product of the charge and the magnetic vector potential. The momentum thus takes the form:

$$\mathbf{P} = 2m\mathbf{v} + 2e\mathbf{A}. \tag{A.49}$$

For the moment the kinetic component will be ignored. Combining Equations (A.48) and (A.49) and using Stokes' Theorem produces a simple relation

$$\frac{2e}{\hbar}\oint \mathbf{A}\cdot d\mathbf{l} = \frac{2e}{\hbar}\iint_S (\nabla\times\mathbf{A})\cdot d\mathbf{s} = \frac{2e}{\hbar}\iint_S \mathbf{B}\cdot d\mathbf{s} = \frac{2e}{\hbar}\Phi = 2n\pi \quad \text{(A.50)}$$

where Φ is the flux.

In a SQUID circuit, such as that in Figure A.16, there will be "phase drops" across the tunnel junctions in addition to the phase along the superconductor. Again using a common electrical analogy, this is like Kirchhoff's Voltage Law where the sum of the voltages around a loop equals zero.

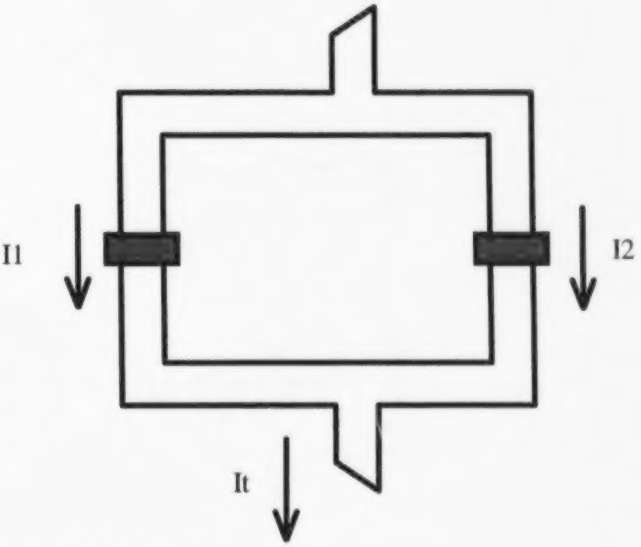

Figure A.16: Schematic of SQUID. Shaded boxes represent tunnel junctions and the clear shapes are the superconducting wiring.

An equation for the wave function phase can be written by going around this loop in a clockwise direction and adding the phase across the right side junction (ϕ_r), subtracting the phase of the left side junction (ϕ_l), and equating the sum to zero. This produces the loop equation

$$\phi_r - \phi_l + \frac{2e}{\hbar}\Phi = \phi_r - \phi_l + \frac{2\pi\Phi}{\Phi_0} = 0 \quad \text{(A.51)}$$

with Φ_0 equal to the magnetic flux quantum. Now that the relationship between the phases across the junctions is known, an equation for the total current can be written:

$$I_t = I_r + I_l = I_C\left(\sin(\phi_r) + \sin(\phi_l)\right) = I_C\left(\sin(\phi_r) + \sin\left(\phi_r - \frac{2\pi\Phi}{\Phi_0}\right)\right) \tag{A.52}$$

This can be simplified with trigonometric rules. It is found that the $\sin(\phi_r)$ term is modulated by a rectified cosine function:

$$\left|I_t(\Phi)\right| = 2I_C\left|\cos\left(\frac{\pi\Phi}{\Phi_0}\right)\right|. \tag{A.53}$$

Thus by counting fringes the magnetic field strength can be determined.

Note that what the SQUID is really measuring is the momentum of the superconducting electrons. In the example above the effect of the external field was assumed to dominate both the internal field and the kinetic components of the momentum. However by minimizing the loop cross-sectional area, the SQUID can be made insensitive to external fields, so that it can be used to measure the internally generated fields or inductance of conductors. This is a complete measurement of the inductance (including the kinetic inductance) since the Cooper pair momentum is the actual quantity that is measured. It is also interesting to note that this inductance measurement is taking place at DC; classical inductance measurements usually require the test element to be excited by an AC source.

A.5 Conclusions

In this appendix a summary of the theory of superconductivity has been presented from an engineering point of view. Emphasis has been given to aspects important to the design and construction of millimetre-wave receivers. The theory of superconducting tunnel diodes has been discussed and simple relationships for obtaining the circuit parameters of these devices have been shown. The problem of superconducting transmission lines has been addressed and equations for dealing with this problem have been developed. And finally several circuits that are useful for measuring transmission line properties have been described.

A.6 References

[1] T. Van Duzer, C. W. Turner, *Principles of Superconductive Devices and Circuits*, New York:Elsevier, 1981

[2] J. S. Blakemore, *Solid State Physics*, Cambridge:Cambridge University Press, 1985

[3] J. Bardeen, L. N. Cooper, J. R. Schrieffer, "Theory of superconductivity," *Phys. Rev.*, vol. 108, pp. 1175-1204, 1957

[4] L. N. Cooper, "Theory of superconductivity," *Am. J. Phys.*, pp. 91-101, 1960

[5] S. B. Kaplan, C. C. Chi, D. N. Langenberg, J. J. Chang, S. Jafarey, D. J. Scalapino, "Quasiparticle and phonon lifetimes in superconductors," *Phys. Rev. B*, vol. 14, pp. 4854-4873, 1976

[6] J. R. Tucker, M. J. Feldman, "Quantum detection at millimeter wavelengths," *Rev. Mod. Phys.*, vol. 57, pp. 1055-1113, 1985

[7] R. V. Churchill, J. W. Brown, R. F. Verhey, *Complex Variables and Applications*, New York:McGraw-Hill, 1976

[8] A. H. Worsham, N. G. Ugras, D. Winkler, D. E. Prober, N. R. Erickson, P. F. Goldsmith, "Quantum tunneling currents in a superconducting junction," *Phys. Rev. Lett.*, vol. 67, pp. 3034-3037, 1991

[9] A. R. Kerr, S.-K. Pan, M. J. Feldman, A. Davidson, "Infinite available gain in a 115 GHz SIS mixer," *Physica*, vol. 108B, pp. 1369-1370, 1981

[10] A. D. Smith, W. R. McGrath, P. L. Richards, H. van Kempen, "Negative resistance and conversion gain in SIS mixers," *Physica*, vol. 108B, pp. 1367-1368, 1981

[11] C. A. Mears, Qing Hu, P. L. Richards, "Numerical simulation of experimental data from planar SIS mixers with integrated tuning elements," *IEEE Trans. Mag.*, vol. MAG-25, pp. 1050-1053, 1989

[12] M. J. Wengler, "Submillimeter-wave detection with superconducting tunnel diodes," *Proc. IEEE*, vol. 80, pp. 1810-1826, 1992

[13] A. C. Rose-Innes, E. H. Rhoderick, *Introduction to Superconductivity*, Oxford: Pergamon, 1978

[14] R. P. Feynman, R. B. Leighton, M. Sands, *The Feynman Lectures on Physics*, Vol. 3, Reading, MA: Addison-Wesley, pp. 21-1 to 21-18, 1965